TOPICS IN STRESS-INDUCED INSTABILITIES AND PHASE TRANSITIONS IN LATTICE-BASED SOLIDS

A Thesis
Presented to
The Academic Faculty

By

Hossein Salahshoor Pirsoltan

In Partial Fulfillment
of the Requirements for the Degree
Doctor of Philosophy in the
School of Aerospace Engineering

Georgia Institute of Technology

December 2018

TOPICS IN STRESS-INDUCED INSTABILITIES AND PHASE TRANSITIONS IN LATTICE-BASED SOLIDS

Approved by:

Dr. Julián J. Rimoli, Advisor
School of Aerospace Engineering
Georgia Institute of Technology

Dr. Massimo Ruzzene
School of Aerospace Engineering
Georgia Institute of Technology

Dr. George Kardomateas
School of Aerospace Engineering
Georgia Institute of Technology

Dr. Arash Yavari
School of Civil and Environmental Engineering
Georgia Institute of Technology

Dr. Dennis M. Kochmann
School of Mechanical and Process Engineering
ETH Zürich

Date Approved: October 30, 2018

To my lovely parents and siblings

ACKNOWLEDGEMENTS

I would like to express my sincere gratitude to my advisor, Professor Julián J. Rimoli, without whom this thesis would not have been possible and for his unwavering support during the journey of PhD. Similarly, I also would like to thank my undergraduate advisor, Professor Soheil Mohammadi, whom introduced me to the fascinating world of mechanics.

I am also very grateful to Professors George Kardomateas, Dennis M. Kochmann, Massimo Ruzzene and Arash Yavari for their guidance and participation in my thesis committee.

I would like to express my deepest gratitude to Professor Rafael de la Llave for his mentorship, whom left a profound impact in my life.

I am also thankful to Raj Kumar Pal for his invaluable contribution and guidance. I wish to thank my fellow group members Claudio, Hernan, Aarohi, Aaron, Ali, Juan, Julie, Daniel, German, Kip, Eric and my very good friend Jean-Baptiste. Many thanks should also go to my colleagues Anirudh, Farshad, Ali, Javi, William, Yuan, Lei, Jiaqi, Yian, Mohit, Donald -whom kindly proofread my thesis-, Arman, Ruthvik and Professor Mike Mello.

My life in the past five years was inspired by many great friends in Georgia Tech. Just to mention a few names, mbare Giuseppe, Kamal, Matteo and his kind wife Francesca, Mikel, Paolo and Pouya and his wonderful wife Neda. A special recognition goes to my dearest buddy Hanif. I also made a lot of friends outside school. Their names are far too many to write here. You know who you are: Thank you!

Finally, I would like to express my deepest gratitude to my adorable parents and siblings, for their continuous support and love, to whom this thesis is dedicated to, particularly my brother Meisam.

TABLE OF CONTENTS

LIST OF FIGURES

SUMMARY

Mechanical response of a lattice-based solid, where the entire system is built up by a repetitive translation of a unit cell along its principal axes, manifests itself in changes either in the macro or the microstructure of the system. Depending on the loading configuration, drastic and remarkable changes may occur in the mechanical behavior of the entire lattice, often triggered by a macro or micro instability. The outcome of these instabilities varies significantly across different systems and scales, and is often reflected in phenomena such as, but not limited to, defect nucleation, shear bands, phase transitions and pattern formations. The subject of this thesis is to study stress-induced instabilities in certain groups of lattice-based solids, as well as their manifestations on mechanical properties of the whole lattice. Although we choose certain families of materials and metamaterials in our study, the approaches that we employ could be utilized to investigate instabilities of any system with translational symmetry.

In chapter two, we investigate stress-induced instabilities in single crystal metals. We study the onset of symmetry breaking in four distinct metals of both FCC and BCC structure. We subject them to a combined shear and dilation, and examine the Schmid assumption, whereby we identify the onset of plasticity with the onset of instability. We perform both phonon and elastic stability analysis. We study the nature of the instability and show for the first time, to the best of our knowledge, that the short wavelength instabilities are abundant. Our results illustrate the potential pitfalls of relying on the widely used elastic stability analysis and disqualifies it as the method of choice.

In chapter three, we investigate stress-induced material symmetry phase transitions in tensegrity-based metamaterials. We study material symmetries of tensegrity lattice by examining the eigenspaces of the effective elasticity tensor, obtained through a homogenization scheme. We demonstrate symmetry breaking and phase transitions, occurring solely due to pre-stressing the members of the lattice. We observe several phase transitions includ-

ing cubic to tetragonal and tetragonal to orthotropic and vice-versa. We also demonstrate existence of a discrepancy between the material symmetries of a finite and infinite lattice, and show that imposing periodic boundary conditions can lead to physically incorrect results. Our results suggest new research paths for designing tensegrity-based metamaterials and tuning their properties through adjusting the pre-stretches in the cables.

In chapter four, we study the mechanical response of homogeneous two dimensional tensegrity lattices. We aim to investigate the effect of lattice connectivity on the corresponding mechanical properties. We propose new designs of two dimensional lattices with very similar geometry, which only differ in the connectivity of compression members. We verify the stability of the proposed lattice, and then compare the mechanical response of two lattices, subjected to uniaxial compression, with connected and isolated compression members. We demonstrate that while local instabilities lead to global instability in the former case, the latter case remains globally stable for a vast regime of deformations. We believe our results create new avenues for investigating the complex problem of emergence of localized deformations.

CHAPTER 1
INTRODUCTION

1.1 Background and motivation

Mechanical response of an unstressed solid subjected to an external excitation is often manifested in global and local phase transitions among admissible states of the system. These phase transitions have a significant impact on the mechanical properties of the system, which makes them a key element for both understanding the material behavior as well as proposing predictive material models; they are often the trigger for material or structural failure. From a mathematical perspective, changes in certain parameters of the governing equations -which could be an external force or displacement in our context-, can lead to an instability, triggering a phase transition, in the system, which roots from a loss of uniqueness in the solution of the governing equations. The aim of this thesis is to shed light on the current understanding of instabilities and material symmetry phase transitions, as one example of possible phase transitions in lattice-based systems, from crystalline materials to the more recently proposed 'metamaterials'.

One popular approach for studying discrete lattice-based systems, is the homogenization approach [1], where the discrete system is substituted by an 'equivalent' continuum one; and the continuum mimics, as close as possible, the desired properties of the discrete system. This, in turn, can be very challenging, thus compromising the accuracy of the results. Yet, homogenization has proven to be very useful and accurate for studying vast regimes of deformation; particularly, since it allows us to incorporate the translational symmetry of the system and reduce the dimension of our problem. Thus we will employ a homogenization scheme in studying instabilities and material symmetries of lattices -where a homogenization scheme is well justified-, as well as investigating possible inaccuracies

manufactured by replacing a discrete system with a continuum one.

Instabilities in materials and structures, are ubiquitous, with some important examples including: buckling of structures, defect nucleation, phase transformations, plastic necking, strain or stress localization and fracture [2]. From a variational perspective, once certain variational inequalities -which are measures of convexity of the energy functional- are not satisfied, instabilities will occur in both material level (microscopic instabilities) and structural level (macroscopic instabilities). A more well known scenario is loss of ellipticity -for continuous systems- or loss of positive-definiteness -for discrete systems- in the constitutive relations. Instabilities in crystalline materials have been studied by several other researchers [3, 4, 5, 6, 7, 8, 9]. The abundance of defects (e.g., dislocations) in bulk crystalline materials has resulted in research focusing primarily on defect evolution or nucleation from existing ones (e.g., Frank-Read source) as opposed to defect nucleation in a perfect lattice. However, with recent advances in nanoscale devices, investigating defect nucleation in perfect lattices is gaining attention [10, 4, 3]. Instabilities in periodic metamaterials have also been the subject of study in the recent years[11, 2]. Instabilities in metamaterials could be beneficial, if mobilized in a controlled fashion, such as soft materials [12, 13], large deformation of 2D lattices and cellular solids [14, 15, 16] and acoustic wave guides [17, 18, 19].

Another key aspect of lattices that will be the focus of this thesis is the material symmetry phase transitions in lattices. Even though we will focus on a specific class of metamaterials, the approaches and techniques are general and applicable to any periodic media. In the context of this thesis, we define metamaterials as structural arrangements built at a scale much smaller than that of the application they are intended to, thus exhibiting an effective behavior different than its constituent materials at that large scale [20, 21, 22, 23]. That effective behavior is usually not easily achieved through traditional materials, e.g, metamaterials have been utilized to steer stress waves, generate phononic band-gaps, and to achieve negative effective refraction indices [24, 25, 20, 26, 27, 28]. Among several

classes of metamaterials, tensegrity-based metamaterials have recently gained significant attention [29, 30, 31]. Tensegrity-based metamaterials are a class of lattices composed of two types of members, cables and bars. The name is inspired from the work of Fuller [32], who introduced it and labeled it as tensile-integrity structures. The key feature of tensegrity lattices is the disconnectedness of their compression members (bars), while the tensile members (cables) are connected [33]. They have a wide range of applications in space structures [34, 35], civil engineering [36], and have recently been used to model biological structures [37, 38, 39]. Also, the isolation of compression members suits particularly well for impact absorption applications [29, 40].

As hinted earlier, mechanical instabilities can cause severe structural changes either in the global or local level. In the latter case, localized deformations, a particular zone deteriorates much faster than the rest of the material, thus leading to structural failure. Why certain instabilities lead to localized deformations in a homogeneous system, and what are the primary factors leading to either of the deformations type -local and global- are still open questions for the most part. We aim to investigate the effect of geometry, particularly the lattice connectivity, on the formation of localized solutions, as the final chapter of the current thesis.

1.2 Objectives

In the case of materials, we focus on single crystal metals. We investigate two important aspects of the nature of defect nucleation in metallic crystals: I) Schmid Law; II) the type of instabilities.

We investigate the validity of Schmid law by looking at the onset of plasticity, i.e. defect nucleation in perfect single crystal metals. Schmid law in crystal plasticity was proposed by Boas and Schmid in 1934. It states that glide on a given slip system commences when its resolved shear stress reaches a critical value [41, 42]. However, in 1983, Christian [43] observed non-Schmid effects experimentally in iron and other body-centered cubic (BCC)

metals. Although non-Schmid effects have been previously reported, various aspects of them are still an active field of research [44, 45, 46, 47]. The aforementioned models and numerical studies were either phenomenological, like most models in crystal plasticity or based on molecular dynamics simulations at finite temperature. Four common metals are chosen for this study: Fe (BCC), Cu (FCC), Ag (FCC) and Ni (FCC). We deliberately chose three common FCC metals in order to test the hypothesis of non-closed packedness leading to non-Schmid effects [42].

Barring a few notable exceptions [48, 49], instabilities are generally found to be of the long wavelength type and multiple authors have incorporated an elastic stability analysis to check for such long wavelength instabilities under complex loading conditions [4, 5, 6]. We aim to scrutinize the validity of such approaches by investigating the nature of instabilities in perfect crystals.

In the case of tensegrity-based metamaterials, we focus on the material symmetry phase transitions induced by presstresses. While material symmetry phase transitions in traditional lattices occur mostly due to changes in material or geometrical properties of the lattice, phase transitions due to prestressing the cables is particular of the tensegrity systems [50, 51]. A simple experimental way to modulate the prestresses of individual cables is applying coatings with distinct thermal expansion coefficients on cables.

While the traditional approaches to investigate the material symmetries were through the crystallographic considerations, new algebraic methods for finding material symmetries were introduced, which are based on examining the eigenspaces of elasticity tensor [52, 53, 54, 55]. Incorporating similar approaches to find the symmetries of a large discrete lattice through its stiffness tensor is more difficult, owing to the high dimension of the stiffness tensor. Thus, an equivalent homogenized model is desirable, which significantly reduces the dimension of the problem and allows us to obtain and examine only the equivalent elasticity tensor. Homogenization approaches have been widely used to obtain different effective properties of discrete lattices [56, 57, 58, 14], including the material symmetries

[59]. We aim to study the material symmetries of the tensegrity-based metamaterials by investigating the effective elasticity tensor. We also study possible size effects on the material symmetries of our chosen tensegrity systems. Symmetry changes solely due to size effects have previously been reported in particular crystalline materials, where it has been shown that in small enough lattice sizes, where the surface effects are sufficiently large, higher material symmetries are observed [60, 61]. Thus, we also investigate possible size effects on the symmetries of tensegrity metamaterials.

Finally we focus on the localization problem, where we investigate the effects of lattice connectivity on the formation of localized solutions -in a homogeneous system-, as opposed to the global deformations. Since it is a complex problem in its generality, we narrow it down to a specific class of lattices, 2-dimensional tensegrities; and aim to study the effect of having a connected compression path on the emergence of localized deformations. Our hypothesis is that having a disconnected set of bars, where compression is isolated, does not allow for localized solutions. To this end, we design two types of 2-dimensional lattices, with very similar geometry, except one is a tensegrity and has a disconnected set of bars, while the other has a connected set of bars. We examine their stability, and perform quasistatic compression tests to evaluate their responses.

The remainder of this thesis is structured as following: chapter 2 is devoted to our study on instabilities in lattices, where the essence of the theory for phonon and elastic stability analysis is presented as well as the results of our investigation on the single crystal metals. We focus on the material symmetry phase transitions in tensegrity-base metamaterials in chapter 3. Chapter 4 is dedicated to emergence of localized solutions in homogeneous lattices, where we discuss effects of lattice connectivity on the localization; where we focus on the case of 2-dimensional lattices. A concluding chapter along with proposed future research avenues proceeds lastly. It is worth mentioning that each chapter includes a separate introduction, which covers the relevant literature, as well as corresponding theory.

CHAPTER 2

INSTABILITIES IN LATTICES: SINGLE CRYSTALS

2.1 Introduction

[1] Onset of instabilities is key in understanding the mechanical response of nonlinear lattices subjected to large deformations and often results in significant changes in the macro or the microstructure of the lattice, which, in turn, remarkably alter the mechanical properties of the whole lattice. They have been extensively studied in both architectured lattices, or metamaterials, and natural lattices, such as metallic crystals, across several length scales.

Instabilities in architectured lattices that undergo large deformation have attracted researchers interest in the past few decades. [63] derived conditions for the onset of microscopic bifurication in cellular solids subjected finite deformations. Triantafyllidis and coworkers [64, 65, 66, 65] studied the onset of bifurication by investigating the tangent stiffness of a unit cell as a representative volume element.

Several other researchers have also studied lattice instability in atomic systems; devising techniques to study homogenous defect nucleation in crystalline solids [3, 4, 5, 6, 7, 8, 9].The abundance of defects (e.g., dislocations) in bulk crystalline materials has resulted in research focusing primarily on defect evolution or nucleation from existing ones (e.g., Frank-Read source) as opposed to defect nucleation in a perfect lattice. However, with recent advances in nanoscale devices, investigating defect nucleation in perfect lattices is gaining attention [10, 4, 3]. Barring a few notable exceptions [48, 49], instabilities are generally found to be of the long wavelength type and multiple authors have incorporated an elastic stability analysis to check for such long wavelength instabilities under complex loading conditions [4, 5, 6].

[1] The results of this chapter is published in [62].

This chapter is devoted to the topic of instabilities in lattices. We first explain the phonon stability analysis, also known as Bloch analysis, whereby we demonstrate the framework for obtaining the dynamical matrix, and illustrate the procedure through a 1-dimensional example. We then focus on elastic stability analysis; we first explain how to homogenize a discrete lattice and substitute it with an equivalent continuum, followed by stability theory in continuum mechanics. We survey different notions of convexity in elasticity theory, as the mathematical foundation of elastic stability theory in continuum mechanics. We finally present the results of our studies, using the aforementioned concepts, techniques and theories on instabilities in single crystal metals.

2.2 Phonon Stability Analysis

This section is devoted to the theory of phonon stability analysis, known as lattice dynamics in the solid state physics community. In the entire theory we rely on the following remark:

Remark. Throughout this thesis, we assume that Born-Oppenheimer approximation is valid. In simple words, this assumption allows us to identify the position of the nuclei and the atoms, neglecting the degrees of freedom associated to electrons.

In the next subsection, we will present the general theory of lattice dynamic analysis -phonon stability analysis-, and we will elaborate on the details by constructing the dynamic matrix for a 1-dimensional lattice.

2.2.1 Theory

Consider a three dimensional lattice of atoms, constructed by tessellating a unit cell over the entire $\mathbb{R}^3$. In order to avoid unnecessary complexities in the formulation, we assume each unit cell consists of a single particle of constant mass. Within the context of

the classical mechanics, we can write the potential energy of the lattice as:

$$W = \sum_{i}^{N} E_i(\mathbf{X}), \tag{2.1}$$

where $\mathbf{X}$ is the vector of positions of the atoms and E_i is the energy of the atomic site 'i'. The summations on the right hand side of (2.1) are over the entire lattice, where N is the total number of atoms. After applying a deformation to the lattice, the total potential energy could be approximated as:

$$W = W_0 + \frac{1}{2} \sum_{i=1}^{N} \sum_{\substack{j=1 \\ j \neq i}}^{N} \mathbf{u_i} \mathbf{K}(\mathbf{x_i}, \mathbf{x_j}) \mathbf{u_j}, \tag{2.2}$$

where position and displacement of atom 'i' in the deformed configuration is respectively shown as $\mathbf{x_i}$ and $\mathbf{u_i}$, where $\mathbf{x_i} = \mathbf{X_i} + \mathbf{u_i}$. Eq.(2.1) is obtained by linearizing the energy (up to the second order) around the equilibrium in the deformed configuration, while W_0 is energy at the undeformed configuration. Note that the first derivative of energy vanishes by equilibrium. This method is known as quasi-harmonic approximation. We remark here that the only distinction between harmonic and quasi-harmonic approximation -widely used in the literature- is that in the former, energy is linearized around the undeformed configuration. We have:

$$K_{pq}(\mathbf{x_i}, \mathbf{x_j}) = \frac{\partial^2 W}{\partial x_i^p \partial x_j^q}. \tag{2.3}$$

The classical equation of motion of the nuclei, after the linearization (2.2), can be written as:

$$m\ddot{\mathbf{u}}_\mathbf{i} = -\sum_{j=1}^{N} \mathbf{K}(\mathbf{x_i}, \mathbf{x_j}) \mathbf{u_j}. \tag{2.4}$$

To solve 2.4, we assume a general form of solutions for the second order differential equation as $\mathbf{u_i(t)} = \bar{\mathbf{u}}_\mathbf{i} e^{i\omega t}$.This leads to:

$$m\omega^2 \bar{\mathbf{u}}_\mathbf{i} = \sum_{j=1}^{N} \mathbf{K}(\mathbf{x_i}, \mathbf{x_j}) \bar{\mathbf{u}}_\mathbf{j}. \tag{2.5}$$

We employ the periodicity of the lattice, allowing us to write $\mathbf{x_i} = \mathbf{n_i}.\mathbf{G}$ where $n \in Z^3$ and $\mathbf{G}$ is the matrix where each column represents a basis vector of the lattice. So one can write $\mathbf{K}(\mathbf{x_i}, \mathbf{x_j}) = \mathbf{K}(\mathbf{n_i}, \mathbf{n_j})$. From translational invariance of the lattice, it follows that:

$$\mathbf{K}(\mathbf{n_i}, \mathbf{n_j}) = \mathbf{K}(\mathbf{n_i} - \mathbf{n_j}). \tag{2.6}$$

Using discrete Fourier Transform we can write:

$$\bar{\mathbf{u}}(\mathbf{x_i}) = \frac{1}{\sqrt{m}} \sum_{h=1}^{N} \hat{\mathbf{u}}_h e^{i\boldsymbol{\kappa}_h.\mathbf{x_i}}, \tag{2.7}$$

where $\hat{u}_h$ is related to the amplitude of the displacement. κ is known as wave vector and is spanned in the 'reciprocal basis'. Using 2.7 we can write:

$$\omega^2(\boldsymbol{\kappa})\hat{\mathbf{u}}(\boldsymbol{\kappa}) = \mathbf{D}(\boldsymbol{\kappa})\hat{\mathbf{u}}(\boldsymbol{\kappa}). \tag{2.8}$$

Note that the above equation is obtained by imposing the orthogonality of Fourier basis. $\mathbf{D}(\boldsymbol{\kappa})$ is called the dynamic matrix and equals:

$$\mathbf{D}(\boldsymbol{\kappa}) = \frac{1}{m} \sum_{j} \mathbf{K}(\mathbf{n_i} - \mathbf{n_j}) e^{i\boldsymbol{\kappa}(\mathbf{x_i} - \mathbf{x_j})}. \tag{2.9}$$

Eq. (2.8) gives us the dispersion relations. We remark that since the choice of $\mathbf{n_i}$ will not change the results, i is usually chosen to be zero, referring to the atom in the unit cell corresponding to the origin. Let us also remark that if only the vibrational frequency $\omega(\boldsymbol{\kappa})$ of

a mode itself is relevant, the classical treatment gives already a good answer (which is why physicists could understand experimentally measured phonon band structure with classical analysis). On the other hand, if the energy connected to each mode $\omega(\boldsymbol{\kappa})$ is important, or more precisely, the way how one populates modes is concerned, then the classical picture will fail. The prototypical example of this is the specific heat due to the lattice vibrations, which simply mounts to how effectively the vibrational modes of the lattice can take up thermal energy.

The general setup explained above is elaborated in the next subsection for the simplest case, a 1-dimensional lattice.

1D Example

Let us now demonstrate the detailed steps for block-diagonalizing hidden in the phonon stability analysis formulation. We avoid unnecessary complications by considering a monoatomic 1-dimensional infinite chain, as shown in Figure 2.1.

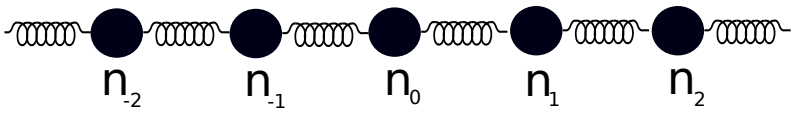

Figure 2.1: 1-dimensional monoatomic chain. The distance between each pair of atoms is 'a'.

We can write the potential energy of the whole lattice as:

$$W = \sum_{i=-N}^{N} \frac{1}{2} k (x_{i+1} - x_i)^2, \tag{2.10}$$

where W is the total energy, x_i is the position of the atom n_i, N is the total number of atoms and k is the stiffness of the 'spring' connecting neighbors. Note that k is only considered as a constant, in the interest of simplicity. Also, N tends to infinity in our calculations.

The equilibrium for each atom is obtained by solving $\frac{\partial W}{\partial x_i} = 0$, through a Newton iterative method, which requires the second derivative of energy or the stiffness matrix. The stiffness matrix consists of submatrices, each associated to a unit cell of the lattice. Below, we write the equilibrium equation for a single unit cell:

$$\begin{pmatrix} K_1 & K_2 & 0 \\ K_2 & K_1 & K_2 \\ 0 & K_2 & K_1 \end{pmatrix} \begin{pmatrix} \delta u[-1] \\ \delta u[0] \\ \delta u[1] \end{pmatrix} = \begin{pmatrix} m\delta\ddot{u}[-1] \\ \delta\ddot{u}[0] \\ \delta\ddot{u}[1] \end{pmatrix}. \tag{2.11}$$

We denote the stiffness components as K_1 and K_2. Also, m is the mass of each atom, and without loss of generality, we assume it is equal to identity. Using *discrete Fourier transform*, we can write:

$$\delta u[n] = \sum_{h=-N}^{N-1} \delta\hat{u}[h] \exp -i\kappa[h]x[n], \tag{2.12}$$

where

$$\kappa[h] = 2\pi \frac{h}{2N} \frac{1}{a}, \ -N \leq h < N. \tag{2.13}$$

Note that a is the bond length. Now we take the following steps:

- Insert (2.12) in (2.11).
- Multiply both sides of each of the three of equations obtained from (2.11) by $\exp i\kappa[h']x[n]$, where $n = -1$, $n = 0$ and $n = 1$ for the first, second and third equation respectively.
- Sum all the three equations.
- The right hand side of the sum equation, using the *inverse Fourier transform*, would lead to $\delta\ddot{\hat{u}}[h']$.
- Incorporate translational invariance. Replace $x[1] = x[0] + a$ and $x[-1] = x[0] - a$ in the left hand side.

- Use the geometric sum $\sum_l \exp\left(\kappa[h] - \kappa[h']\right)x[l]]\delta_{hh'}$, where $\delta_{hh'}$ is identity when $h = h'$ and zero otherwise.

As a result of the above steps, assuming that $x[0] = 0$, we get the following:

$$(K_1 + K_2 \exp -i\kappa[h']a + K_2 \exp i\kappa[h']a)\hat{u}[h'] = \ddot{\hat{u}}. \tag{2.14}$$

It is obvious that (2.14) decouples the displacements, presenting an 'equivalent' stiffness in the 'wave-vector' space.

We remark here that the above procedure can easily be extended to multi-atom unit cells as well as higher dimensions. As the reader might have noticed, the core of above computations is change of basis to Fourier space and incorporating the translational invariance, which is valid for periodic systems. We also note that the above procedure has a continuous counterpart, where displacement of a periodic continuous media could be written in Fourier basis, as the underlying Hilbert space.

2.2.2 Symmetries of the dynamical matrix

A great deal of information about the dispersion of the lattice vibrations could be extracted from the symmetries. Some of the main and basic symmetries that lead to interesting observations are briefly discussed as follows:

1. The translational invariance of the lattice and reciprocal lattice:

Using these symmetries, one can prove that the dynamical matrix (2.9) is Hermitian, i.e. $D^{T*} = D^{\dagger} = D$. The proof is based on the symmetry of the second derivative and translational symmetry of the lattice. Based on the properties of the Hermitian operators, the eigenvalues ω^2 are real. This means that either ω are real or they are purely imaginary. We will assume the former. The latter yields pure exponential growth of our Fourier solution, indicating an instability of the lattice to a second-order structural phase transition.

2. The point group symmetries of the lattice and reciprocal lattice: A point group

operation takes a crystal back to an identical configuration. Both the original and final lattice must have the same dispersion. Thus, since the reciprocal lattice has the same point group as the real lattice, the dispersion relations have the same point group symmetry as the lattice.

3. Time-reversal invariance: Time reversal symmetry, which in the wave vector space implies equivalence of wave moving to the left or right, causes the mirror symmetry of the dispersion curve. In other words $\omega(\boldsymbol{\kappa}) = \omega(-\boldsymbol{\kappa})$.

2.3 Elastic Stability Analysis

We now turn our attention to stabiltiy analysis in the context of continuum mechanics. We first demonstrate how to homogenize a discrete lattice, substitute it with an equivalent continuum and obtain the effective elastic properties. We finally delve into the mathematical foundations of stability theory.

2.3.1 Homogenization and Cauchy-Born rule

In order to formulate a constitutive law for a continuum from the atomic interactions of the discrete crystal that underlies it, we must hypothesize a connection between the continuum displacement field and the motion of atoms. The standard reasoning consistent with the locality approximation of continuum mechanics is that the atomic environment at a continuum point is characterized by the deformation gradient there; this is referred to as the Cauchy-Born (CB) hypothesis. Thus, each continuum point is taken to represent a large, essentially infinite, region on the atomic scale which is homogeneously distorted according to the deformation gradient at the point [67]. We will rigorously state the CB hypothesis for a lattice with a single atom unit cell.

Let Ω_L be the set of union of the coordinates of all the atoms in a lattice in $\mathbb{R}^3$ and L be the diameter of the Ω_L. Let $\phi : \Omega_L \to \mathbb{R}^3$ be a mapping, where $\phi(\mathbf{x})$ denotes the position of the particle $\mathbf{x} \in \Omega_L$ in the deformed configuration. Let also the continuum, where each

point of the continuum is defined by $\lim_{L\to\infty}\Omega_L$, be subjected to an affine deformation gradient $\mathbf{F}$. The strain energy density of the lattice is obtained by:

$$W(\mathbf{F}) := \lim_{L\to\infty} \min_{\substack{\mathbf{x}\in\Omega_L \\ \phi(\mathbf{x})|_{\mathbf{x}\in\partial\Omega_L}=\mathbf{F}\mathbf{x}}} \frac{1}{vol(\Omega_L)} E[\phi(\mathbf{x})|_{\mathbf{x}\in\Omega_L}], \tag{2.15}$$

where $vol(\Omega_L)$ and $E[\phi(\mathbf{x})]$ are the volume of the region in $\mathbb{R}^3$ occupied by the lattice and the energy of the lattice in the deformed configuration, respectively. Also, $\partial\Omega_L$ is the union of the atoms in the boundary of the lattice. We remark here that several subtleties exist in the definition, which we skip here in the interest of simplicity. Those include the precise definition of the boundary and its regularity, passing to the limit and the existence of the limit, and conditions on the mapping ϕ as a function of an affine deformation gradient. CB hypothesis postulates that $W(\mathbf{F}) = W_{CB}(\mathbf{F})$, where:

$$W_{CB}(\mathbf{F}) := \lim_{L\to\infty} \frac{1}{vol(\Omega_L)} E[\mathbf{F}\mathbf{x}|_{\mathbf{x}\in\Omega_L}]. \tag{2.16}$$

In other words, it postulates that the minimum in (2.15) is attained when each unit cell individually follows the prescribed affine deformation.

In the next section, under the CB assumption, we demonstrate how to compute the effective elasticity tensor of a discrete medium with a complex unit cell.

2.3.2 Effective elasticity tensor of a periodic lattice

Following CB rule, we assume that the strain energy of a single unit cell normalized by its volume ($\tilde{W}$) located in the interior of a very large lattice with its boundary subjected to an affine deformation gradient $\mathbf{F}$ is equivalent with the strain energy density of a hyper-elastic continuum (W). By definition, W is solely a function of $\mathbf{F}$:

$$W(\mathbf{F}) = \tilde{W}(\mathbf{x}, \mathbf{F}), \tag{2.17}$$

where $\mathbf{x}$ is a $3N$ dimensional vector containing the position vectors of all the N nodes in a unit cell in the deformed configurations. We remark here that the equivalence in energy in (3.18) is obtained by taking the limit of the strain energy density as the volume of the lattice tends to infinity [68]. Note that $\mathbf{x} = \{\mathbf{x}_i, \mathbf{x}_m, \mathbf{x}_s\}$ and $\mathbf{x}_s$ is related to $\mathbf{x}_m$ and initial configuration as $\mathbf{x}_s = \mathbf{x}_m + \mathbf{F}(\mathbf{X}_s - \mathbf{X}_m)$. Thus we can write $\tilde{W}(\mathbf{x}, \mathbf{F}) = \overline{W}(\mathbf{x}_u, \mathbf{F})$, where $\mathbf{x}_u$ is the union of $\mathbf{x}_i$ and $\mathbf{x}_m$. Let us remark that in a complex lattice like ours, due to internal degrees of freedom, $\mathbf{x}_u$ must be obtained by minimizing the energy of a single unit cell [67].

The first elasticity tensor is defined as $\mathbf{C} = \frac{\partial^2 W}{\partial \mathbf{F} \partial \mathbf{F}}$, which is computed as:

$$\mathbf{C} = \frac{\partial^2 \overline{W}}{\partial \mathbf{F} \partial \mathbf{F}} + \frac{\partial^2 \overline{W}}{\partial \mathbf{F} \partial \mathbf{x}_u} \frac{\partial \mathbf{x}_u}{\partial \mathbf{F}}. \tag{2.18}$$

Note that (3.19) is obtained by assuming equilibrium. Using the equilibrium of the unit cell, we can write the following:

$$\begin{aligned} &\frac{\partial \overline{W}}{\partial \mathbf{x}_u} = 0 \implies \frac{d}{d\mathbf{F}} \left(\frac{\partial \overline{W}}{\partial \mathbf{x}_u} \right) = 0, \\ &\frac{d}{d\mathbf{F}} \left(\frac{\partial \overline{W}}{\partial \mathbf{x}_u} \right) = \frac{\partial^2 \overline{W}}{\partial \mathbf{x}_u \partial \mathbf{F}} + \frac{\partial^2 \overline{W}}{\partial \mathbf{x}_u \partial \mathbf{x}_u} \frac{\partial \mathbf{x}_u}{\partial \mathbf{F}} = 0. \end{aligned} \tag{2.19}$$

By computing $\frac{\partial \mathbf{x}_u}{\partial \mathbf{F}}$ from (3.20) and plugging in (3.19), we obtain:

$$\mathbf{C} = \frac{\partial^2 \overline{W}}{\partial \mathbf{F} \partial \mathbf{F}} - \frac{\partial^2 \overline{W}}{\partial \mathbf{F} \partial \mathbf{x}_u} \left(\frac{\partial^2 \overline{W}}{\partial \mathbf{x}_u \partial \mathbf{x}_u} \right)^{-1} \frac{\partial^2 \overline{W}}{\partial \mathbf{x}_u \partial \mathbf{F}}. \tag{2.20}$$

We compute the derivatives of $\overline{W}$ in (3.21) with respect to $\mathbf{F}$ as follows:

$$\begin{aligned}
\frac{\partial^2 \overline{W}}{\partial F_{ij} \partial F_{kl}} &= \sum_{r=1}^{N_s} \sum_{p=1}^{N_s} \frac{\partial^2 \overline{W}}{\partial x^i_{sr} \partial x^k_{sp}} (X^j_{sr} - X^j_{mr})(X^l_{sp} - X^l_{mp}), \\
\frac{\partial^2 \overline{W}}{\partial \mathbf{x}_u \partial F_{ij}} &= \sum_{r=1}^{N_s} \frac{\partial^2 \overline{W}}{\partial \mathbf{x}_u \partial x^i_{sr}} (X^j_{sr} - X^j_{mr}), \\
\frac{\partial^2 \overline{W}}{\partial \mathbf{F} \partial \mathbf{x}_u} &= \left(\frac{\partial^2 \overline{W}}{\partial \mathbf{x}_u \partial \mathbf{F}} \right)^T,
\end{aligned} \tag{2.21}$$

where $i, j, k, l \in \{1, 2, 3\}$ and N_s is the number of slave nodes. Note that we assume $\overline{W}$ is twice differentiable.

2.3.3 Stability in continuum elasticity theory

This section is devoted to the mathematical foundations of stability theory in the context of elasticity theory. This section is essentially based on the notes of professor John Ball, which has been the primary source of learning the topic for the author. To lay the foundations of the matter, let us consider the variational formulation of the nonlinear elastostatics. Let us define a motion by a sufficiently smooth map $y : \Omega \times [t_1, t_2] \to \mathbb{R}^3$, $y = y(x, t)$ and the corresponding deformation gradient as:

$$F = Dy(x, t), \;\; F_{ij} = \frac{\partial y_i}{\partial x_j}, \tag{2.22}$$

where $F \in M^{n \times n}_+$ where $M^{n \times n}_+ = \{\text{real } n \times n \text{ matrices with positive determinant}\}$. We note that imposing a positive determinant on the deformation gradient ensures that the deformation is orientation preserving as well as invertibile, only if $y(x, t)$ and Ω satisfies certain regularity conditions.

The total elastic energy corresponding to the deformation $y = y(x)$ is given by

$$I(y) = \int_\Omega W(Dy(x)) dx, \tag{2.23}$$

where $W = W(F)$ is the stored-energy function of the material and assumed to be C^1. Also, we assume it is always nonnegative. The key question is the existence of minimizers of I subject to certain boundary conditions. To lay down the framework, first we need to specify the space of functions that we will work in, as well as the properties that W should satisfy. The answer to the first question is the Sobolev spaces. We will define one family of Sobolev space, $W^{1,p}$ -which will be trivial for the reader familiar with functional analysis-, as the following:

$$\begin{aligned} W^{1,p} &= \{y : \Omega \to \mathbb{R}^3 : ||y||_{1,p} < \infty\} \\ ||y||_{1,p} &= \Big(\int_\Omega |y(x)|^p + |Dy(x)|^p dx \Big)^{\frac{1}{p}}, \end{aligned} \tag{2.24}$$

where $1 \leq p < \infty$ and Dy is interpreted in the weak sense, that is:

$$\int_\Omega \frac{\partial y_i}{\partial x_j} \phi_i dx = -\int_\Omega y_i \frac{\partial \phi_i}{\partial x_j} dx, \ \ \forall \phi \in C_0^\infty(\Omega). \tag{2.25}$$

We assume that y belongs to the largest Sobolev space, that is $p = 1$, so that in particular Dy is well defined a.e $x \in \Omega$ and $I(y) \in [0, \infty]$.

Thus we formulate the problem as if there exists $y^* \in W^{1,1}$ to minimize (2.23), while simultaneously satisfying the associated boundary conditions. The existence of a minimizer requires certain constraints on the energy function. In other words, we restrict ourselves to certain subspaces of the $W^{1,1}$. To make things more clear, we first focus on 1-dimensional elasticity, and then extend the proposed concepts and conditions to 3-dimensional elasticity.

1D elasticity

Let us consider an inhomogeneous 1-dimensional elastic material with $\Omega = (0, 1)$, with corresponding total elastic energy as

$$I(y) = \int_0^1 W(x, Dy) dx. \tag{2.26}$$

Our goal is to minimize I in the set of admissible deformations $\mathcal{A}$, defined as:

$$\mathcal{A} = y \in W^{1,1}(0,1) : Dy(x) > 0 a.e., y(0) = \alpha, y(1) = \beta, \tag{2.27}$$

where $\alpha < \beta$.

We make the following hypotheses on W, and then prove the existence of a minimizer:

- $W : [0,1] \times (0,\infty) \to [0,\infty)$ is continuous.
- $W(x,y) \to \infty$ as $y \to 0+$. Note that we also consider $W(x,y) = \infty$ if $p \leq 0$.
- $\Psi(y) \leq W(x,y) \forall p > 0, x \in (0,1)$, where $\Psi : (0,\infty) \to [0,\infty)$ is continuous with the growth condition $\lim_{p\to\infty} \frac{\Psi(p)}{p} = \infty$.
- W(x,y) is convex in y, that is $W(x, \lambda y + (1-\lambda)y') \leq \lambda W(x,y) + (1-\lambda)W(x,y') \forall y > 0, y' > 0, \lambda \in (0,1), x \in (0,1)$.

We note that the last condition is equivalent to a non decreasing stress ($W_{Dy}(x, Dy)$), given that W is C^1.

Theorem. Under the above hypotheses, there exists y^* that minimizes I in $\mathcal{A}$.

Proof:

First we note that $\mathcal{A}$ is nonempty, since $z(x) = \alpha + (\beta - \alpha)x$ belongs to $\mathcal{A}$. Let us denote $l = \inf_{y\in\mathcal{A}} I(y)$. Since W is nonnegative and continuous $0 \leq l$. Now let y^j be a minimizing sequence, i.e. $y^j \in \mathcal{A}$, $I(y^j) \to l$ to $j \to \infty$. Since $\int_\Omega \Psi(Dy^j)dx \leq M < \infty$, there exists a subsequence, which we call -by abuse of notation- Dy^j, converging weakly in $L^1(0,1)$ to some z [69]. Now we define $y^*(x) = \alpha + \int_0^x z(s)ds$, so that $Dy^* = z$. Then $y^j(x) = \alpha + \int_0^x Dy^j(s)ds \to y^*(x) \, \forall x \in [0,1]$. In particular $y^*(0) = \alpha$, $y^*(1) = \beta$. Now by Banach-Mazur theorem, there exists a sequence $z^k = \sum_{j=k}^{\infty} \lambda_j^k Dy^j$ of finite convex combinations of the Dy^j converging strongly to z, and so without loss of generality a.e. By

convexity

$$\int_0^1 W(x, z^k)dx \leq \int_0^1 \sum_{j=k}^{\infty} \lambda_j^k W(x, Dy^j)dx \leq \sup_{j\geq k} \int_0^1 W(x, Dy^j)dx. \tag{2.28}$$

Letting $k \to \infty$, by Fatou's lemma

$$\int_0^1 W(x, Dy^*)dx = \int_0^1 W(x, z)dx \leq l. \tag{2.29}$$

This also implies that $Dy^* > 0$ a.e. and so $y^*\mathcal{A}$. Hence we proved

$$l \leq I(y^*) \leq l, \tag{2.30}$$

which implies $I(y^*) = l$ and y^* is a minimizer.

The above theorem was presented to show how convexity will lead to existence of a minimizer, given some additional conditions are satisfied. The key difference between the 1-dimensional case and higher dimensional case, is the lack of convexity in the higher dimensions. We devote the next subsection to this subject.

Convexity in 3D elasticity

As hinted before, the elastic energy functional is never convex in 3-dimensions, corroborated by the following facts:

- 1. W is frame indifferent, that is

$$W(RF) = W(F), \forall R \in M_+^{3\times 3} \tag{2.31}$$

For a detailed discussion, the reader is referred to [70, 71]. This is because $M_+^{3\times 3}$ is

not convex. This could be easily verified by considering matrices A and B as follows:

$$\begin{aligned} &A = \text{diag}(1,1,1),\ \ B = \text{diag}(-1,-1,1) \\ &W(\frac{1}{2}(A+B)) = \infty > \frac{1}{2}W(A) + \frac{1}{2}W(B). \end{aligned} \tag{2.32}$$

This implies that a energy functional that is convex in 1-dimensional space, will not be convex in higher dimensions.

- 2. If W is convex, then any equilibrium solution -solution of the Euler-Lagrange equation- is an absolute minimizer of the elastic energy:

$$I(y) = \int_\Omega W(Dy)dx. \tag{2.33}$$

This is easily proven, by considering $z \in \mathcal{A}$ and linearizing around y:

$$I(z) = \int_\Omega W(Dz)dx \geq \int_\Omega W(Dy) + DW(Dy).(Dz - Dy)dx = I(y). \tag{2.34}$$

Note that the second term on the right hand side of the inequality goes to zero, since DW is the first PK stress and is zero, due to equilibrium. This contradicts experimental results which suggest non-unique equilibria, e.g. buckling.

With this introduction, other measures of convexity are defined in higher dimensions, which are briefly described in Appendix. A.

2.4 Instabilities in single crystal metals

2.4.1 Phonon stability analysis of single crystal metals

When a perfect single crystal is subjected to a deformation such that the energy at a lattice site exceeds the Pierels energy barrier, dislocations are nucleated there and move towards the boundary[72]. Dislocation nucleation in a perfect crystal can be identified

with the onset of an instability under appropriate loading conditions, which breaks the local translational symmetry. Thus studying lattice instabilities provide useful insights into the mechanics of defect nucleation in single crystals, which is identified with the onset of plasticity. We investigate two important aspects of the nature of defect nucleation in metallic crystals: I) Schmid Law; II) the type of instabilities.

Schmid law in crystal plasticity, which governs dislocation motion [73, 74, 42], was proposed by Boas and Schmid in 1934. It states that glide on a given slip system commences when its resolved shear stress reaches a critical value [41, 42]. Later, Bridgman conducted several experiments on a sample under various hydrostatic pressures and concluded that the yield stress is independent of the hydrostatic pressure [75]. However, in 1983, Christian [43] observed non-Schmid effects experimentally in iron and other body-centered cubic (BCC) metals. Similar behaviors were observed in several alloys [76, 77, 45], like Ni_3Al and NiTi [78, 79], and crystal plasticity models based on non-Schmid effects have been proposed [78, 74, 80]. These models attribute non-Schmid effects to the non-closed packedness present in BCC single crystals. Molecular dynamics simulations have also been employed to study non-Schmid effects in various materials [42, 73, 81]. Although non-Schmid effects have been previously reported, various aspects of them are still an active field of research [44, 45, 46, 47]. The aforementioned models and numerical studies were either phenomenological, like most models in crystal plasticity or based on molecular dynamics simulations at finite temperature.

Four common metals are chosen for this study: Fe (BCC), Cu (FCC), Ag (FCC) and Ni (FCC). We deliberately chose three common FCC metals in order to test the hypothesis of non-closed packedness leading to non-Schmid effects [42]. Defect nucleation is identified by lattice instability analysis using phonon calculations. We model inter-atomic interactions through Mishin potentials, which belong to the widely adopted class of Embedded-Atom Method (EAM) potentials [82, 83, 84, 85]. It is worth mentioning that these potentials are obtained through *ab initio* calculations and are presented in the form of tabulated

data, which lead to non-constant coefficients for the assumed EAM form. While there are controversies on accuracy of potentials on predicting defect evolution, they are reliable for studying the onset of instabilities [86, 4, 10, 3, 5]. To avoid the extra complexities of having a finite temperature, we also consider the temperature to be zero. Each lattice system is constructed using its standard primitive vectors written in the standard basis [87]. Imposing periodic boundary conditions implies solving for an infinite lattice or the interior of a sufficiently large lattice such that surface effects are not encountered. We subject the atoms at the boundary of the lattice to an affine deformation with deformation gradient $\mathbf{F}$. The deformed configuration of the boundary is obtained by $\mathbf{x} = \mathbf{F}\mathbf{X}$, where $\mathbf{x}$ and $\mathbf{X}$ are the position vectors of the atoms in the deformed and the reference configurations, respectively.

In our study, the applied deformation gradient consists of a hydrostatic component β and a simple shear part γ, as follows

$$\mathbf{F} = \begin{bmatrix} 1+\beta & \gamma & 0 \\ 0 & 1+\beta & 0 \\ 0 & 0 & 1+\beta \end{bmatrix}.$$

This particular choice of $\mathbf{F}$ is motivated by our objective to investigate the effect of hydrostatic deformation β on the shear value at the instability point, which we indicate as γ_d. Also, for the sake of consistency in both lattice systems, $\mathbf{F}$ is written in the standard basis. An alternate approach to examine the Schmid law would consist in applying $\mathbf{F}$ in a coordinate system in which two of the basis vectors lie within one of the slip planes (for FCC). Note that this would result in the same hydrostatic deformation as in our approach, given the hydrostatic component of the deformation gradient is invariant under a coordinate transformation. We believe this indirect way of subjecting the slip plane to shear loading allows us to compare the shear-normal coupling in FCC and BCC metals under identical deformation gradient.

The deformation gradient $\mathbf{F}$ is applied in two stages: We first subject the lattice to a

hydrostatic deformation (β) and then impose shear deformation (γ). At a fixed β, shear deformation is increased from 0 in small steps until the onset of instability, at $\gamma = \gamma_d$.This procedure is performed for 61 different values of β, spanning from -0.03 to 0.03.

Note that under this procedure the lattice undergoes an affine deformation, and that an affine displacement for atoms is always a valid equilibrium solution for the lattice, owing to translational symmetry. As the deformation increases, this affine deformation solution becomes unstable and a defect nucleates. Indeed, since the affine deformation is stable to infinitesimal perturbations before the instability point, no defect nucleates under quasistatic loading. The nucleation of defects in a real single crystal beyond this critical deformation point will depend on finite size effects and on the nature of perturbations in the lattice. Our procedure thus seeks to identify a lower bound for the yield strength of the material under the considered boundary conditions. It is worth emphasizing that our approach accounts for nucleation in the bulk of the system and does not consider the surface effects.

We seek to identify the instability point by analyzing the stability under infinitesimal perturbations in the Fourier space, corresponding to a phonon stability analysis [88, 67] (as described in details in chapter 2). Since instabilities are associated with the loss of positive definiteness of the Hessian of the energy functional, we use a second order approximation about the deformed configuration. This method is also known as quasi-harmonic approximation (QHA) where we allow the frequencies to be dependent on the deformation [89]. We remark here that our analysis in the reciprocal lattice space of a single unit cell allows instabilities of arbitrary wavelengths. The equilibrium of an arbitrary atom 'r' located in the interior, far from the boundary can be written as:

$$\sum_{s=1}^{N} \mathbf{K}_{rs} \delta \mathbf{u}_s = \delta \mathbf{f}_r, \tag{2.35}$$

where N is the number of atoms in the lattice. $\mathbf{K}$ and $\delta\mathbf{u}$ are, respectively, the second derivative of the potential energy with respect to atomic coordinates and the change in displacement with respect to the deformed configuration due to force perturbation, $\delta\mathbf{f}$. Note

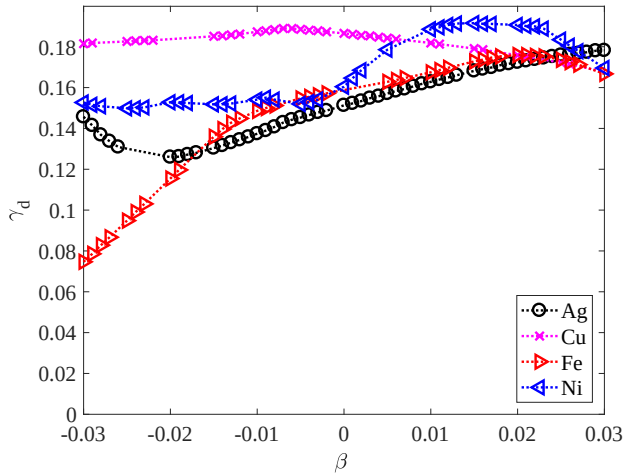

Figure 2.2: Shear deformation at the onset of instability (γ_d) vs. Hydrostatic deformation (β): phonon stability results demonstrate a significant shear-normal coupling.

that at the equilibrium, $\mathbf{f}_r = 0$. Without loss of generality, the origin is placed at the atom 'r' and the discrete Fourier transform of $\delta\mathbf{u}$ is written as:

$$\delta\mathbf{u}_s = \sum_{h=1}^{N} e^{-i\mathbf{k}_h \cdot \mathbf{x}_s} \delta\hat{\mathbf{u}}_h, \tag{2.36}$$

where $\mathbf{k}$ and $\delta\hat{\mathbf{u}}$ are wave vector in the reciprocal basis and the Fourier transform of the displacement perturbation, respectively. Similarly, $\mathbf{x}_s$ is the position vector of atom 's' in the deformed configuration. Substituting Eq. 2.36 into Eq. 2.35 and employing periodicity and orthogonality of the Fourier basis leads to:

$$\sum_{s=1}^{N} \mathbf{K}_{rs} e^{-i\boldsymbol{\kappa}.\mathbf{x}_s} \delta\hat{\mathbf{u}}_r = \delta\hat{\mathbf{f}}_r, \tag{2.37}$$

where similarly $\delta\hat{\mathbf{f}}$ is the force perturbation in the Fourier space. Eq. 2.37 is written for a fixed wave vector $\mathbf{k} = \boldsymbol{\kappa}$. Lattice instability is identified by the loss of positive definiteness of the stiffness matrix $\sum_{s=1}^{N} \mathbf{K}_{rs} e^{-i\boldsymbol{\kappa}.\mathbf{x}_s}$. The analysis is performed by looking at the entire first Brillouin Zone (BZ), which is shown in Fig. 2.4 for both BCC and FCC lattices, in the deformed configuration.

The dependence of the shear at the onset of instability, γ_d, on the hydrostatic deformation β is illustrated in Fig. 2.2. Since Schmid law focuses on the stress values, it is worth emphasizing that this dependency in the deformation space is an indirect way of investigating dependency in the stress space. Indeed, an independency of critical shear stress τ_c on hydrostatic pressure P implies an independency of the critical shear deformation γ_d on the hydrostatic deformation β. Note that the form of dependency $\tau_c(P)$ can be different, in general, from $\gamma_d(\beta)$ due to geometric and material nonlinear effects. Schmid law implies a horizontal line, i.e. the critical shear deformation γ_d is independent of the hydrostatic deformation β. As mentioned previously, there is experimental evidence of non-Schmid effects in BCC metals, while FCC metals are considered to follow the Schmid plasticity [42]. Indeed, a strong coupling exists in iron (BCC). However, Fig. 2.2 illustrates that hydrostatic deformation significantly affects shear instabilities in FCC metals too. We observe that the trend and extent of shear normal coupling are considerably different in various materials. While silver does not exhibit Schmid type behavior, copper and nickel follow closely the Schmid assumption in a vast regime of deformations.

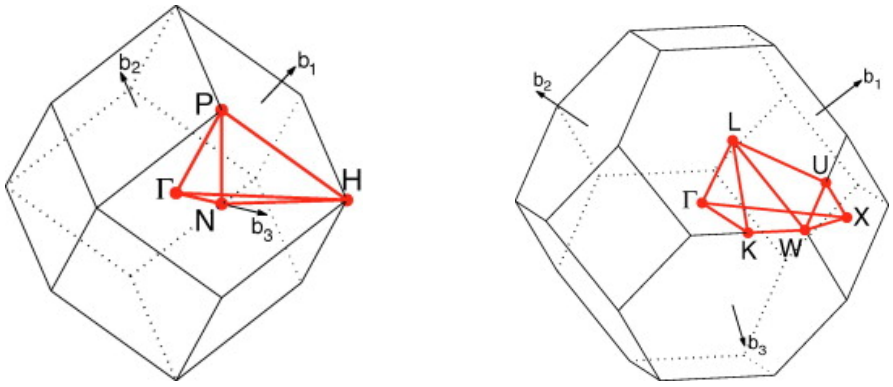

(a) (b)

Figure 2.4: First Brillouin zone for: (a) BCC and (b) FCC lattices. The polygon in red is representing the associated irreducible Brillouin zone. The figures are borrowed from [87] .

To investigate the nature of instabilities, after the wave vector associated with the instability point (i.e. $\boldsymbol{\kappa}_d$) is computed, we look at all the wave vectors along the line connecting Γ to the boundary of the first BZ, passing through $\boldsymbol{\kappa}_d$. If the phonon softens along the entire line (eigenvalues become zero), it corresponds to a long wavelength instability. On

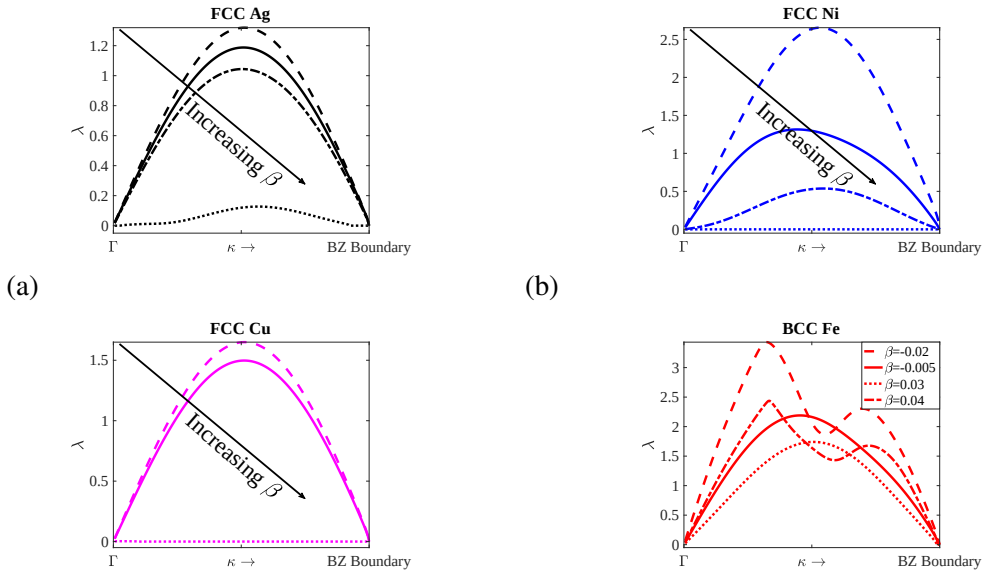

Figure 2.3: Transition from short to long wavelength instability, as hydrostatic pressure β increases there is a transition to long wavelength in FCC metals. (a)-(d) represents square root of the minimum eigenvalue, λ, along the path connecting the center of BZ (Γ) to the wave vector associated with the instability on the BZ boundary $\boldsymbol{\kappa}_d$. Each graph is at the shear leading to instability for a fixed β (a) Silver: $\beta \in \{-0.015, 0.0, 0.015, 0.045\}$. Transition point is at $\beta = 0.04$. (b) Nickel: $\beta \in \{-0.03, 0.005, 0.03, 0.035\}$. Transition point is at $\beta = 0.032$ (c) Copper: $\beta \in \{-0.025, -0.01, 0.005\}$. Transition point is at $\beta = -0.006$ (hydrostatic compression). (d) Iron: $\beta \in \{-0.02, -0.005, 0.03, 0.04\}$ All instabilities are of short wavelength nature.

the other hand, nonzero eigenvalues close to $\kappa = 0$ and along that path imply short wavelength instability. We performed this calculation for all the loading conditions. Note that the square root of the minimum eigenvalue of the stiffness matrix, denoted by λ, is proportional to the frequency of the acoustic modes. Fig. 2.3 shows λ values for the considered materials. We remark that the wavelengths associated with short wavelength instabilities are in the range of 1 to 3 times the interatomic distances. Also, the instability points in the short wavelength cases are at the L and P points [87] of the deformed reciprocal lattice Brillouin zone in the FCC and BCC lattices, respectively. For each material, four different β values are chosen and their associated λ values are plotted along the aforementioned path. We observe that for $\beta < 0$, i.e. hydrostatic compression, instabilities of short wavelength happen in the Ag, Ni and Fe. In Ni, Cu and Ag, a transition from short to long wavelength instabilities occurs. The transition point depends significantly on the material: it happens around $\beta = -0.005$ for Cu, while it only happens, at $\beta = 0.04$ for Ag. To illustrate these transitions, we choose distinct β values for various metals in Fig. 2.3. We also observe

that instabilities in iron are always of a short wavelength nature (in the chosen deformation regime). We remark here that, the difference in the nature of instabilities in compression and tension, reflects the tension-compression asymmetry in metals [90]. While the existence and possibility of having short wavelength instabilities have been shown previously [91, 49], our results demonstrate an abundance of such short wavelength instabilities. Since short wavelength instabilities do not have a simple homogenized continuum analogue, they cannot be captured by a first order continuum model. Based on our results, the widespread practice of using an elastic stability analysis to study nanoindentation and uniaxial tension at the nanoscale may have led to erroneous results [4, 5, 6]. We observe that the type of instability is dependent on both the material and the loading conditions.

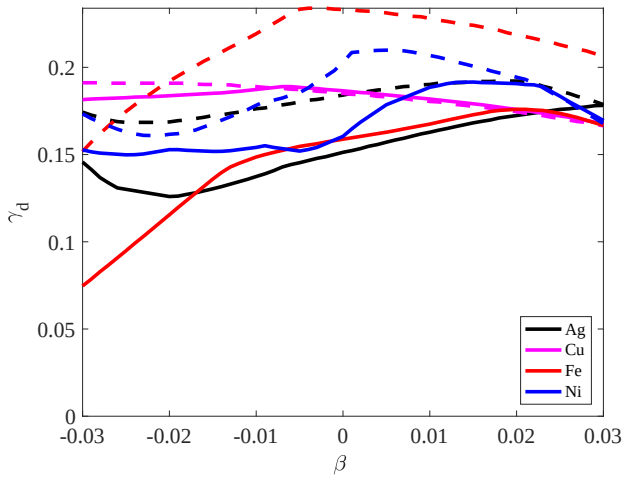

Figure 2.5: Comparison of elastic (dashed) and phonon (solid) stability analyses: They are equivalent when instabilities are of long wavelength type, e.g. in Cu for $\beta > -0.006$. When short wavelength instabilities occur, elastic stability predicts a significantly higher γ_d. Horizontal and vertical axis are hydrostatic (β) and shear deformation at the onset of instability (γ_d), respectively.

2.4.2 Elastic stability analysis of single crystals

To relate the deformations to the material yield stress, we consider the behavior of an equivalent continuum hyperelastic material until the onset of instability. We also perform an elastic stability analysis to quantify the difference between the results obtained by the two approaches and to further illustrate the pitfalls of using an elastic stability analysis. For this purpose, a homogenized continuum model of the lattice is considered, as described

in details in chapter 3. We will remind the reader about the main assumptions. Let $\overline{W}$ be the homogenized energy of the continuum under two assumptions: I) The Cauchy-Born hypothesis is satisfied, implying that the underlying lattice will deform under the same deformation gradient as the continuum, II) The strain energy density $\overline{W}(\mathbf{F})$ in the continuum model is equal to the energy of a single unit cell normalized by its volume, obtained from the interatomic potentials [14]. Within this framework, instability occurs following the violation of the strong ellipticity condition [67, 64]:

$$\delta\mathbf{u}^T : \frac{\partial^2\overline{W}(\mathbf{F})}{\partial\mathbf{F}\partial\mathbf{F}} : \delta\mathbf{u} > 0, \tag{2.38}$$

where $\delta\mathbf{u}$ is a perturbation of the displacement field about the deformed configuration.

The continuum body is subjected to exactly the same affine deformation as the lattice. We seek instabilities which result from perturbations having a plane wave basis, i.e. $\delta\mathbf{u} = \delta\mathbf{u}_0 e^{i\boldsymbol{\kappa}\cdot\mathbf{x}}$ [92, 5]. Fig. 2.5 compares the elastic and phonon instability results. We observe that the difference in the results are significant, e.g. 50% for iron at $\beta = -0.03$. Evidently, instabilities that happen at short or finite wavelengths are not captured by an elastic stability analysis. Indeed, since elastic instabilities under affine deformations are a subset of phonon instabilities, the γ_d obtained by phonon calculations either coincide with elastic stability results or predict a smaller value.

At the onset of instability, the Cauchy stress tensor is computed by [93]:

$$\boldsymbol{\sigma} = (\det\mathbf{F})^{-1}\left(\frac{\partial W}{\partial\mathbf{F}}\right)\mathbf{F}^T. \tag{2.39}$$

Fig. 2.6 illustrates the shear stress component, $\tau = \sigma_{12}$ for different hydrostatic pressure values (P), where P$= Tr(\boldsymbol{\sigma})/3$. Evidently, by increasing the hydrostatic pressure (-P), the shear stress at the onset of instability increases. We remark that the large values of stresses are due to lack of imperfections, consistent with the experimental observations that ideal strength of metals are in orders of GPa [86, 94, 95, 96]. These observations motivate the

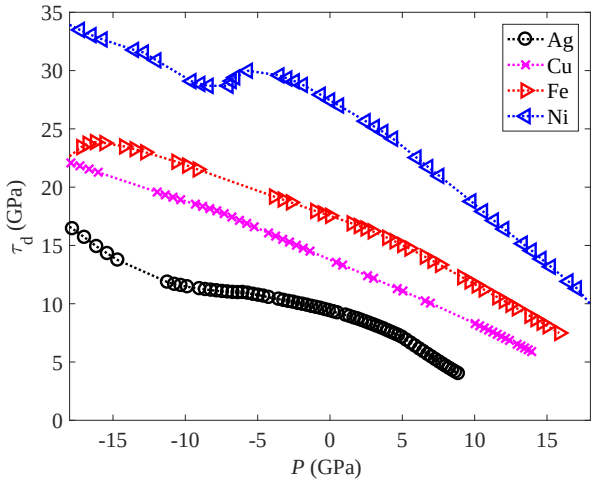

Figure 2.6: Shear normal coupling through Cauchy stress results for the four materials, obtained from phonon stability analysis: Shear vs. hydrostatic pressure. Stress values are in the orders of GPa in the nanoscale perfect single crystals, which is typical in nanoscale experiments [86].

necessity of a pressure-dependent plasticity model for perfect single crystal metals.

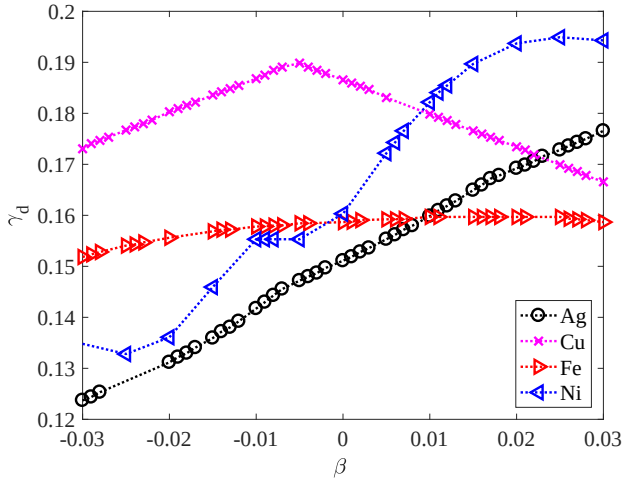

Figure 2.7: Deformation results under combined uniaxial and simple shear deformation $\mathbf{F}'$ for the four different materials, also exhibiting significant shear-normal coupling.

While hydrostatic deformation is chosen to understand non-Schmid effects, applying this type of deformation in the nano-scale experiments might be very challenging. Fig. 2.7 illustrates phonon stability results for deformation $\mathbf{F}'$, i.e. a combined uniaxial deformation and simple shear, which is anticipated to be useful for nano-scale experiments. The point of discontinuity in the slope of this critical shear strain (γ_d) for Copper and Nickel is

associated with the change in the nature of the instability, from finite to long wavelength, with increasing uniaxial strain β.

$$\mathbf{F}' = \begin{bmatrix} 1+\beta & \gamma & 0 \\ 0 & 1 & 0 \\ 0 & 0 & 1 \end{bmatrix}.$$

In summary, we have shown that the onset of plasticity is dominated by a non-Schmid behavior, where a significant dependence of the critical shear deformation γ_d on the hydrostatic deformation β is observed. While certain metals like copper follow the Schmid law relatively well, others such as iron and silver demonstrate a strong non-Schmid behavior. It is verified that depending on the crystal and the loading conditions, short wavelength instabilities are dominant, and cannot be captured by a standard elastic stability analysis. Also, we propose that the widely used Cauchy-Born assumption [97, 98, 6, 3]in single crystals must be appropriately modified after the onset of finite wavelength instabilities [68, 99].

CHAPTER 3
MATERIAL PHASE TRANSISTIONS IN LATTICES: TENSEGRITY METAMATERIALS

3.1 Introduction

[1] The term tensegrity, originally introduced by Fuller [32], refers to a class of structures composed of cables and bars, in an arrangement such that tensile members (cables) belong to a continuous network, while compression members (bars) are either disconnected from each other or belong to isolated compression clusters [33]. Tensegrity structures exhibit strong geometric nonlinearities and are usually designed through form-finding processes [35, 101, 102, 103, 104, 105, 106]. They have been applied to a wide variety of problems, ranging from applications in space [34, 35, 40] and civil [36, 107] structures to modeling biological systems [37, 38, 39], to name a few.

The concept of tensegrity has been recently incorporated into the design of nonlinear metamaterials. In the context of this thesis, we define metamaterials as structural arrangements built at a scale much smaller than that of the application they are intended to, thus exhibiting an effective behavior different than their constituent materials at that large scale [20, 21, 22, 23]. That effective behavior is usually not easily achieved through traditional materials, e.g, metamaterials have been utilized to steer stress waves, generate phononic band-gaps, and to achieve negative effective refraction indices [24, 25, 20, 26, 27, 28]. Typically, tensegrity metamaterials are obtained by performing periodic translations of a tensegrity structure as a fundamental unit cell [108, 29, 31, 109]. Tensegrity metamaterials were initially constructed as one-dimensional lattices, and it was only recently that a tensegrity structure that can tessellate $\mathbb{R}^3$ was proposed [30]. This new development expands the

[1] The results of this chapter is published in [100].

existing application space of tensegrity systems to more realistic three-dimensional cases, and thus we make it the focus of our investigations.

One of the most appealing characteristics of tensegrity metamaterials is that their properties can be tuned and optimized through suitable adjustment in the prestress of the cables [108, 110, 50, 51]. Inspired by the stress induced solid-solid phase transitions in natural materials, we aim to investigate the effects of cable prestressing on the material symmetry phases in tensegrity metamaterials. To that effect, we first apply a homogenization scheme to obtain the effective elasticity tensor of the tensegrity lattice [14], and then examine its eigenspaces through recently developed algebraic methods [52].

Material symmetries, like many other material properties, could also be altered by size effects [111, 112, 61]. Discrepancies between a finte and an infinite periodic system, as far as their rigidity and indeterminacy, has been discussed before [113, 111]. Moreover, symmetry changes solely due to surface effects have previously been reported in particular crystalline materials, where it has been shown that once the surface effects are sufficiently large, they lead to higher material symmetry [60, 61]. Thus, we also investigate possible size effects on the symmetries of tensegrity metamaterials.

The remainder of this chapter is organized as follows. In Section 3.2, we present the theoretical basis for this work, including a discrete model for tensegrity lattices, the periodic boundary condition (PBC) formulation required for modeling an infinite lattice, the homogenization scheme for finding the effective elasticity tensor, and the theory for obtaining the material symmetries. We devote Section 3.3 to the analysis of symmetries and phase transitions in finite and infinite tensegrity metamaterials. Finally, in Section 3.4 we summarize our work and conjecture the existence of similar findings in a more general class of lattices.

3.2 Theory and model description

In this section, we cover the theoretical basis for our investigations. After introducing the unit cell of the tensegrity metamaterial, we describe the procedure for obtaining the equilibrium configuration of finite and infinite tensegrity lattices subject to cable prestress. To this end, we first explain the procedure for constructing a tensegrity unit cell that can tessellate $\mathbb{R}^3$. We then discuss the underlying reduced-order model adopted for modeling the individual elements of the lattice, followed by the development of a constrained optimization formulation for studying the equilibrium of an infinite prestressed lattice. We finally describe a homogenization scheme for obtaining the effective properties of the lattice, as well as the procedure for characterizing its symmetries.

3.2.1 Tensegrity lattice description

There are many different ways of designing a tensegrity structure; in fact form-finding methods are devised and developed with the purpose of constructing new tensegrity systems, for a given nodal connectivity. On the other hand, it was only recently that a 3-dimensional tensegrity lattice design was proposed [30], where we explain the procedure in the following.

Let us consider a truncated octahedron, shown in Fig. 3.1, which consists of 6 square faces, parallel in pairs, with the planes containing each pair being perpendicular to those corresponding to the other two pairs. We label the faces as top, bottom, left, right, back, and front. At first glance, it might seem that because all squares are placed on the faces of a containing cube, this elementary cell could tile $\mathbb{R}^3$, thus generating a 3-dimensional lattice. However, the squares corresponding to each pair have opposite twists with respect to the normal to the plane and they do not coincide when projected on the plane parallel to the faces of the two squares. Thus, if we simply translate the elementary cell, we would end up with an incompatible configuration, as the nodes of the adjacent squares would not

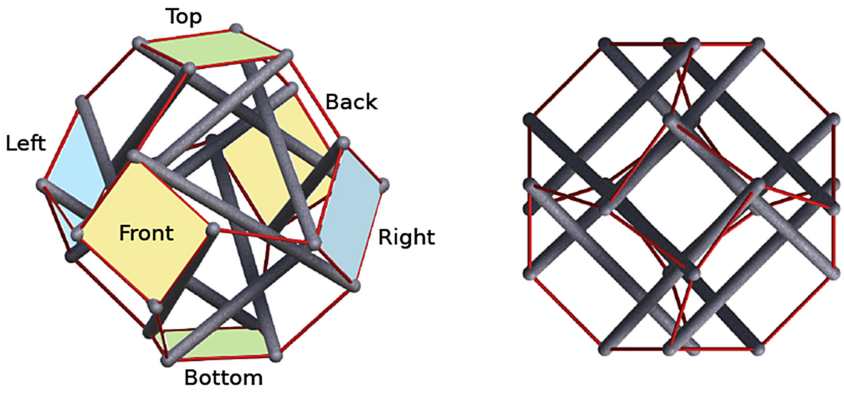

Figure 3.1: Elementary cell for lattice. Perspective (left) and top (right) views with legends indicating naming convention.

overlap.

This incompatibility is illustrated in Fig. 3.3 as follows. Let us consider the bottom-right elementary cell. In the figure, its main axes are aligned with the perspective of the reader in such a way that the top, bottom, left, and right planes remain perpendicular to the viewing plane, whereas the front and back squares are parallel to it. Even though the elementary cell stacked to its left maintains the alignment of the left and right planes, all other planes are rotated with respect to the normal to the coincident face between the cells. The same effect is observed on the elementary cell stacked to the top, with only the top and bottom planes remaining in place. This effect gets worse as we keep stacking cells next to each other. For example, the figure shows that the top-right elementary cell has lost all the alignments with respect to the original cell. Furthermore, due to this misalignment, it would be impossible to insert an elementary cell to connect the bottom-right and top-right cells.

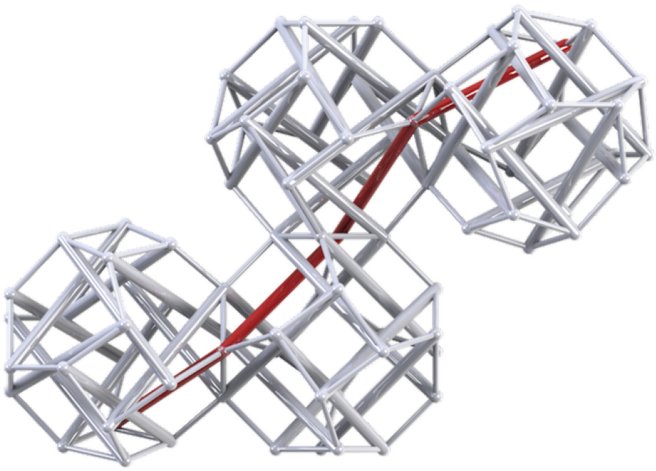

Figure 3.2: Simply stacking of elementary cells leads to continuum compression paths extending throughout the structure.

Additionally, even if somehow we could remove the torsion of the elementary cell, e.g. by selecting cables and bars of varying lengths, another problem remains: for such a configuration, bars would generate continous compression paths that always initiate an external surface of the lattice, then propagate through its interior to finally terminate at another external boundary of the structure. This kind of lattice would fail to comply with the most rigorous definition of tensegrity, as there would not be isolated compression islands within the structure. This, in turn, could negatively affect the stability of the lattice once buckling starts to develop on one of those paths. A continuum compression path is highlighted in red in Fig. 3.3 for purpose of illustration.

In order to address these issues, namely the incompatibility between cells and the presence of continuum compression paths within the structure, a method is proposed [30] to construct a lattice from a macro unit cell consisting of 8 elementary cells related to each other through consecutive reflection operations. The details of such procedure are explained in the following paragraphs.

First, we perform a reflection of the elementary cell (Fig. 3.3, top-left) with respect to the plane containing its right face, obtaining a system of two cells (Fig. 3.3, top-right). The left and right faces of this 2-cell unit now have coincident nodes due to the reflection operation. Consequently, this system can be considered as a building block for one-dimensional

tensegrity lattices, or in structural terms, tensegrity columns. It is worth emphasizing that, as a result of this operation, the top, bottom, front, and back squares of the resulting elementary cells remain aligned to those of the original one.

Subsequently, we proceed to reflect this 2-cell system with respect to the plane containing their top faces, resulting in the 4-cell configuration depicted in Fig. 3.3 (bottom-left). By construction, the left, right, top, and bottom squares of the resulting 4-cell unit have coincident nodes. Consequently, this system can be considered as a building block for 2-dimensional tensegrity lattices, or in structural terms, tensegrity plates. As in the previous step, all squares remain in their original planes, confined to the faces of a rectangular parallelepiped.

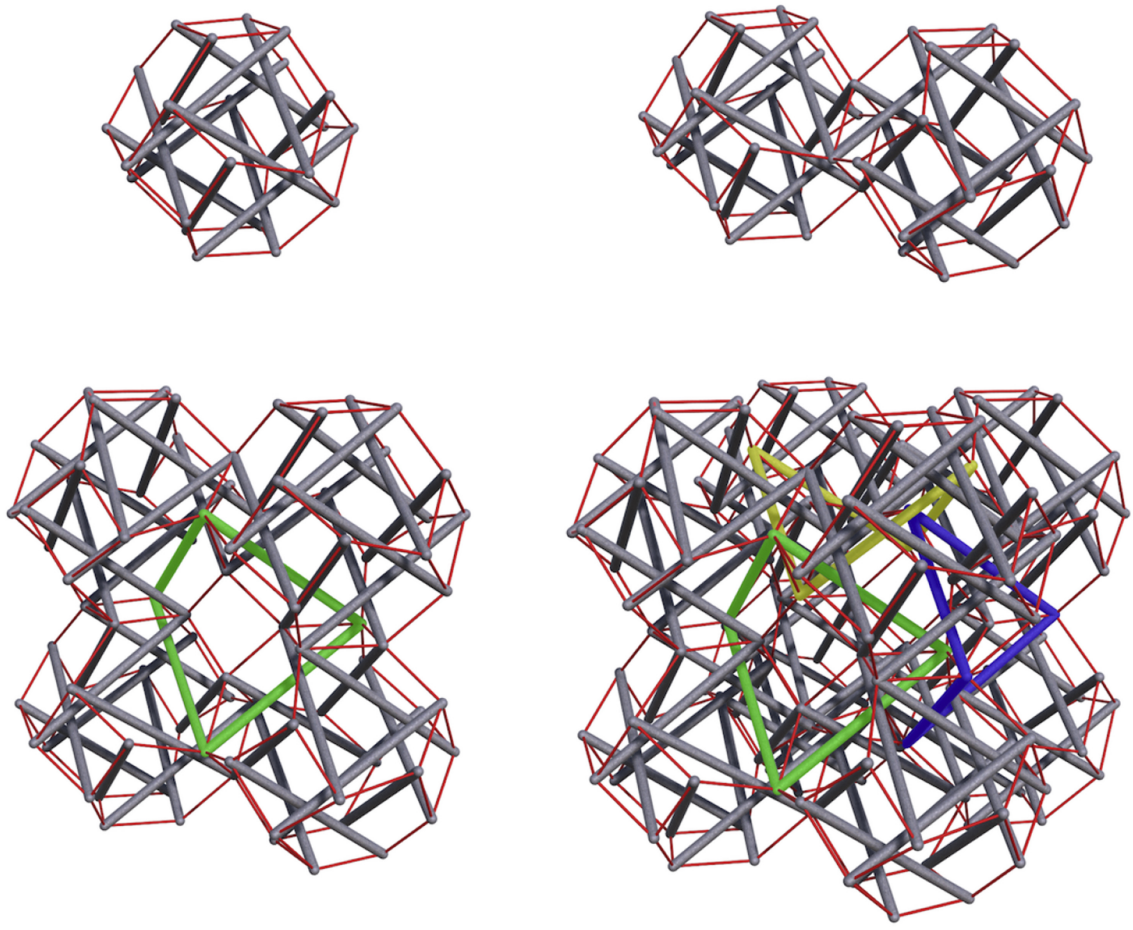

Figure 3.3: Sequence of reflection operations needed to generate a unit cell compatible with translational symmetries.

Finally, the resulting system is reflected with respect to the plane corresponding to their

front faces, obtaining in this way an 8-cell system (Fig. 3.3, bottom-right). By construction, the left, right, top, bottom, front, and back squares of the resulting 8-cell unit have coincident nodes. Consequently, this system can be considered as a building block for 3-dimensional tensegrity lattices, or in structural terms, tensegrity solids. As a result of these reflections, the nodes of the four squares corresponding to the top face coincide with those at the bottom, and the same occurs with the other combinations. Once again, all squares remain in the planes defining a cube, with no associated twist or distortion.

It is worth noting that by following this procedure we not only generate a unit-cell with translational symmetry, but also ensure that there are no continuum compression paths that extend throughout the lattice. By applying successive reflection operations we generate closed compression loops that resemble a folded rhomboid, as depicted by the set of green bars on Fig. 3.3, bottom-left. In Fig. 3.3, bottom-right, we highlight three of these closed-loops in green, yellow, and blue. Each of them has a symmetric counterpart on the opposite side of the cube, totaling 6 closed loops for the unit cell. The bars that do not form closed loops are either isolated from other bars or forming 2-bar v-shape arrangements. All of them become part of closed loops once unit cells are stacked against each other to form a 3-dimensional lattice. In the case of an infinite lattice, every single bar in the structure is part of a closed compression loop, with loops connected to each other exclusively through cables. In this way, our construction recreates the concept of isolated compression islands in a sea of tension, in the spirit of Fuller's definition of tensegrity.

This resultant unit cell, as shown in Figure 3.4, is a $2 \times 2 \times 2$ unit cell, 2 octahedrons in each direction, with space-tilling translational symmetry. The constructed unit cell consists of 96 bars and 240 cables, connected by pin joints, with a total number of nodes N equal to 144.

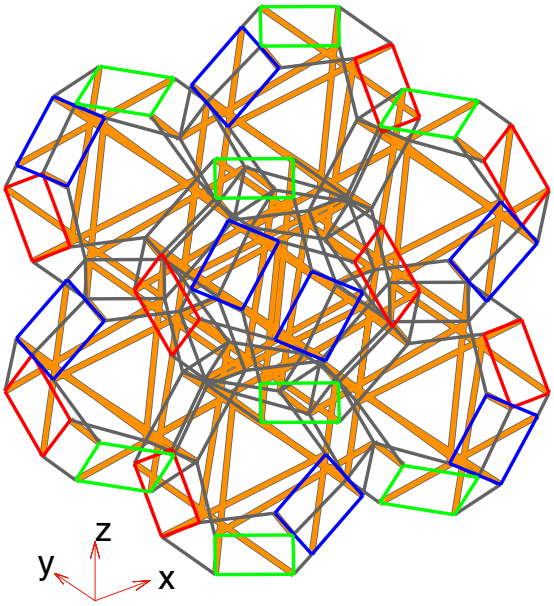

Figure 3.4: Three-dimensional canonical tensegrity unit cell, comprising of 96 bars and 240 cables. Bars are shown in orange. Cables lying in the planes with normals along the X, Y and Z axis are shown in red, blue and green, respectively. All the other cables are shown in grey.

3.2.2 Discrete model

While traditional approaches for modeling the mechanical response of tensegrity structures assume that all components (bars and cables) experience axial loading exclusively [34, 114], a discrete model has been recently proposed to account for their off-axis behavior (bending and shear) as well [115]. The main advantage of this model is that it can capture the buckling and post-buckling behavior of tensegrity-based metamaterials with very few degrees of freedom for each member. We outline the model here for the sake of completeness.

Let us consider a bar of length L and constant cross-section with corresponding area and moment of inertia A and I, respectively. The bar has a homogeneous mass density of ρ and Young's modulus E. We discretize the bar with four masses, three linear springs and two angular springs. Figure 3.5 shows a schematic of the continuum and discretized model.

As depicted in Figure 3.5, there are six parameters in the discrete model: two masses (m_1, m_2), two linear spring stiffness (k_1, k_2), one angular spring stiffness (k_t) and a param-

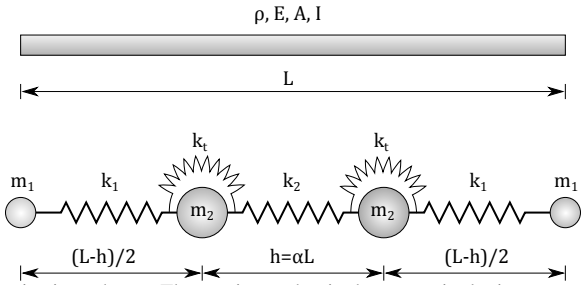

Figure 3.5: Schematic of the discretization scheme. The continuum bar in the tensegrity lattice are replaced by the discrete system.

eter α which determines the unstretched length of the middle spring as a ratio of the total length. We obtain these parameters by enforcing the discrete model to mimic the primary mechanical properties of the continuous bar. First, we require the total mass and the mass moment of inertia of the discrete model to amount to the corresponding values in the bar, which can be expressed as:

$$\begin{aligned} 2m_1 + 2m_2 &= \rho AL, \\ \frac{1}{2}m_1 L^2 + \frac{1}{2}m_2 h^2 &= \frac{1}{12}\rho AL^3. \end{aligned} \tag{3.1}$$

By substituting $h = \alpha L$ with $0 < \alpha < 1$ and solving for m_1 and m_2, one gets the following relations:

$$\begin{aligned} m_1 &= \frac{1}{6}\rho AL\left(\frac{1-3\alpha^2}{1-\alpha^2}\right), \\ m_2 &= \frac{1}{3}\rho AL\left(\frac{1}{1-\alpha^2}\right), \end{aligned} \tag{3.2}$$

We obtain an upper bound for α as $\alpha \leq \sqrt{3}/3$, which is required to have positive masses.

We now enforce equal overall stiffness between the discrete system and the continuum bar. This is attained by specifying the following values for the axial springs:

$$
\begin{aligned}
k_1 &= \frac{2EA}{L(1-\alpha)}, \\
k_2 &= \frac{EA}{\alpha L},
\end{aligned}
\tag{3.3}
$$

We also require the discretized bar to buckle at the same load as the continuum one, which is particularly useful for for problems involving high loads. This is achieved by tuning the value of the angular stiffness k_t. As showing in Fig. 3.6, we assume a symmetric buckling configuration under an applied load P, for which we can write the following for the potential energy:

$$
\Pi = k_1\Big(d_1 - \frac{L-h}{2}\Big)^2 + \frac{k_2}{2}(d_2 - h)^2 + k_t\theta^2 - P\Delta L. \tag{3.4}
$$

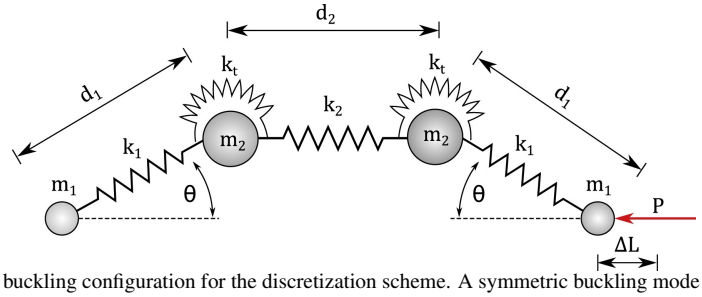

Figure 3.6: Schematics of buckling configuration for the discretization scheme. A symmetric buckling mode is assumed.

Note that ΔL is the displacement induced by the load P and is related to the other kinematic quantites via the equation:

$$
\Delta L = L - 2d_1\cos(\theta) - d_2. \tag{3.5}
$$

We want to minimize the energy, thus we can write the optimality conditions, which results in equilibrium equations, with respect to the generalized coordinates θ, d_1 and d_2:

$$\begin{aligned}
\frac{\partial \Pi}{\partial d_1} &= 2k_1\Big(d_1 - \frac{L-h}{2}\Big) + 2P\cos(\theta) \\
\frac{\partial \Pi}{\partial d_2} &= k_2(d_2 - h) + P \\
\frac{\partial \Pi}{\partial \theta} &= 2k_t\theta - 2Pd_1\sin(\theta)
\end{aligned} \tag{3.6}$$

Using the above equations, after linearizing around $\theta = 0$, we obtain:

$$2k_t\theta - P\theta L + 2P^2\frac{\theta}{k_1} + P\theta h = 0. \tag{3.7}$$

The nontrivial solution of the above equation yields the values of critical load for the discrete system:

$$P_{cr} = \frac{1}{4}k_1(L-h) - \frac{1}{4}\sqrt{k_1^2(L-h)^2 - 16k_1k_t}. \tag{3.8}$$

If we equate the above equation with the Euler's buckling load for a continuum bar, which is $P_{cr} = \pi^2 EI/L$, we obtain the following for k_t:

$$k_t = \frac{1-\alpha}{2}\frac{E\pi^2 I}{AL^3}(AL^2 - I\pi^2). \tag{3.9}$$

Note that the second term in between parentheses can be neglected for slender bars. If t is the characteristic length of the cross section of the bar, then $l \propto t^4$ and $A \propto t^2$. Thus, the second term between parentheses scales as $(t/L)2$ and can be neglected for $t/L \ll 1$, which is usually the case for slender bars. It is worth noting that the resulting expression under this assumption is identical to what we would have obtained if the buckling load of the discrete system was computed neglecting the axial stiffness of the bar, an assumption that is actually made during the derivation of Eulers buckling load for the continuum bar.

Finally the value of α is obtained by enforcing the discrete model to mimic the first two natural frequencies of the continuum bar and its post-buckling behavior. We remark

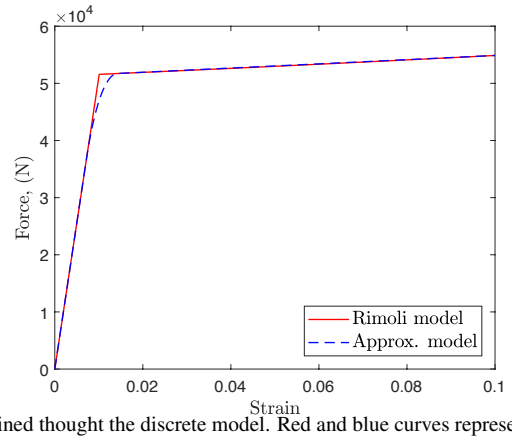

Figure 3.7: Constitutive relation obtained thought the discrete model. Red and blue curves represent the constitutive relation derived from Rimoli's model and the smoothed curve, respectively. Note that to observe the post-buckling transition strains must be compressive (the relation remains linear in the tensile regime.)

here that the cables are modeled with the same discretization model, except that the angular stiffness is set to zero.

We obtain the force-displacement relation for bars by employing the aforementioned model, as shown in Figure 3.7. Note that the transition from a pre-buckling state to a post-buckling state leads to a discontinuity in the derivative of the force-displacement relation. To avoid numerical convergence issues caused by this slope discontinuity, we smooth out the constitutive relation by fitting an arc of a circle near the onset of buckling, such that it is tangent to the lines indicating the pre-buckling and post-buckling regime (see Figure 3.7).

We then write the potential energy of element i (bar or cable) as:

$$E_i = K^i_{\text{effective}}(\Delta l_i)^2, \tag{3.10}$$

where Δl_i is the total change in the length of the i^{th} element and $K_{\text{effective}}$ is the stiffness obtained by the force-displacement relation, as shown in Figure 3.7.

3.2.3 Modeling a finite lattice

When a lattice with pre-stretched cables is assembled, the bars compress and the cables stretch leading to a new equilibrium position for the lattice. The lattice is then said to be under a pre-stretch $\boldsymbol{\lambda}$ (see Section 3.2.7) and the equilibrium configuration is determined by minimizing the energy of a single unit cell with respect to the lattice coordinates subject only to the connectivity constraints. We thus formulate the following minimization problem for any given $\boldsymbol{\lambda} \in \mathbb{R}^6$ –explained in Section 3.2.7– as

$$\min_{\mathbf{x}^{\in}\mathbb{R}^{3N}} W(\mathbf{x}) := \sum_{i=1}^{N_{\text{bar}}+N_{\text{cables}}} E_i, \tag{3.11}$$

where E_i is given by Eq. 3.10. We will discuss in detail how to impose $\boldsymbol{\lambda}$ in Section 3.2.7. The optimality conditions of the aforementioned minimization problem will lead to the equilibrium equations of the associated quasi-static problem. We also add 6 constraints to prevent rigid body motions. Note that while there are many choice for these constraints, one must check they do not impose extra, artificial constraints.

To solve the quasi-static problem we employ a combination of Newton-Raphson and conjugate gradient solvers. We remark here that the conjugate gradient solver is only employed when the stiffness matrix is not full rank. Once the equilibrium configuration is determined, we compute the first elasticity tensor of the homogenized tensegrity lattice. We emphasize that for the case of finite lattices, we do not impose PBC conditions to solve for the equilibrium configuration. In the next section, we present the procedure for obtaining the equilibrium configuration of an infinite lattice by imposing PBC. We employ a homogenization scheme to obtain the effective elasticity tensor of this equilibrium configuration.

3.2.4 Modeling an infinite lattice through PBC

We aim to determine the equilibrium configuration of the lattice under an imposed set of cable pre-stretches by minimizing the energy of a single unit cell under PBC. Since subjecting the cables in the unit cell to an arbitrary pre-stretch can lead to an arbitrary deformed configuration, we do not have a priori knowledge on the direction and magnitude of the basis vectors for the lattice in the equilibrium configuration. This is precisely the main challenge in solving for the equilibrium configuration of the pre-stretched lattice subjected to PBC, which we overcome by formulating the question of determining lattice equilibrium as a constrained minimization problem with the PBC imposed as a constraint.

Let us consider the unit cell shown in Figure 3.4, where it has 96 nodes in the boundaries and 48 nodes in the interior, whose coordinates are denoted respectively by $\mathbf{X}_b$ and $\mathbf{X}_i$. Note that we denote the reference configuration and equilibrium configuration as $\mathbf{X}$ and $\mathbf{x}$ in this section. Let us enclose the unit cell in a cube of length $2L$ and fix a coordinate system with the origin at the center of the cube and x, y and z axis normal to the faces of the cube. Each face of the cube will contain 16 boundary nodes of the unit cell. We label boundary nodes in planes $x = L$, $y = L$ and $z = L$ as the master nodes, $\mathbf{X}_m$, and those in $x = -L$, $y = -L$ and $z = -L$ as slave nodes, $\mathbf{X}_s$. There is a unique slave node for each master node, lying on opposite faces, which implies a one to one correspondence between them. Let $\mathbf{x}_m^p$ and $\mathbf{x}_s^p$ denote the position vector of the master and slave nodes in the deformed prestressed configuration, with the index p running from 1 to N_s, where $N_s = 48$ is the total number of slave nodes. Let $\mathbf{f}_m^p$ and $\mathbf{f}_s^p$ denote, respectively, the forces acting on these nodes. Then PBC in all the n directions, where $n = 3$ in our case and is the number of dimensions, is obtained by imposing restrictions on the displacement and force of these nodes, which may be written as

$$\mathbf{x}_m^p - \mathbf{x}_s^p = \mathbf{a}_l, \quad \mathbf{f}_m^p + \mathbf{f}_s^p = \mathbf{0},\ p \in 1 \text{ to } N_s,\ l \in 1 \text{ to } n. \tag{3.12}$$

Also, we divide the cross-section area of the cables that lie in the faces of the cube by two, since those cables are shared by two adjacent cells. As mentioned before, the lattice vectors $\mathbf{a}_l$ change due to imposed pre-stretches and they are not known a priori. Hence, we impose the following conditions for the displacements:

$$\begin{aligned} &\mathbf{x}_m^p - \mathbf{x}_s^p = \mathbf{x}_m^\alpha - \mathbf{x}_s^\alpha,\ p \in 1 \text{ to } N_s \\ &\mathbf{R} = x_m^{\beta,i} - x_s^{\beta,i} = 0,\ i \in 1 \text{ to } n \\ &\mathbf{x}_m^1 = \mathbf{X}_m^1. \end{aligned} \tag{3.13}$$

$\mathbf{x}_m^\alpha$ and $\mathbf{x}_s^\alpha$ are the coordinates of n pairs of master and slave nodes, one in each direction, where the index α depends on the index p (i.e. $\alpha(p)$) and is chosen as $\alpha = 1$ for $1 \leq p \leq 16$, $\alpha = 17$ for $17 \leq p \leq 32$ and $\alpha = 33$ for $33 \leq p \leq 48$. Note that the choice of $\mathbf{x}^\alpha$ is not unique and one can choose any pair of master and slave nodes in each direction. $\mathbf{R}$ is a set of C_r equations that constrains the rigid body rotations, where $C_r = 3$ is the number of equations. Each equation in $\mathbf{R}$ has a corresponding β, which is an index -between 1 and 48- associated to a pair of master and slave nodes, and i as a component of the position vector of the chosen pair. While the choice of $x^{\beta,i}$ is not unique, it is not arbitrary, since it might lead to physically incorrect constraints, such as artificial dilation, if improperly chosen. For example, for a given β, if we choose i along the normal direction of the parallel planes that master and slave nodes lie in, imposing $\mathbf{R}$ will identify both the nodes, which is obviously incorrect. In this work, we choose the pairs of (β, i) as $(1, 1)$, $(17, 2)$ and $(33, 3)$. The last condition, which fixes the position of an arbitrary master node, constrains rigid body translations. In total we have $n \times (N_s - n + 1) + C_r$ conditions in (3.13).

We determine the equilibrium configuration by formulating a constrained optimization problem to minimize the unit cell energy subject to the conditions listed in equations (3.13) . We introduce Lagrange multipliers, $\boldsymbol{\mu}^d = \{\boldsymbol{\mu}_p^d\}_{p=1}^{N_s-n}$, $\boldsymbol{\mu}^f = \{\boldsymbol{\mu}_p^f\}_{p=1}^{N_s}$ and $\boldsymbol{\mu}^r = \{\mu_p\}_{p=1}^{C_r}$ corresponding, respectively, to the displacement, force and rigid body rotations constraints. Note that for every p, $\boldsymbol{\mu}_p^d$ and $\boldsymbol{\mu}_p^f$ are vectors in $\mathbb{R}^3$. Thus we construct the constraint optimization problem as

$$\min_{\mathbf{x}\in\mathbb{R}^{3N}} \max_{\substack{\boldsymbol{\mu}^d\in\mathbb{R}^{3(N_s-n)} \\ \boldsymbol{\mu}^f\in\mathbb{R}^{3N_s} \\ \boldsymbol{\mu}^r\in\mathbb{R}^{C_r}}} L := \tilde{W} + \sum_{\substack{p=1, \\ p\neq\alpha}}^{N_s} \boldsymbol{\mu}_p^d(\mathbf{x}_m^p - \mathbf{x}_s^p - \mathbf{x}_m^\alpha + \mathbf{x}_s^\alpha) + \sum_{p=1}^{N_s} \boldsymbol{\mu}_p^f \left(\frac{\partial \tilde{W}}{\partial \mathbf{x}_m^p} + \frac{\partial \tilde{W}}{\partial \mathbf{x}_s^p} \right) + \sum_{q=1}^{C_r} \mu_q^r R^q, \tag{3.14}$$

where L and $\tilde{W}$ are respectively the Lagrangian and the energy of a unit cell. $\boldsymbol{\mu}^d$, $\boldsymbol{\mu}^f$, $\boldsymbol{\mu}^r$ are vectors of Lagrange multipliers associated with the periodic boundary condition constraints. We emphasize that $\tilde{W} \neq W$, since we are dividing the cross-sectional area of cables in the boundaries of the unit cell by two, as mentioned before, in the PBC formulation. The optimality conditions give the following equations:

$$\frac{\partial L}{\partial \mathbf{x}^i} = \frac{\partial \tilde{W}}{\partial \mathbf{x}^i} + \boldsymbol{\mu}_p^d(\delta_{i(p,m)} - \delta_{i(p,s)} - \delta_{i(\alpha,m)} + \delta_{i(\alpha,s)}) + \tag{3.15a}$$

$$\sum_{p=1}^{3\times 48} \boldsymbol{\mu}_p^f \left(\frac{\partial^2 \tilde{W}}{\partial x^i \partial x_m^p} + \frac{\partial^2 \tilde{W}}{\partial x^i \partial x_s^p} \right) + \sum_{q=1}^{3} \mu_q^r \frac{\partial R^q}{\partial x^i} = \mathbf{0}, \tag{3.15b}$$

$$\frac{\partial L}{\partial \boldsymbol{\mu}_{p\prime}^d} = (\mathbf{x}_m^{p\prime} - \mathbf{x}_s^{p\prime} - \mathbf{x}_m^\alpha + \mathbf{x}_s^\alpha) = \mathbf{0}, \tag{3.15c}$$

$$\frac{\partial L}{\partial \boldsymbol{\mu}_p^f} = (\frac{\partial \tilde{W}}{\partial \mathbf{x}_m^p} + \frac{\partial \tilde{W}}{\partial \mathbf{x}_s^p}) = \mathbf{0}, \tag{3.15d}$$

$$\frac{\partial L}{\partial \mu_q^r} = R^q = 0. \tag{3.15e}$$

We remark here that $\delta_{i(p,m)}$ is one if i is equal to the index of the master node in master-slave pair p, and zero otherwise. We solve the system (3.15) by using a Newton-Raphson

solver. In incremental form, the matrices have the following expressions:

$$\begin{pmatrix} \mathbf{K}+\mathbf{T} & \mathbf{B} & \mathbf{K}_m+\mathbf{K}_s & \mathbf{D} \\ \mathbf{B}^T & \mathbf{0} & \mathbf{0} & \mathbf{0} \\ \mathbf{K}_m^T+\mathbf{K}_s^T & \mathbf{0} & \mathbf{0} & \mathbf{0} \\ \mathbf{D}^T & \mathbf{0} & \mathbf{0} & \mathbf{0} \end{pmatrix} \begin{pmatrix} \delta\mathbf{x} \\ \delta\boldsymbol{\mu}^d \\ \delta\boldsymbol{\mu}^f \\ \delta\boldsymbol{\mu}^r \end{pmatrix} + \nabla L = \mathbf{0}. \tag{3.16}$$

Here ∇L denotes the residual in the system (3.15), $\mathbf{K}$ denotes the stiffness matrix, $\mathbf{K}$ with subscripts denote the rows corresponding to the master/slave nodes arising from the linearization of Eqn. (3.15d), $\mathbf{D}$ is a matrix composed of the rigid body rotation constraints and $\mathbf{B}$ is also matrix with components $\{0, -1, 1\}$, arising from taking the derivative of Eqn. (3.15c) with respect to $\mathbf{x}_i$. Also, $\mathbf{T}$ is obtained as follows:

$$\mathbf{T} = \sum_{p=1}^{48} \boldsymbol{\mu}_p^f \left(\frac{\partial^3 \tilde{W}}{\partial \mathbf{x}^j \partial \mathbf{x}^i \partial \mathbf{x}_m^p} + \frac{\partial^3 \tilde{W}}{\partial \mathbf{x}^j \partial \mathbf{x}^i \partial \mathbf{x}_s^p} \right), \tag{3.17}$$

where the derivatives are provided in the appendix (see D). Once we obtain the equilibrium configuration under PBC, we will homogenize the lattice to compute the effective elasticity tensor.

3.2.5 Effective elasticity tensor

Obtaining the symmetries of the tensegrity lattice through the $3N \times 3N$-dimensional stiffness matrix of the unit cell using analytical approaches is next to impossible, if not so. This is due to the high dimensionality of the eigenspace of the stiffness matrix. Therefore, we seek for a homogenized continuum model, which allows us to compute the equivalent elasticity tensor. It also allows us to use an analytical group theory based approach, which examines the homogenized elasticity tensor to find the symmetries of the lattice.

A first order homogenized continuum model for discrete systems, applicable as well to tensegrity lattices has been developed previously by the co-authors [30, 14]. We employ a

similar approach here. Since we are homogenizing the interior of a large lattice as a point in a continuum, we impose PBC on the unit cell (3.12). Note that, unlike in the previous subsection, we know the lattice vectors ($\mathbf{a}_l$) in this stage, which is a direct consequence of subjecting the lattice to an affine deformation field during the homogenization step.

Let us remark here that the pre-stretched configuration is taken to be the reference configuration ($\mathbf{F} = \mathbf{I}$) and we do not subject the lattice to any additional deformation to compute the homogenized first elasticity tensor $\mathbf{C}$. Although the procedure presented below for obtaining $\mathbf{C}$ is applicable when the lattice is subjected to any affine deformation, we are only concerned with $\mathbf{C}$ at the reference configuration for the purpose of obtaining the material symmetry.

Let us now assume that the strain energy of a single unit cell ($\tilde{W}$) normalized by its volume located in the interior of a very large lattice with its boundary subjected to an affine displacement field characterized by a constant deformation gradient $\mathbf{F}$, is equivalent to the strain energy density W of a hyper-elastic continuum. By definition, then, W is solely a function of $\mathbf{F}$:

$$W(\mathbf{F}) = \tilde{W}(\mathbf{x}, \mathbf{F}), \tag{3.18}$$

where $\mathbf{x}$ is a $3N$-dimensional vector containing the position vectors of all the N nodes in a unit cell in the deformed configuration. We remark here that the equivalence in energy in (3.18) holds for the limit of the strain energy density as the volume of the lattice tends to infinity [68]. Note that $\mathbf{x} = \{\mathbf{x}_i, \mathbf{x}_m, \mathbf{x}_s\}$ and $\mathbf{x}_s$ is related to $\mathbf{x}_m$ and initial configuration as $\mathbf{x}_s = \mathbf{x}_m + \mathbf{F}(\mathbf{X}_s - \mathbf{X}_m)$. Thus we can write $\tilde{W}(\mathbf{x}, \mathbf{F}) = \overline{W}(\mathbf{x}_u, \mathbf{F})$, where $\mathbf{x}_u$ is the union of $\mathbf{x}_i$ and $\mathbf{x}_m$. Let us remark that in a complex lattice like ours, due to internal degrees of freedom, $\mathbf{x}_u$ are not known a priori. We obtain $\mathbf{x}_u$ by solving for the equilibrium of a single unit cell with boundary nodes subjected to an affine deformation field characterized by a constant deformation gradient $\mathbf{F}$[67].

The first elasticity tensor is defined as $\mathbb{C} = \partial^2 W / \partial \mathbf{F} \partial \mathbf{F}$, which is computed as:

$$\mathbb{C} = \frac{\partial^2 \overline{W}}{\partial \mathbf{F} \partial \mathbf{F}} + \frac{\partial^2 \overline{W}}{\partial \mathbf{F} \partial \mathbf{x}_u} \frac{\partial \mathbf{x}_u}{\partial \mathbf{F}}. \tag{3.19}$$

Note that (3.19) is obtained by assuming equilibrium. Using the equilibrium of the unit cell, we can write the following:

$$\begin{aligned} &\frac{\partial \overline{W}}{\partial \mathbf{x}_u} = 0 \implies \frac{d}{d\mathbf{F}} \left(\frac{\partial \overline{W}}{\partial \mathbf{x}_u} \right) = 0, \\ &\frac{d}{d\mathbf{F}} \left(\frac{\partial \overline{W}}{\partial \mathbf{x}_u} \right) = \frac{\partial^2 \overline{W}}{\partial \mathbf{x}_u \partial \mathbf{F}} + \frac{\partial^2 \overline{W}}{\partial \mathbf{x}_u \partial \mathbf{x}_u} \frac{\partial \mathbf{x}_u}{\partial \mathbf{F}} = 0. \end{aligned} \tag{3.20}$$

We obtain $\frac{\partial \mathbf{x}_u}{\partial \mathbf{F}}$ from (3.20) and plug it in (3.19), which leads to:

$$\mathbb{C} = \frac{\partial^2 \overline{W}}{\partial \mathbf{F} \partial \mathbf{F}} - \frac{\partial^2 \overline{W}}{\partial \mathbf{F} \partial \mathbf{x}_u} \left(\frac{\partial^2 \overline{W}}{\partial \mathbf{x}_u \partial \mathbf{x}_u} \right)^{-1} \frac{\partial^2 \overline{W}}{\partial \mathbf{x}_u \partial \mathbf{F}}. \tag{3.21}$$

We compute the derivatives of $\overline{W}$ in (3.21) with respect to $\mathbf{F}$ as follows:

$$\begin{aligned} \frac{\partial^2 \overline{W}}{\partial F_{ij} \partial F_{kl}} &= \sum_{r=1}^{N_s} \sum_{p=1}^{N_s} \frac{\partial^2 \overline{W}}{\partial x_s^{r,i} \partial x_s^{p,k}} (X_s^{r,j} - X_m^{r,j})(X_s^{p,l} - X_m^{p,l}), \\ \frac{\partial^2 \overline{W}}{\partial x_u^k \partial F_{ij}} &= \sum_{r=1}^{N_s} \frac{\partial^2 \overline{W}}{\partial x_u^k \partial x_s^{r,i}} (X_s^{r,j} - X_m^{r,j}), \\ \frac{\partial^2 \overline{W}}{\partial \mathbf{F} \partial \mathbf{x}_u} &= \left(\frac{\partial^2 \overline{W}}{\partial \mathbf{x}_u \partial \mathbf{F}} \right)^T, \end{aligned} \tag{3.22}$$

where $i, j, k, l \in \{1, 2, 3\}$ and N_s is the number of slave nodes. Note that $\overline{W}$ is assumed to be at least twice differentiable, which is certainly true in our case. We also note that the derivatives in the above expressions are evaluated at $\mathbf{F} = \mathbf{I}$.

3.2.6 Material symmetry

Material symmetries of the homogenized model are investigated by exploring the symmetries of the effective elasticity tensor $\mathbb{C}$, obtained through the procedure discussed in the

previous subsection. Note by considering the major and minor symmetries of the fourth order tensor $\mathbb{C}$, it can also be represented as a map $[\mathbb{C}] : L_{2,s}(\mathbb{R}^3) \rightarrow L_{2,s}(\mathbb{R}^3)$ from the space of symmetric rank-2 tensors to itself, where

$$[\mathbb{C}](\boldsymbol{\epsilon}) = \boldsymbol{\sigma}, \tag{3.23}$$

$\boldsymbol{\epsilon}$ is the symmetric part of the displacement gradient $\nabla \mathbf{u} = \partial \mathbf{u}/\partial \mathbf{X}$. Note that $L^2_{2,s}$ is a six-dimensional space. An orthonormal basis for $L_{2,s}$, $\mathbf{E}$, is constructed using an orthonormal basis, $\mathbf{e} = \{\mathbf{e}_1, \mathbf{e}_2, \mathbf{e}_3\}$, for $\mathbb{R}^3$ [53, 54, 55, 52]:

$$E_{\alpha(i,j)}(\mathbf{e}) = 2^{-\frac{1}{2-\delta_{ij}}}(\mathbf{e}_i \otimes \mathbf{e}_j + \mathbf{e}_j \otimes \mathbf{e}_i), \tag{3.24}$$

where $\alpha(i,j) = i\delta_{ij} + (1-\delta_{ij})(9-i-j)$. Note that α varies from 1 to 6. The elasticity tensor can be represented in the new basis (3.24) as follows:

$$[\mathbb{C}] = \begin{pmatrix} c_{11} & c_{12} & c_{13} & \sqrt{2}c_{14} & \sqrt{2}c_{15} & \sqrt{2}c_{16} \\ c_{12} & c_{22} & c_{23} & \sqrt{2}c_{24} & \sqrt{2}c_{25} & \sqrt{2}c_{26} \\ c_{13} & c_{23} & c_{33} & \sqrt{2}c_{34} & \sqrt{2}c_{35} & \sqrt{2}c_{36} \\ \sqrt{2}c_{14} & \sqrt{2}c_{24} & \sqrt{2}c_{34} & 2c_{44} & 2c_{45} & 2c_{46} \\ \sqrt{2}c_{15} & \sqrt{2}c_{25} & \sqrt{2}c_{35} & 2c_{45} & 2c_{55} & 2c_{56} \\ \sqrt{2}c_{16} & \sqrt{2}c_{26} & \sqrt{2}c_{36} & 2c_{46} & 2c_{56} & 2c_{66} \end{pmatrix}.$$

An elasticity tensor $[\mathbb{C}]$ has symmetry $\mathbf{A}$, where $\mathbf{A} \in SO(3)$ is a rotation matrix, if and only if:

$$\begin{aligned} &\mathbf{A}[\mathbb{C}](\boldsymbol{\epsilon}) = [\mathbb{C}](\boldsymbol{\epsilon}), \\ &\mathbf{A}[\mathbb{C}](\boldsymbol{\epsilon}) := \mathbf{A}[\mathbb{C}](\mathbf{A}^t \boldsymbol{\epsilon} \mathbf{A})\mathbf{A}^t, \ \forall \ \boldsymbol{\epsilon} \in L_{2,s}. \end{aligned} \tag{3.25}$$

An elasticity tensor can exhibit eight symmetries and the direct sum of all the corresponding

spaces of each eigentensor will form the whole $L_{2,s}$ space [116, 117]. Bóna. *et. al.* [52] proved necessary and sufficient conditions that an elasticity tensor needs to satisfy to fall in any of the eight symmetry classes (see section 3.2.6). The main idea lies in finding elements of the $SO(3)$, special orthogonal rotation group, that will maintain the eigen decomposition of c. The main advantage of this method is that it consists of coordinate-free conditions and does not require an a priori knowledge of the symmetry axes.

For the sake of completeness, we briefly review the essential theorems proved by Bóna. *et. al.* [52] to obtain the symmetries of the elasticity tensor. The framework is built on the following theorem, stated by Rychlewski [118]:

Theorem for symmetries of elasticity tensor. Let $[\mathbb{C}]$ be an elasticity tensor with each eigenvalue $\lambda \in \mathbb{R}$ and the corresponding space of eigentensor $\Lambda_\lambda \in L^2_{2,s}(\mathbb{R}^3)$, where $L^2_{2,s}(\mathbb{R}^3)$ is the space of symmetric rank-2 tensors. Then, the symmetry group of $\mathbb{C}$ consists of all the symmetric operators $A \in SO(3)$ that preserve the Λ_λ for all the eigenvalues. In other words, if we consider a direct decomposition of $L^2_{2,s}(\mathbb{R}^3)$, determined by eigendecomosition of $\mathbb{C}$ as

$$L^2_{2,s}(\mathbb{R}^3) = \oplus_\lambda \Lambda_\lambda, \tag{3.26}$$

the symmetry group of $\mathbb{C}$ coincides with the subgroup of $SO(3)$ that preserves the eigendecomposition (3.26), namely

$$G_c = \cap_\lambda \{A \in SO(3) | A\Lambda_\lambda A^t = \Lambda_\lambda\}. \tag{3.27}$$

We next explain the geometric meaning of the symmetries that are of interest for our purposes, as well as the necessary and sufficient theorems for obtaining each symmetry. We note that for a given $mathbbC$, we denote eigenvalue 'i' by λ_i, its multiplicity by m_i and the corresponding space of eigentensor by Λ_i. We also denote the elements in Λ_i by $\sigma \in L^2_{2,s}(\mathtt{R}^3)$.

Cubic symmetry

An elasticity tensor, $\mathbb{C}$, has cubic symmetry if it is invariant under rotations by $\pi/2$ around two mutually orthogonal axes. Thus, a basis with e_1 and e_2 parallel to the two orthogonal axes, is a natural basis of $\mathbb{C}$. In the context of our definition in the previous subsection,

$$G_c = \{A \in SO(3), A(e_i) = \pm e_j : i, j \in \{1, 2, 3\}\}. \tag{3.28}$$

The matrix representation of a cubic elasticity tensor, with respect to its natural basis is

$$[\mathbb{C}] = \begin{pmatrix} c_{11} & c_{12} & c_{12} & 0 & 0 & 0 \\ c_{12} & c_{11} & c_{12} & 0 & 0 & 0 \\ c_{12} & c_{12} & c_{11} & 0 & 0 & 0 \\ 0 & 0 & 0 & 2c_{44} & 0 & 0 \\ 0 & 0 & 0 & 0 & 2c_{44} & 0 \\ 0 & 0 & 0 & 0 & 0 & 2c_{44} \end{pmatrix}.$$

In this case, $\mathbb{C}$ has the following eigenvalues with corresponding multiplicities, $\lambda_1 = c_{11} + 2c_{12}$ with $m_1 = 1$, $\lambda_2 = c_{11} - c_{12}$ with $m_2 = 2$ and $\lambda_3 = 2c_{44}$ with $m_3 = 3$. Also, the corresponding spaces of eigentensors are expressed as -with respect to the natural basis-

$$\begin{aligned} \Lambda_1 &= \{a_1 I, a_1 \mathbb{R}\} = \{a_1(E_1 + E_2 + E_3); a_1 \in \mathbb{R}\}, \\ \Lambda_2 &= \{a_2(E_1 - E_3) + a_3(E_2 - E_3); a_2, a_3 \in \mathbb{R}\}, \\ \Lambda_3 &= \{a_4 E_4 + a_5 E_5 + a_6 E_6; a_4, a_5, a_6 \in \mathbb{R}\}. \end{aligned} \tag{3.29}$$

If the followin theorem is satisfied, $\mathbb{C}$ has cubic symmetry.

Criteria for cubic symmetry.

I) $[\mathbb{C}]$ has three distinct eigenvalues λ_1 , λ_2 and λ_3 with $m_1 = 1$, $m_2 = 2$ and $m_3 = 3$.

II) All σ in Λ_1 have eigenvalues with multiplicity three.

III) All σ in Λ_2 have three common eigenvectors.

One can easily compute the three independent coefficients of a cubic elasticity tensor, based on their eigenvalues as follows:

$$c_{11} = \frac{\lambda_1 + 2\lambda_2}{3},\ c_{12} = \frac{\lambda_1 - \lambda_2}{3},\ c_{12} = \frac{\lambda_3}{2} \tag{3.30}$$

Tetragonal symmetry

An elasticity tensor, $\mathbb{C}$, has tetragonal symmetry if it is invariant under a four-fold rotation. Let us assume e_3 is parallel to the axis of rotation,then there exists an orthonormal basis $\{e_1, e_2, e_3\}$ as the natural basis of $\mathbb{C}$, with respect to which the symmetry group is

$$G_c = \{I, R_{\pm\pi/2,e_3}, R_{\pi,e_3}, -R_{u_a}; a \in \{1,2,3,4\}\}, \tag{3.31}$$

where R_{u_a}, $a \in \{1,2,3,4\}$, are reflections about four planes that contain e_3, the angle between any two planes is either $\pi/4$ or $\pi/2$.

The matrix representation of $\mathbb{C}$ with respect to its natural basis is

$$[\mathbb{C}] = \begin{pmatrix} c_{11} & c_{12} & c_{13} & 0 & 0 & 0 \\ c_{12} & c_{11} & c_{13} & 0 & 0 & 0 \\ c_{13} & c_{13} & c_{33} & 0 & 0 & 0 \\ 0 & 0 & 0 & 2c_{44} & 0 & 0 \\ 0 & 0 & 0 & 0 & 2c_{44} & 0 \\ 0 & 0 & 0 & 0 & 0 & 2c_{66} \end{pmatrix}.$$

The elasticity tensor has five eigenvalues:

$$\begin{aligned}
\lambda_1 &= \frac{c_{11}+c_{12}+c_{33}+\sqrt{(c_{11}+c_{12}-c_{33})^2+8c_{13}^2}}{2},\\
\lambda_2 &= \frac{c_{11}+c_{12}+c_{33}-\sqrt{(c_{11}+c_{12}-c_{33})^2+8c_{13}^2}}{2},\\
\lambda_3 &= c_{11}-c_{12},\\
\lambda_4 &= 2c_{66},\\
\lambda_5 &= 2c_{44},
\end{aligned} \tag{3.32}$$

wutg the corresponding multiplicities as $m_1 = m_2 = m_3 = m_4 = 1$ and $m_5 = 2$. Let us define γ_1 as

$$\gamma_1 = -\frac{c_{11}+c_{12}-c_{33}+\sqrt{(c_{11}+c_{12}-c_{33})^2+8c_{13}^2}}{2c_{13}}. \tag{3.33}$$

Then we can define the corresponding five spaces of eigentensorsm with respect to the natural basis, as

$$\begin{aligned}
\Lambda_1 &= \{a_1(E_1+E_2+\gamma_1 E_3); a_1 \in \mathbb{R}\},\\
\Lambda_2 &= \{a_2(\gamma_1(E_1+E_2)-2E_3); a_2 \in \mathbb{R}\},\\
\Lambda_3 &= \{a_3(E_1-E_2); a_3 \in \mathbb{R}\},\\
\Lambda_4 &= \{a_4 E_6; a_4 \in \mathbb{R}\},\\
\Lambda_5 &= \{a_5 E_4 + a_6; a_5, a_6 \in \mathbb{R}\}.
\end{aligned} \tag{3.34}$$

For a given $\mathbb{C}$, if the following necessary and sufficient conditions are satisfied, tetragonal material symmetry is obtained.

Criteria for tetragonal symmetry.

I) $[\mathbb{C}]$ has five distinct eigenvalues λ_i (i = 1 to 5), where $m_1 = m_2 = m_3 = m_4 = 1$ and $m_5 = 2$.

II) All σ in Λ_1 and Λ_2 have two distinct eigenvalues and a common one-dimensional eigenspace.

III) All σ in Λ_3 and Λ_4 have a common zero eigenvalues with corresponding eigenspace common with the one-dimensional eigenspace of Λ_1 and Λ_2.
IV) All σ in Λ_3 have three distinct eigenvalues where corresponding eigenvectors are also eigenvectors of σ in Λ_1.

Having six invariants for a tetragonal elasticity tensor -$\lambda_1, \lambda_2, \lambda_3, \lambda_4, \lambda_5, \gamma_1$-, we can obtain the six coefficients of a tetragonal tensor, with respect to its natural basis, as

$$\begin{aligned} c_{11} &= \frac{2(\lambda_2+\lambda_3)+(\lambda_1+\lambda_3)\gamma_1^2}{2(2+\gamma_1^2)},\ c_{12} = \frac{2(\lambda_2-\lambda_3)+(\lambda_1-\lambda_3)\gamma_1^2}{2(2+\gamma_1^2)} \\ c_{13} &= \frac{(\lambda_2-\lambda_1)\gamma_1}{2+\gamma_1^2},\ c_{33} = \frac{2\lambda_1+\lambda_2\gamma_1^2}{2+\gamma_1^2},\ c_{44} = \frac{\lambda_4}{2},\ c_{66} = \frac{\lambda_5}{2}. \end{aligned} \tag{3.35}$$

Orthotropic symmetry

An elasticity tensor, $\mathbb{C}$, has orthotropic symmetry it is invariant under two rotations by π around two mutually orthogonal axes. If e_1 and e_2 are parallel to the two axes of rotation, with respect to an orthonormal basis $\{e_1, e_2, e_3\}$, which is a natural basis for $\mathbb{C}$, the symmetry group is

$$G_c = \{I, R_{\pi,e_i}; i \in \{1,2,3\}\}. \tag{3.36}$$

The matrix representation of an orthotropic elasticity tensor, in its natural basis, is

$$[\mathbb{C}] = \begin{pmatrix} c_{11} & c_{12} & c_{13} & 0 & 0 & 0 \\ c_{12} & c_{22} & c_{23} & 0 & 0 & 0 \\ c_{13} & c_{23} & c_{33} & 0 & 0 & 0 \\ 0 & 0 & 0 & 2c_{44} & 0 & 0 \\ 0 & 0 & 0 & 0 & 2c_{55} & 0 \\ 0 & 0 & 0 & 0 & 0 & 2c_{66} \end{pmatrix}.$$

The above tensor has six distinct eigenvalues; first three, $\lambda_i, i \in \{1,2,3\}$, are the eigenvalues of the upper-left 3×3 block of the above matrix, and the other three are $\lambda_4 = 2c_{44}$, $\lambda_5 = 2c_{55}$, $\lambda_6 = 2c_{66}$. We also consider the following three parameters

$$\gamma_1 = \frac{a_1}{c_1},\ \gamma_2 = \frac{b_1}{c_1},\ , \gamma_3 = \frac{a_2}{b_2}. \tag{3.37}$$

Let us also define

$$\begin{aligned} x_1 &= -\gamma_1\gamma_3 - \gamma_2, \\ x_2 &= -\frac{\gamma_2\gamma_3 - \gamma_1}{1 + \gamma_2^2 + \gamma_1\gamma_2\gamma_3} \\ x_3 &= \frac{\gamma_2\gamma_3 - \gamma_1}{1 + \gamma_2^2 + \gamma_1\gamma_2\gamma_3}. \end{aligned} \tag{3.38}$$

The corresponding six spaces of of eigentensors are expressed, with respect to the natural basis is

$$\begin{aligned} \Lambda_1 &= \{a_1(\gamma_1 E_1 + \gamma_2 E_2 + E_3); a_1 \in \mathbb{R}\}, \\ \Lambda_2 &= \{a_2(\gamma_3 E_1 + E_2 + x_1 E_3); a_2 \in \mathbb{R}\}, \\ \Lambda_3 &= \{a_3(E_1 + x_2 E_2 + x_3 E_3); a_3 \in \mathbb{R}\}, \\ \Lambda_4 &= \{a_4 E_4; a_4 \in \mathbb{R}\}, \\ \Lambda_5 &= \{a_5 E_5; a_5 \in \mathbb{R}\}, \\ \Lambda_6 &= \{a_6 E_6; a_6 \in \mathbb{R}\}. \end{aligned} \tag{3.39}$$

We note that x_1, x_2 and x_3 are chosen in such a way that the first three eigenspaces are mutually orthogonal. We next present the theorem, for determining whether a given elasticity tensor has orthotropic symmetry.

Criteria for orthotropic symmetry.

I) $[\mathbb{C}]$ has six distinct eigenvalues λ_i ($i = 1$ to 5), each with multiplicity one.

II) All σ in Λ_1, Λ_2 and Λ_3 have distinct eigenvalues.

III) All σ in Λ_1, Λ_2 and Λ_3 have three common eigenvectors e_1, e_2 and e_3.

IV) All σ in Λ_4, Λ_5 and Λ_6 have a common zero eigenvalue, with the corresponding eigenvector for each Λ_{i+3} is e_i, for $i = 1, 2, 3$.

In a similar fashion, the components of an orthotropic elasticity tensor are determined from the nine invariants, that is λ_1 to λ_6 and γ_1 to γ_3.

3.2.7 Symmetry phases of a pre-stretched tensegrity lattice

Let us define the cable pre-stretch λ as the ratio between the undeformed length of the cable and the distance between two nodes connecting a cable in the canonical unit cell (Figure 3.4). For instance, $\lambda = 0.99$ means that the undeformed cable is 1 % shorter than the distance connecting two nodes in the canonical unit cell. We remark here that the cables connecting slave nodes, as explained in Section 3.2.5, have identical pre-stretches to those of the cables connecting the corresponding master nodes, thus we have 192 cables, rather than the original 240 ones, that can have distinct pre-stretches. Since we aim to study the effect of cable pre-stretching on material symmetries, we need to explore a 192-dimensional space of pre-stretches, where the majority of cases would exhibit a general anisotropic or triclinic symmetry. For tractability, we reduce the dimension of our problem (i.e. reducing the number of cables that have distinct pre-stretches) by dividing the 192 cables into groups with identical pre-stretches. This sort of classification into families of cables would allow for a more systematic study of the possible material symmetries. Obviously, choices of classifications are not unique. For this work, we classify the 192 cables into six distinct families based on their orientation and connectivity.

We define two categories of cables, each containing three families of cables. The first category are the cables that span the squares with normal along the X, Y and Z axis, see Figure 3.4. The second category are those lying in the hexagonal faces of the lattice which connect the cables of the first category, named as YZ, XZ, XY (e.g. XZ cables are connect-

ing cables in the X category and Z category).

This classification leads to a six-dimensional space of pre-stretch of different cable families. We define the pre-stretch vector as:

$$\boldsymbol{\lambda} = \begin{pmatrix} \lambda_x & \lambda_y & \lambda_z & \lambda_{yz} & \lambda_{xz} & \lambda_{xy} \end{pmatrix}, \boldsymbol{\lambda} \in \mathbb{R}^6, \tag{3.40}$$

where each component of $\boldsymbol{\lambda}$ represents the magnitude of pre-stretch in the corresponding family, indicated with a subscript. In the rest of the chapter, we abuse the language by calling cables by their pre-stretch. For instance, we would call cables in the Y category as λ_y cables. Let us remark that very large values of pre-stretches, which corresponds to $|\boldsymbol{\lambda}| \ll 1$, are physically irrelevant and thus not considered in our study. After sweeping the physically relevant subset of the aforementioned six-dimensional space, we identify certain sections of interest which will be discussed in the next section.

We emphasize that the material symmetries obtained from the elasticity tensor correspond to the symmetries of a unit cell in the interior of a very large lattice. In our homogenization scheme, we consider $\mathbf{F} = \mathbf{I}$. This is a natural choice for studying the material symmetries of the lattice, treating the pre-stretched lattice as the initial configuration. Note that in the reference configuration ($\mathbf{F} = \mathbf{I}$), the first elasticity tensor computed by Eq 3.19, is equivalent to the Cauchy elasticity tensor, which relates the Cauchy stress to strain [119]. Thus the obtained elasticity tensor will have major and minor symmetries. We also remark here that the energy landscape is assumed to be rank-one convex, as explained in A, for the considered range of pre-stretches $\boldsymbol{\lambda}$, in the vicinity of $\mathbf{F} = \mathbf{I}$.

3.3 Results

In this section, we first explain the rationale of choosing certain pre-stretch scenarios, followed by the material symmetry results for each case. We conclude this section by discussing the symmetries of an infinite lattice -where we solve for the equilibrium con-

figuration of the unit cell subjected to pre-stretch in the presence of PBC-, and explain the obtained results through geometrical considerations, particularly on how they compare to the finite case.

3.3.1 Pre-stretch Cases

Even though we reduce the 192-dimensional space of possible distinct pre-stretches to a six-dimensional one, where each point $\boldsymbol{\lambda} \in \mathbb{R}^6$ represents a distinct pre-stretch case, the number of possible pre-stretching cases remains infinite. Thus, we make judicious choices of scenarios by simple geometrical arguments, rather than sweeping the entire six-dimensional space of pre-stretches, and focus on four different scenarios. In each scenario we group certain components of the $\boldsymbol{\lambda}$ vector together and a range of pre-stretches are applied to distinct groups. The four cases that we will focus on are the following:

$$\begin{aligned}
&\text{Case A: } \lambda_x = \lambda_y = \lambda_z = \lambda_1, \lambda_{yz} = \lambda_{xz} = \lambda_{xy} = \lambda_2 \\
&\qquad \implies \boldsymbol{\lambda} = \begin{pmatrix} \lambda_1 & \lambda_1 & \lambda_1 & \lambda_2 & \lambda_2 & \lambda_2 \end{pmatrix}, \\
&\text{Case B: } \lambda_x = \lambda_y = \lambda_1, \lambda_{yz} = \lambda_{xz} = \lambda_2, \lambda_{xy} = \lambda_z = C \\
&\qquad \implies \boldsymbol{\lambda} = \begin{pmatrix} \lambda_1 & \lambda_1 & C & \lambda_2 & \lambda_2 & C \end{pmatrix}, \\
&\text{Case C: } \lambda_y = \lambda_1, \lambda_{yz} = \lambda_2, \lambda_x = \lambda_z = \lambda_{xz} = \lambda_{xy} = C \\
&\qquad \implies \boldsymbol{\lambda} = \begin{pmatrix} C & \lambda_1 & C & \lambda_2 & C & C \end{pmatrix}, \\
&\text{Case D: } \lambda_y = \lambda_1, \lambda_{xz} = \lambda_2, \lambda_x = \lambda_z = \lambda_{yz} = \lambda_{xy} = C \\
&\qquad \implies \boldsymbol{\lambda} = \begin{pmatrix} C & \lambda_1 & C & C & \lambda_2 & C \end{pmatrix},
\end{aligned} \tag{3.41}$$

where C is a constant parameter. For each case, we examined 1600 pre-stretch scenarios, where both λ_1 and λ_2 range from 0.96 to 1. Figure 3.8 shows each case, where cables undergoing pre-stretches equal to C, λ_1 and λ_2 are respectively colored as black, red and blue. Note that all the cases have numerous equivalent scenarios and their equivalence is

easily justified geometrically, considering the cubic symmetry of the lattice (see Section 3.3.3). For instance, in case B, all the following pre-stretch cases will yield the same symmetry results as case B:

$$\begin{array}{cc}
\begin{pmatrix} \lambda_1 & \lambda_1 & C & C & \lambda_2 & \lambda_2 \end{pmatrix}, & \begin{pmatrix} \lambda_1 & \lambda_1 & C & \lambda_2 & C & \lambda_2 \end{pmatrix} \\
\begin{pmatrix} C & \lambda_1 & \lambda_1 & C & \lambda_2 & \lambda_2 \end{pmatrix}, & \begin{pmatrix} C & \lambda_1 & \lambda_1 & \lambda_2 & C & \lambda_2 \end{pmatrix} \\
\begin{pmatrix} C & \lambda_1 & \lambda_1 & \lambda_2 & \lambda_2 & C \end{pmatrix}, & \begin{pmatrix} \lambda_1 & C & \lambda_1 & C & \lambda_2 & \lambda_2 \end{pmatrix} \\
\begin{pmatrix} \lambda_1 & C & \lambda_1 & \lambda_2 & C & \lambda_2 \end{pmatrix}, & \begin{pmatrix} \lambda_1 & C & \lambda_1 & \lambda_2 & \lambda_2 & C \end{pmatrix}
\end{array} \tag{3.42}$$

Case A

Figure 3.9 shows the symmetry results for the case A. The interior of a large tensegrity lattice has four-fold symmetry in three perpendicular planes, where λ_x, λ_y and λ_z are lying, as it will be explained in detail in Section 3.3.3. According to the definition of cubic symmetry [117], any pre-stretch that maintains the aforementioned four-fold symmetries, leads to a cubic symmetry. Also, the pre-stretched configuration respects that symmetry. This is the case when all the families in each category have identical pre-stretch, as shown in 3.9.

In the unstretched case, i.e. $\lambda_1 = \lambda_2 = 1$, and in a small neighborhood of it, the lattice exhibits floppy modes, which are zero energy modes leading to a stiffness matrix that is not full rank, as seen in the upper right corner of Figure 3.9. If the magnitude of the pre-stretches are large enough, pre-stretching the cables lead to the buckling of bars. The pre-stretches above the blue line and below the purple line lead to buckling of none and all of the bars, respectively. Due to symmetric nature of the case presented in Figure 3.9, all the bars buckle simultaneously.

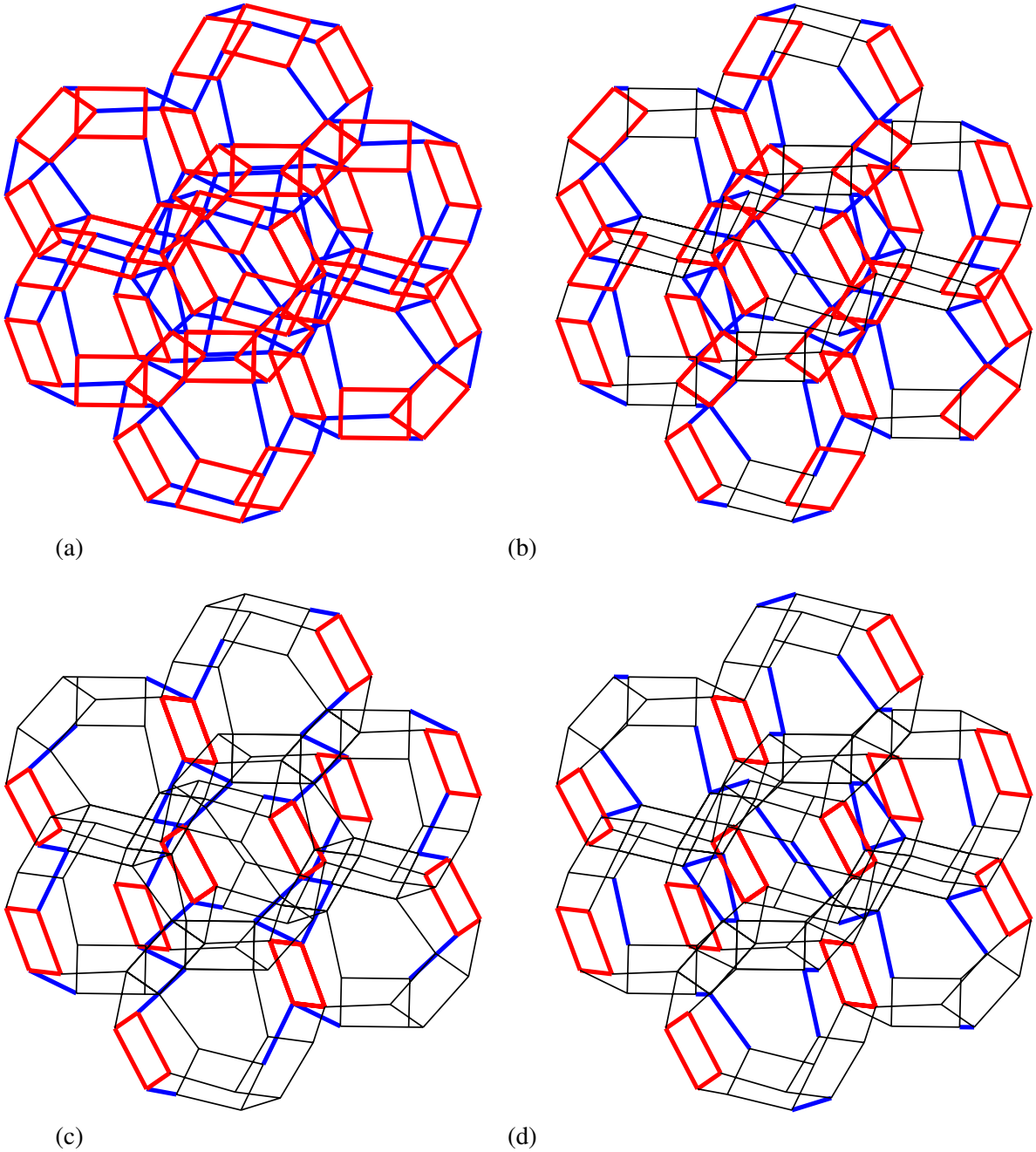

(a) (b)

(c) (d)

Figure 3.8: Representation of four pre-stretch cases of the tensegrity unit cell. Family of cables with pre-stretch λ_1, λ_2 and constant values C are respectively shown in red, blue and black. Also, to better present the cables that are pre-stretched in each case, we are not showing the bars. (a) Case A, (b) Case B, (c) Case C, (d) Case D.

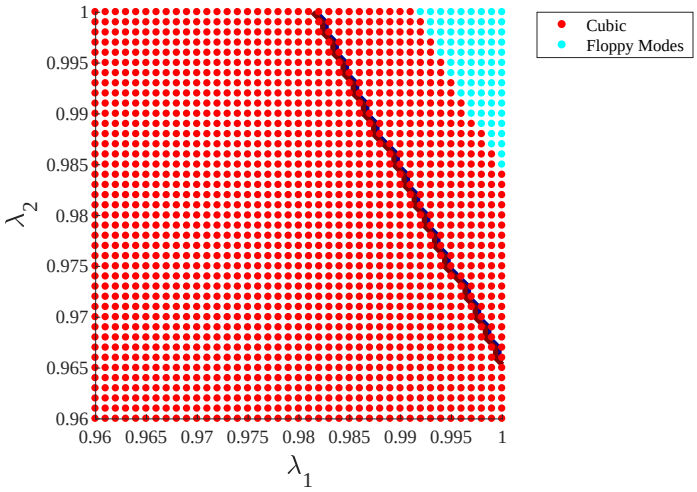

Figure 3.9: Material symmetries for the pre-stretch case A: We have $\lambda_x = \lambda_y = \lambda_z = \lambda_1$ and $\lambda_{yz} = \lambda_{xz} = \lambda_{xy} = \lambda_2$. Blue and purple lines are the boundaries for the zones where none of the cables and all the cables are buckling, respectively. In this case, they coincide.

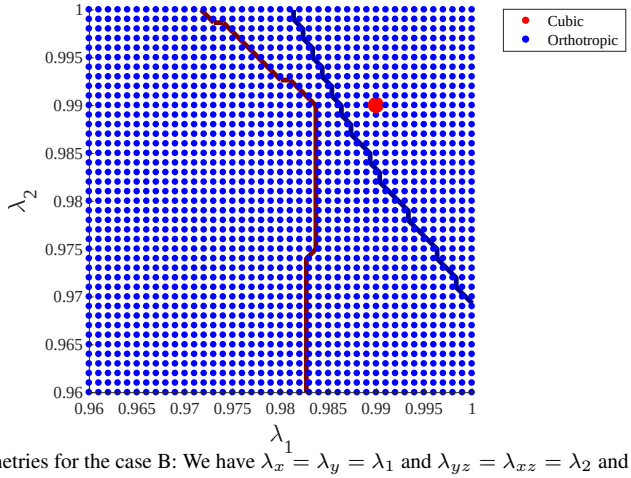

Figure 3.10: Material symmetries for the case B: We have $\lambda_x = \lambda_y = \lambda_1$ and $\lambda_{yz} = \lambda_{xz} = \lambda_2$ and $\lambda_z = \lambda_{xy} = C = 0.99$. Blue and purple lines are the boundaries for the zones where none of the bars and all the bars are buckling, respectively.

Case B

The cubic material symmetry breaks once one of the cable families in any of the categories has a different pre-stretch than the rest of the cables in the same category. We explore this material symmetry breaking by applying a constant pre-stretch of $C = 0.99$ in *Case B* in (3.41). As shown in Figure 3.10, a phase transition from cubic to orthotropic is observed. Yet, when all the pre-streches are equal, the cubic symmetry is recovered. In the rest of cases, the four-fold symmetry in the three perpendicular planes is broken to two-fold symmetry, resulting in orthotropic symmetries.

Let us make two remarks here: I) The magnitude of the constant pre-stretch, i.e. 0.99, will not affect the symmetries and 0.99 is chosen to avoid any possible floppy modes. II) Any combination of pre-stretches that identifies two families of cables in each of the two categories, will yield the same results as Figure 3.10. This is simply due to the original cubic symmetry of the lattice. For instance, $\lambda_z = \lambda_y = \lambda_1$ and $\lambda_{xy} = \lambda_{xz} = \lambda_2$ and $\lambda_x = \lambda_{xy} = C = 0.99$ leads to the same symmetries as Figure. 3.10. Note that contrary to the case A, the blue and purple lines -indicating the boundaries of the zones where none and all of the bars have buckled- are not coincident, thus we have a zone where only a subset of bars are buckling. Also, we observe that symmetries are independent of the buckling of bars.

Cases C and D

We next consider cases C and D, where two families of cables in each category have a constant pre-stretch $C = 0.99$. As shown in Figure 3.11, they display distinct results, both in terms of material symmetries and buckling of bars. Evidently, there exists a plane with four-fold symmetry in a zone of case D, as shown in Figure 3.11b, which yields a tetragonal symmetry. Therefore, contrary to case C, we do observe a transition from orthotropic to tetragonal symmetry in case D. Note that in both cases, cubic symmetry is observed where all the cables have identical pre-stretch, equal to the constant value $C = 0.99$.

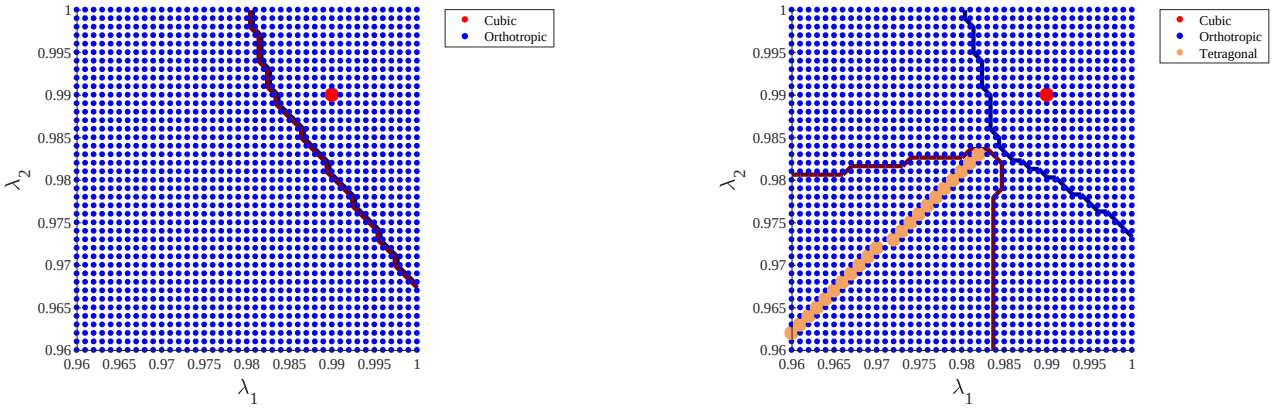

(a) (b)

Figure 3.11: (a) Material symmetries for the pre-stretch case C: We have $\lambda_y = \lambda_1$ and $\lambda_{yz} = \lambda_2$ and $\lambda_x = \lambda_z = \lambda_{xz} = \lambda_{xy} = C = 0.99$; (b) Material symmetries for the pre-stretch case D: We have $\lambda_y = \lambda_1$ and $\lambda_{xz} = \lambda_2$ and $\lambda_x = \lambda_z = \lambda_{yz} = \lambda_{xy} = C = 0.99$. Blue and purple lines are the boundaries for the zones where none of the bars and all the bars are buckling, respectively.

The distinction among cases C and D lies within the connectivity of the set of pre-stretched cables, such that, in cases C and D, the two families of pre-stretched cables are respectively connected and disconnected. Subsequently, the pre-stretched cables in case C lie in intersecting planes, while in case D, all the pre-stretched cables lie in parallel planes. We emphasize that the symmetry results for this case is independent of the choice of families in each category.

We note that, for case D, the lattice exhibits tetragonal symmetry only in the region where all the bars are buckled, see Figure 3.11b. Since buckling necessarily leads to a significant reduction of the stiffness of individual bars, it can be seen as a phase transition of the constituent material of the lattice, which, in turn, enables a phase transition of the entire system.

We also remark here that although $\boldsymbol{\lambda}$ associated to the case D is invariant under exchanging x and z indices, one cannot conclude that case D exhibits tetragonal symmetry. To illustrate this point, we look into the canonical unit cell subjected to pre-stretch case D, from two perpendicular points of view. Using pure geometry, as shown in Figure 3.12, we demonstrate that case D does not have tetragonal symmetry. This point will be further discussed in Section 3.3.3. A similar reasoning applied to the case B, discussed previously.

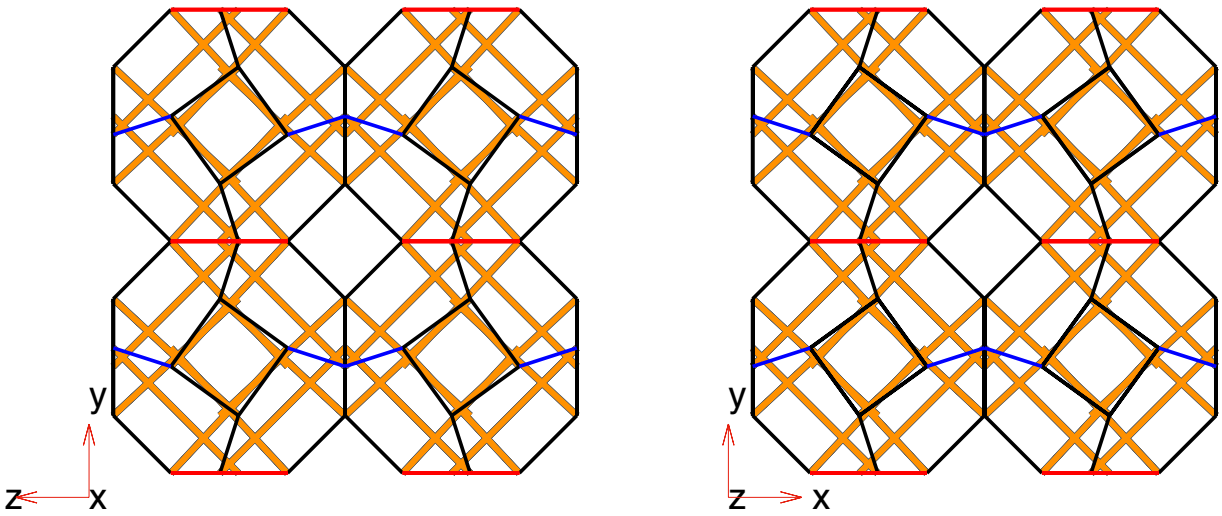

(a) (b)

Figure 3.12: (a) Cross section of the canonical unit cell along the YZ plane; (b) Cross section of the canonical unit cell along the XY plane. Cables shown in red, blue and black respectively represent cables with λ_1, λ_2 and C pre-stretch values. Note that only a subset of cables are shown, to simplify distinguishing between the two different perspectives.

Yet, a fundamental question arises here. We know that the lattice has a four-fold symmetry, and that the pre-stretch scenario in case D respects the four-fold symmetry of the lattice in a plane. Thus, it would be reasonable to expect a tetragonal symmetry everywhere. The question is then, why do we obtain orthotropic symmetry as well? In other words, while the pre-stretch has four-fold symmetry, what leads to a symmetry breaking? We try to answer this question in the remainder of this section.

To further understand this case, we examine the equilibrium configuration of the unit cell subjected a priori to pre-stretch. Figure 3.13 contains the cross-sectional views of the deformed configurations in two pre-stretch scenarios from case D, where Figure 3.13a and Figure 3.13b correspond to a tetragonal and orthotropic symmetry. From a purely geometric perspective, we observe that the equilibrium configuration due to the applied pre-stretch scenario, exhibits an inhomogeneous shear in the orthotropic case. This distortion in the lattice breaks the four-fold symmetry (explained in more detail in section. 3.3.3), which is observed in the cubic case, and leads to orthotropic symmetry. Besides, the presence of

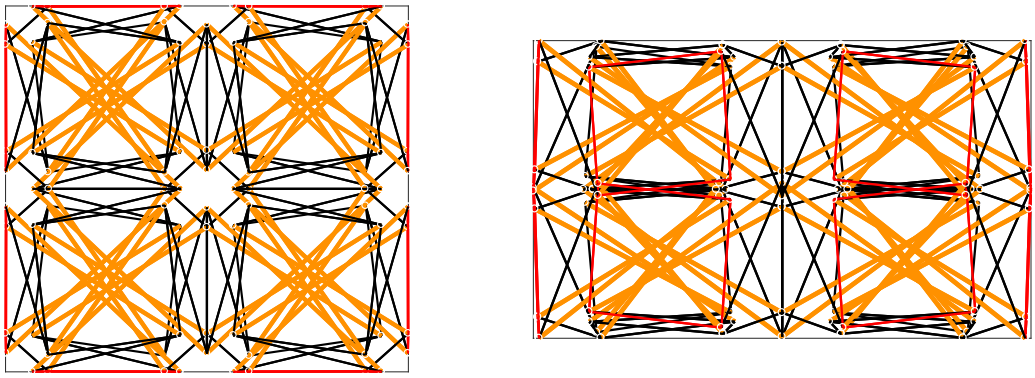

(a) (b)

Figure 3.13: Geometry of the equilibrium configuration of the unit cell dictates the symmetry (a) Cross section of the deformed lattice for a tetragonal scenario in case D, with $\lambda_y = \lambda_1 = 0.985$, $\lambda_{yz} = \lambda_2 = 0.985$ and $\lambda_x = \lambda_z = \lambda_{xz} = \lambda_{xy} = C = 0.99$; (b) Cross section of the deformed lattice for a orthotropic scenario in case D, with $\lambda_y = \lambda_1 = 0.985$, $\lambda_{xz} = \lambda_2 = 0.95$ and $\lambda_x = \lambda_z = \lambda_{yz} = \lambda_{xy} = C = 0.99$. black and orange lines represent bars and cables. To demonstrate the transition to inhomogeneous deformation, the cables in the outer facets are shown in red. To exhibit the inhomogeneous deformation in the outer facets, displacements are magnified.

a band of tetragonal symmetry is due to a special distortion on those specific pre-stretch values where a plane with four-fold symmetry is preserved. This is analogous to accidental degenerecies observed in various condensed matter systems [120].

We also explore the effect of the constant pre-stretch, C, on the symmetry phase diagram. Figure 3.14 shows the results for the cases where $C \in \{0.991, 0.992, 0.993, 0.994\}$. Evidently, regardless of the value of C, tetragonal cases are obtained only after all the bars have buckled. As mentioned before, due to the non-homogeneous buckling of bars, only the state when all the bars are buckled allows for existence of the four-fold symmetric plane and consequently exhibition of tetragonal symmetries in a band close to the diagonal.

A numerical example

In this section, we look into one specific pre-stretch scenario, included in case D -see Section 3.3.1-, to point out some issues that arise from numerical implementation of the

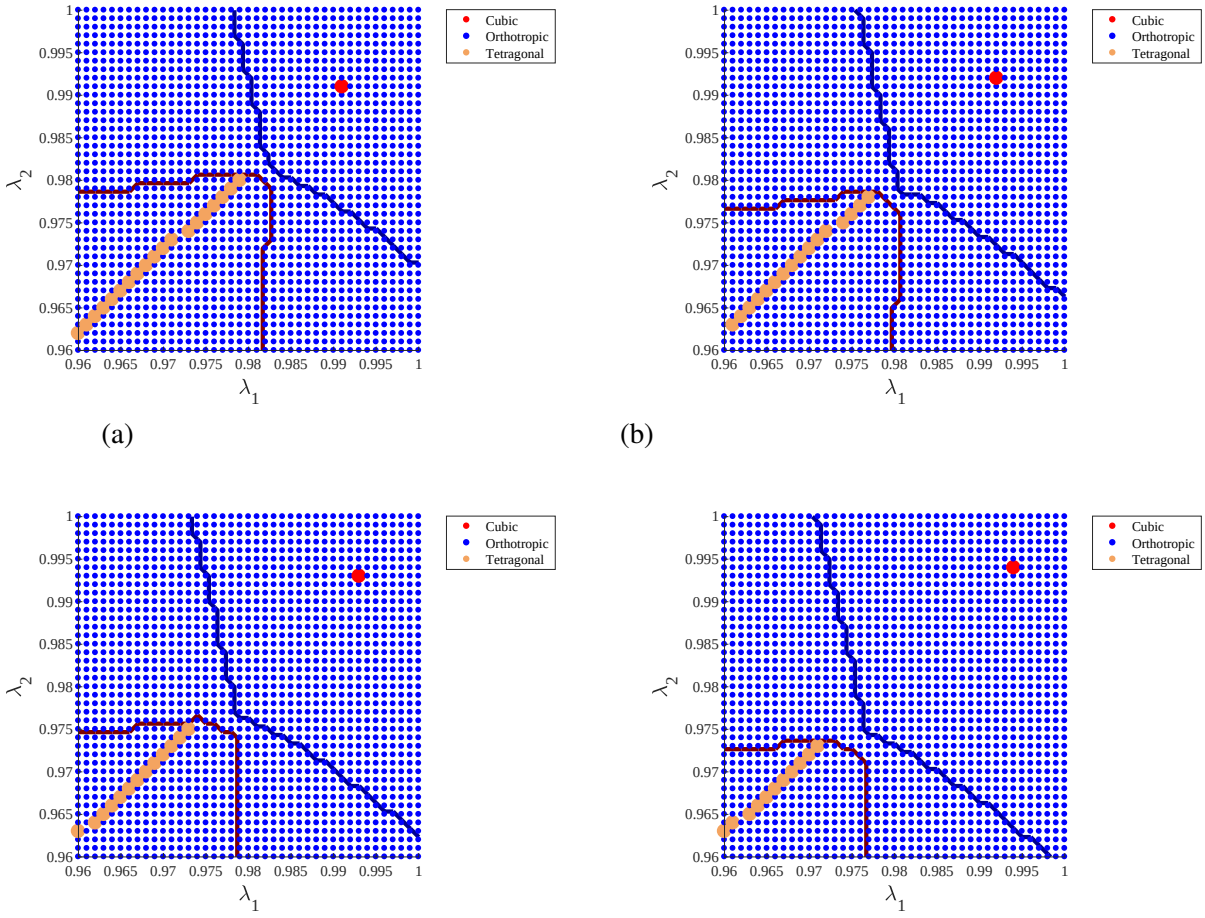

Figure 3.14: Material symmetries for the pre-stretch case D: We have $\lambda_y = \lambda_1$, $\lambda_{xz} = \lambda_2$ and $\lambda_x = \lambda_z = \lambda_{yz} = \lambda_{xy} = C$, where (a):$C = 0.991$; (b):$C = 0.992$; (c):$C = 0.993$; (d):$C = 0.994$. Blue and purple lines are the boundaries for the zones where none of the bars and all the bars are buckling, respectively.

theorems. Let us then consider the following pre-stretch scenario:

$$\boldsymbol{\lambda} = \begin{pmatrix} 0.99 & 0.98 & 0.99 & 0.99 & 0.98 & 0.99 \end{pmatrix}. \tag{3.43}$$

After solving the equilibrium equations and homogenizing the lattice, we obtain the following elasticity tensor:

$$[\mathbb{C}] = 10^6 \times \begin{pmatrix} 2.3801655462 & 1.9871944741 & 1.9448676617 & -0.000000000007 & -0.000000000008 & 0.000000000002 \\ 1.987194474176 & 2.497532203433 & 1.987194429190 & 0.000000000002 & -0.000000000010 & 0.000000000005 \\ 1.94486766178 & 1.987194429190 & 2.380165457358 & -0.000000000008 & -0.000000000004 & -0.000000000001 \\ -0.000000000007 & 0.000000000001 & -0.000000000008 & 1.737565973286 & 0.000000000008 & -0.000000000008 \\ -0.000000000008 & -0.000000000010 & -0.000000000004 & 0.000000000008 & 1.709012755196 & -0.000000000003 \\ 0.000000000002 & 0.000000000005 & -0.000000000001 & -0.000000000008 & -0.000000000003 & 1.737565918942 \end{pmatrix} \tag{3.44}$$

The sorted eigenvalues of the $[\mathbb{C}]$ are obtained:

$$\boldsymbol{\lambda} = 10^6 \times \begin{pmatrix} 0.435297840024970 \\ 0.456147573667622 \\ 1.709012755195620 \\ 1.737565918941615 \\ 1.737565973285677 \\ 6.366417793362083 \end{pmatrix}. \tag{3.45}$$

According to the aforementioned criteria, we require 5 or 6 distinct eigenvalues for tetragonal or orthotropic symmetry, respectively. It is evident from (3.45) that if we impose a tolerance of $1e-7$ or larger, the first condition of the tetragonal symmetry is satisfied. Also, the rest of the conditions required for obtaining a tetragonal symmetry are satisfied. In light of this example, we found that for relatively large values of the tolerances, the tetragonal band observed in case D -see section 3.3.1- becomes thicker. The above example illustrates the need for a careful examination of the theoretical conditions. It also serves as a motivating example for potential future paths on constructing measures of symmetry

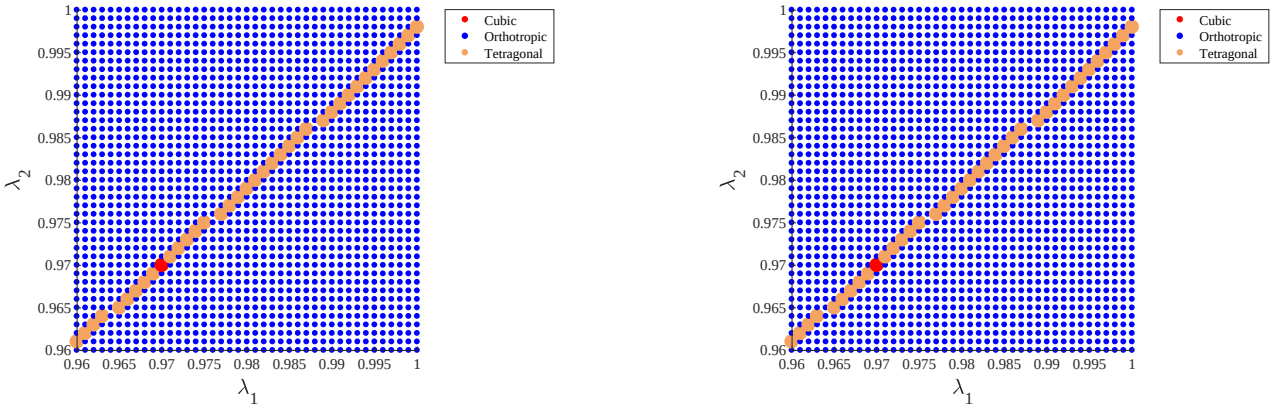

(a) (b)

Figure 3.15: Effect of the unit cell size on the phase diagram for pre-stretch case D, where $\lambda_y = \lambda_1$, $\lambda_{yz} = \lambda_2$ and $\lambda_x = \lambda_z = \lambda_{xz} = \lambda_{xy} = C = 0.97$: (a) Material symmetries for the lattice for $2 \times 2 \times 2$ unit cell, (b) Material symmetries for the lattice with $4 \times 4 \times 4$ unit cell.

in 3D, which quantifies deviations from each symmetry.

3.3.2 Note on the effect of unit cell size on the symmetries

In this section, we address the question of whether the unit cell size plays a role in the material symmetries of the tensegrity lattice. To this end, we double the unit cell size in each direction, (i.e. $4 \times 4 \times 4$ unit cell, with 4 octahedron in each direction, see section 3.2.1) and examine the symmetries of the corresponding lattice, subject to the relatively 'complicated' pre-stretch case D. Figure 3.15 compares the symmetry results for case D of lattices with $4 \times 4 \times 4$ and $2 \times 2 \times 2$ unit cells. Evidently, the phase diagram for the lattices with different unit cell sizes are identical. We obtain similar results for other pre-stretch cases. Note that due to the constant pre-stretch of $C = 0.97$, all the bars buckle. We also performed similar computations for a lattice with an $8 \times 8 \times 8$ unit cell and obtained identical results to lattices constructed with $4 \times 4 \times 4$ and $2 \times 2 \times 2$ unit cells.

As mentioned before, we model the interior of a large lattice, constructed by tessellating the unit cell in space. Thus, the symmetries that are obtained through the homogenization scheme are associated with the entire lattice. The exhibition of identical symmetries in the lattices obtained by tessellating the $2 \times 2 \times 2$, $4 \times 4 \times 4$ and $8 \times 8 \times 8$ unit cells follows from

the fact that the deformed configurations (caused by pre-stretch) in the resultant lattices are identical. This is a natural outcome of applying a pre-stretch field to the entire domain. For further clarification, let us consider a lattice constructed from an $N \times N \times N$ unit cell, undergoing a pre-stretch field. Since the pre-stretches are applied everywhere, the deformed configuration of the lattices constructed from $N \times N \times N$ and $2 \times 2 \times 2$ unit cells will have identical geometries, given that the pre-stretch fields are identical. Therefore, since identical geometries lead to identical elasticity tensors, the symmetries are not dependent on the size of the unit cell.

3.3.3 Infinite vs. finite lattice: Surface effects on symmetry phases

As discussed in section 3.3.1, even though the lattice has four-fold symmetry and the applied pre-stretch is symmetry-preserving, the deformed lattice is not necessarily tetragonal. This observation is justified by looking at the geometry of the pre-stretched unit cell, where an inhomogeneous shear causes a symmetry breaking from tetragonal to orthotropic. However, the resultant inhomogeneous shear deformation is not consistent with having PBC, meaning that the obtained symmetries are valid for a finite lattice rather than an infinite lattice. This motivates us to look into symmetries of an infinite tensegrity lattice, where we model the infinite lattice by imposing PBC.

We solve for the equilibrium of tensegrity unit cell under PBC, using the theory developed in section 3.2.4, subject to the pre-stretch case D. Once the equilibrium configuration of the pre-stretched unit cell is determined, we proceed as before to compute the effective elasticity tensor and examine the corresponding material symmetries. As shown in 3.16, the infinite lattice exhibits tetragonal symmetry everywhere, except when $\boldsymbol{\lambda} = \mathbf{C} = 0.97$, which corresponds to cubic symmetry. The pre-stretch field in case D respects tetragonal symmetry, and unlike the finite case, the infinite lattice deforms in a symmetry-preserving fashion. This shows that tensegrity-based metamaterials can exhibit distinct material symmetries in the finite and infinite case. In other words, for our metamaterial, terminating the

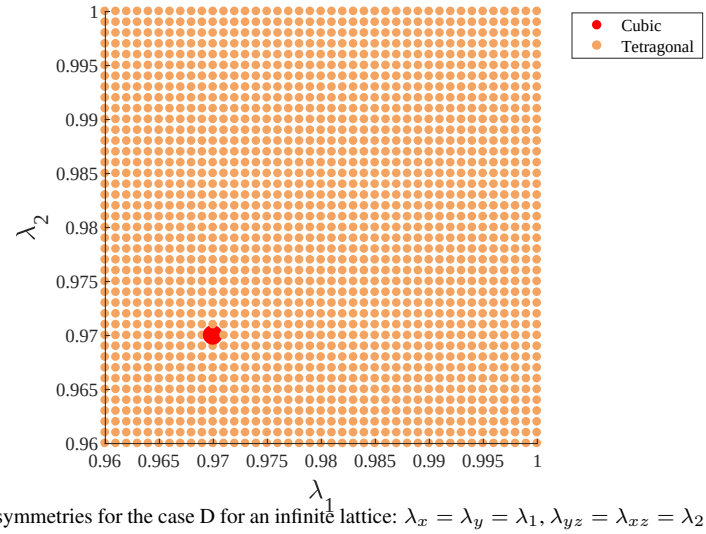

Figure 3.16: Material symmetries for the case D for an infinite lattice: $\lambda_x = \lambda_y = \lambda_1$, $\lambda_{yz} = \lambda_{xz} = \lambda_2$ and $\lambda_z = \lambda_{xy} = C = 0.97$.

lattice and creating a surface leads to material symmetry breaking. This is in contrast with studies on natural materials, where decreasing the size of the system, and consequently increasing the surface effects, leads to symmetry reduction [60, 61]. This class of metamaterials has a particular property that is discussed in the next subsection.

Non-symmorphic lattices: Observations on the tensegrity lattice

In this section, we discuss a fundamental aspect of the tensegrity unit cell that leads to the discrepancy of the symmetries of the infinite and finite lattice. From a symmetry point of view, lattices are divided in two broad categories: symmorphic and non-symmorphic lattices. Symmorphic lattices are defined as lattices whose space group, apart from translations, is solely composed of point group operations. In contrast, non-symmorphic lattices are defined as lattices with space group consisting of glide elements in addition to point-group symmetries [121].

The tensegrity unit cell in this study is a non-symmorphic lattice. This is due to the fact that once a 90 degrees rotation is applied and the unit cell is glided by half a unit cell size, we obtain a lattice identical to the one prior to rotation. Due to the rather complex geometry of the tensegrity unit cell, this might not be easy to observe. Figure 3.17 shows

the full and half tensegrity unit cell with their corresponding cross-sections.

Let us rotate the full tensegrity unit cell by 90 degrees and focus on its cross-section. Evidently, the rotated cross-section, as shown in 3.18a, is distinct from the initial one 3.17b (note that the bars are pointing in different directions). However, the rotated cross-section is identical to the initial mid-plane cross-section of the unit cell 3.17d. To facilitate comparing the rotated cross-section with the initial mid-plane cross-section, they are presented in Figure 3.18. Consequently, if we glide the unit cell after the rotation, we would obtain four-fold symmetry. This proves, from a pure geometric point of view, that the infinite tensegrity lattice has four-fold symmetry. Since the aforementioned glide can only happen in the infinite case, this is not valid for the finite lattice.

3.4 Summary and concluding remarks

In this work, we have characterized material symmetry phase transitions in three-dimensional tensegrity-based metamaterials, occurring solely by varying pre-stretches in the cables. In a systematic manner, we first defined six families of cables, obtained through clustering subsets of cables according to i) orientation, and ii) the planes that they lie in, and then identified the pre-stretches in all the cables of each family. After careful and thorough examinations of the resulting six-dimensional space of pre-stretches, important two-dimensional sub-spaces are identified. For each of them, we examined 1600 different pre-stretch scenarios and presented the associated phase diagrams. For each pre-stretch scenario, we found the corresponding material symmetry of the lattice by examining the eigenspaces of the effective elasticity tensor, obtained through homogenizing the equilibrium configuration of the pre-stretched lattice. It is worth remarking that the techniques and approaches that are employed in this work are general and could be applied to any discrete system with translational symmetry.

We have demonstrated orthotropic to cubic, orthotropic to tetragonal and cubic to tetragonal material symmetry phase transitions in finite tensegrity lattices. We also ob-

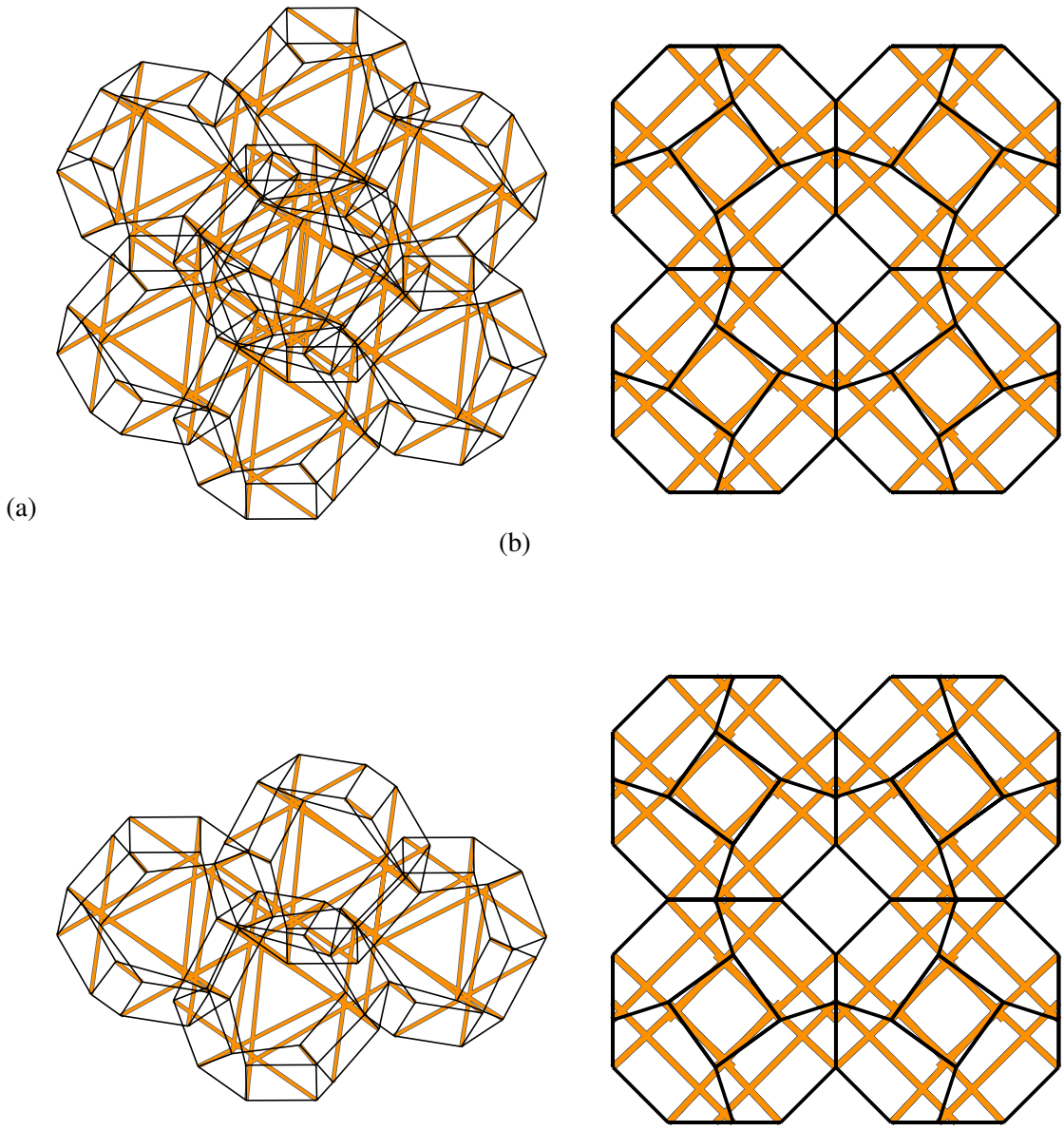

Figure 3.17: The tensegrity is a non-symmorphic lattice where bars and cables are respectively shown in black and orange. (a) and (c) are perspective of full and half unit cell with (b) and (d) as the corresponding cross-sections. Note the distinction between cross-sections is more evident if one focuses on the out of plane direction of bars. We Note that only a subset of cables are shown, to simplify the distinction between the two different perspectives.

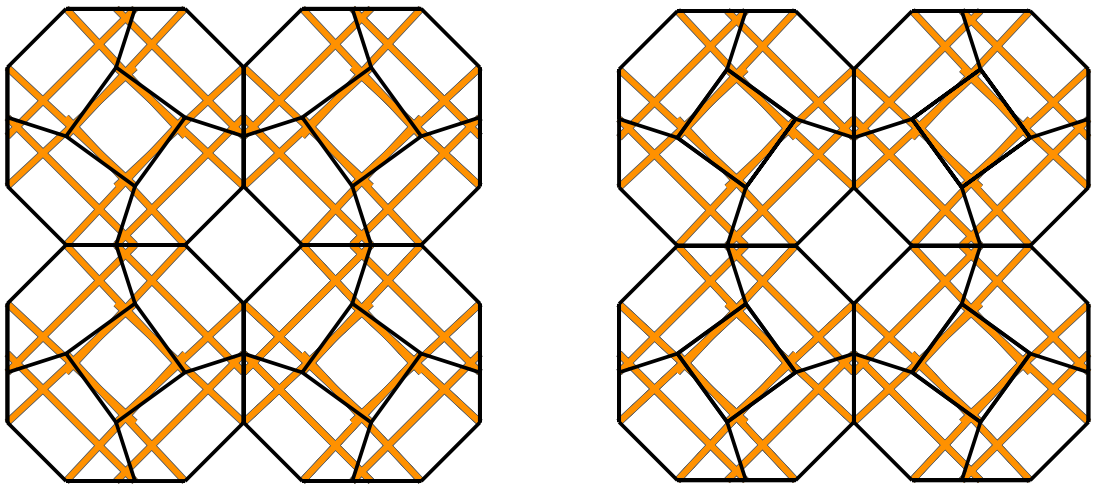

(a) (b)

Figure 3.18: Comparing the mid-plane section and 90° rotated front facet. The infinite tensegrity lattice has four-fold symmetry, obtained by a rotation and a glide of half unit cell size.We Note that only a subset of cables are shown, to simplify the distinction between the two different perspectives.

served that the transition from orthotropic to tetragonal symmetry occurs only when all the bars in the tensegrity lattice have buckled. Furthermore, to explain the phase transitions we observed, we analyzed the deformed configuration of the pre-stretched lattice. To the best of our knowledge, this is the first time material symmetry phase transitions in tenegrity-based metamaterials are characterized, which is analogous to solid-solid phase transitions in materials. This could prove useful for a variety of engineering applications. For example, having tunable material symmetries could serve as a foundation for adaptive stress wave propagation in impact mitigation and force protection applications. Also, one could envision the possibility of a tensegrity metamaterial in which alternating symmetry phases are present forming effective microstructures similar to those observed in shape memory alloys.

To conclude our work, we formulated a constrained optimization problem to study the symmetries of an infinite-dimensional tensegrity lattice. We observed that the orthotropic phases found in the finite case are replaced by tetragonal symmetries in the infinite lattice, even though both cases are subjected to identical pre-stretch fields. We have shown that

this discrepancy among the finite and infinite lattice is i) due to the particular deformation of the finite lattice in a way that breaks the tetragonal symmetry, ii) the non-symmorphic nature of the tensegrity lattice, and iii) boundary effects. This discrepancy has vast implications for computational modeling of lattices and using periodic boundary conditions to mimic a very large system. Based on our results, depending on the deformation type, imposing periodic boundary conditions could lead to an incorrect prediction of the effective material symmetry. We also remark that unlike natural materials, where increasing the size of the system leads to obtaining lower symmetries [60] we found a class of metamaterials where the infinite lattice exhibits a higher symmetry than the finite one. Based on our observations, we envision the presence of similar patterns in other architectured-materials. We also claim that if members of a non-symmorphic lattice are prestressed in a symmetry-preserving fashion, the finite and infinite lattice can exhibit different symmetries.

CHAPTER 4
EFFECTS OF CONNECTIVITY ON THE MECHANICAL RESPONSE OF LATTICES: 2D TENSEGRITY SYSTEMS

4.1 Introduction

Global properties of a lattice, subjected to a nonlocal external loading -or excitation in a more general context-, are often significantly affected by a localized deformation. This arises in a wide range of problems across multiple scales. Notable examples are: plastic twinning in metals [122], homogeneous dislocation nucleation [4], localized buckling of epithelial cell in biological systems [123] and chevron folds in rocks [124]. These localized deformations often happen as a result of an instability, either at the microscopic and material level or that the macroscopic and structural level, and they lead to formation of patterns or phase transitions [2, 125].

Several studies have focused on pattern formations in periodic media, including continuum and discrete systems -lattices- [65]. Creation of these patterns affects several mechanical properties of their corresponding system. For example, Bertoldi and Boyce have demonstrated how instabilities in soft polymers induce changes in the frequency band structure of periodic phononic systems [126]. Pal et al [14, 127], have extensively investigated the static and dynamic properties of hexagonal lattices and demonstrated that instabilities can lead to the surface confinement of elastic waves. They also have demonstrated emergence of localized solutions in both 2-dimensional and 1-dimensional lattices[128].

Once the mechanical response of a system emerges as a localized deformation, a ‘weak’ zone is introduced to the system, which would non decreasingly deteriorate if the external loading is maintained or increased. Thus prediction and design of localized patterns have been the objective of several studies, such as investigation of localization behavior in peri-

odic media [129], and are considered open challenges in the understanding of failure and post-buckling behavior. This problem has also been investigated in the case of continuous systems, where localization is manifested as a discontinuous strain distribution; which is examined primarily by checking the loss of ellipticity conditions through the Hessian of the strain energy [130]. Yet, the relation to the microstructure and the effect of the macroscopic geometry, including boundary conditions, is not understood well.

In fact, unlike diffuse instabilities and deformations, there is no recipe for studying and predicting localized deformations. Several studies [131, 132] have demonstrated, both numerically and experimentally, how buckling at the microstructural level evolves into localized deformations. For example, Papka and Kyriakides [133, 134] investigated the crushing of honeycomb cellular lattices under a variety of loading conditions. More recently, dAvila et al. [135] have demonstrated that the onset of localization in a periodic composite depends on the effective tangent stiffness of the composite and occurs only if this stiffness in the loading direction is negative. There have also been studies on localized vibration modes called intrinsically localized modes or discrete breathers, where localization arises as a consequence of discreteness and nonlinear interactions [136, 137].

In this chapter, we aim to investigate a hypothesis that relates the connectivity of the lattice, as a topological parameter, with its mechanical response. We also remark that the effect of lattice geometry, such as node geometry, on the corresponding mechanical properties of truss lattice architectures has recently been studied [138, 139]. In the interest of simplicity and tractability, we restrict our investigations to 2-dimensional tensegrities. Our hypothesis is that by purely changing the lattice topology, through isolating the compressive members -which are allowed to buckle and undergo large deformations-, global stability and properties could be altered. For the sake of this investigation, we introduced new designs of 2-dimensional tensegrities, as well as 2-dimensional lattices with connected sets of compression members. In the remaining of this chapter, we first describe the criterion for verifying that a tensegrity lattice is stable -we note that checking the stability

is necessary, since, unlike in previous chapter, new designs are introduced-. Then we introduce our new designs, with very similar geometry, differing only in the connectivity of compression members. We finally present the results for quasi-static tests. We believe that our results serve as strong evidence for our hypothesis, which motivates future research for a rigorous proof.

4.2 2D tensegrities

As discussed in the previous chapter, tensegrity structures have only two types of members: bars -or struts-, which are always in compression; and cables, which are always in tension. Since we are introducing new designs of 2-dimensional tensegrities, we have to check for their prestress stability, which we will define in the next subsection. After all, we want to investigate emergence of localized deformation on lattices which are stable.

4.2.1 Prestress stability of tensegrities

In this section, which is mainly based on the works of Ohsaki as well as Connelly [140, 141, 50], we present the theory for prestress stability of tensegrity structures. Let us remark that here we focus on a specific definition of stability that hinges on the lattice connectivity and geometry, rather than solely on the tangent stiffness of energy functional, as we extensively discussed in chapter two. Yet, the concepts of stability that are demonstrated in here are connected, and equivalent for the most part, with those described in chapter two. Besides, the primary reason for discussing prestress stability, which is also known as 'superstability', is its generality, which makes it independent of selection of the materials and levels of prestresses. For the sake of completeness, we will present the theory for general 3-dimensional structure, even though we only deal with 2-dimensional systems in this chapter.

Let us consider a d-dimensional tensegrity structure, where $d = 3$, which consists of n and m members. Also, once a coordinate system is fixed, the coordinate vectors along x, y

and z directions are denoted by $\mathbf{x}$, $\mathbf{y}$ and $\mathbf{z}$ $(\in \mathbb{R}^n)$, respectively. We define a connectivity matrix $\mathbf{C}$ as follows: $\mathbf{C}$ has m rows and n columns, and each component in row *k*, which is associated to member *k*, is zero, unless they correspond to the end nodes of *k*. If nodes *i* and *j* $i < j$ are the end nodes of *k*, the *ith* and *jth* component of row *k* will be 1 and -1, respectively. Hence, sum of all the elements in each row vanishes.

Let us define the force density vector $\mathbf{q}$ as an m dimensional vector, where each component q_k -associated to the *kth* member-, is the ratio of force in that member to its respective length. We define the force density matrix, as follows:

$$\mathbf{E} = \mathbf{C}^T \text{diag}(\mathbf{q})\mathbf{C}. \tag{4.1}$$

Now let $\mathbf{u}, \mathbf{v}$ and $\mathbf{w}$ $(\in \mathbb{R}^m)$ denote the vectors consisting of the differences of members in x, y and z directions, respectively. We can write them in terms of the connectivity matrix and the nodal coordinate vectors as

$$\begin{aligned} \mathbf{u} &= \mathbf{C}\mathbf{x}, \\ \mathbf{v} &= \mathbf{C}\mathbf{y}, \\ \mathbf{w} &= \mathbf{C}\mathbf{z}. \end{aligned} \tag{4.2}$$

Let us define the diagonal form of $\mathbf{u}, \mathbf{v}$ and $\mathbf{w}$ as $\mathbf{U}, \mathbf{V}$ and $\mathbf{W}$.

Finally we define a 'geometry matrix' $\mathbf{G} \in \mathbb{R}^{m\times 6}$. $\mathbf{G}$ is determined only by connectivity and nodal coordinates of the structure as

$$\mathbf{G} = (\mathbf{Uu}\ \mathbf{Vv}\ \mathbf{Ww}\ \mathbf{Uv}\ \mathbf{Uw}\ \mathbf{Vw}). \tag{4.3}$$

We note that for 2-dimensional structures, the gometry matrix $\mathbf{G} \in \mathbb{R}^{m\times 3}$ becomes

$$\mathbf{G} = (\mathbf{Uu}\ \mathbf{Vv}\ \mathbf{Uv}). \tag{4.4}$$

Note that the number of columns of $\mathbf{G}$ is $d(d+1)/2$ for a d-dimensional structure.

With the above definitions, we state the following lemma, based on the works of Zhang and Ohsaki [140]. It must be emphasized that we assume the structures are not 'degenerate'. This means they do not lie in a hypersurface of the d-dimensional space. For example, in 3-dimensional space, a 2-dimensional structure would be degenerate. With this in mind, the following lemma [140] is stated:

Lemma. If a d-dimensional tensegrity structure is stable with positive quadratic form of the tangent stiffness matrix, that is if $\mathbf{K}$ is the tangent stiffness matrix, for any non-trivial motion $\mathbf{d}$ -excluding the rigid body motions-

$$Q = \mathbf{d}^T \mathbf{K} \mathbf{d} > 0, \tag{4.5}$$

then rank of the geometry matrix $\mathbf{G}$ defined in Eq. (4.3) or Eq. (4.4) is equal to $d(d+1)/2$.

We now present the lemma, that provides the necessary and sufficient condition for prestress stability, also known as superstability.

Lemma. If the following three conditions are satisfied, then the d-dimensional tensegrity structure is stable, irrespective of selection of materials and level of self-stresses:

1. The force density matrix $\mathbf{E}$ has the minimum rank deficiency $d+1$.
2. $\mathbf{E}$ is positive semi-definite.
3. Rank of the geometry matrix $\mathbf{G}$ is $d(d+1)/2$.

The proofs are presented in the Zhang and Ohsaki article [140]. It is worth mentioning that the above concepts, for the most part, were initially presented by Connelly, and he was the first one to show that a tensegrity structure is stable if *the members do not lie on the same conic at infinity*. Zhang and Ohsaki [140] showed that the former lemma is equivalent to the Connelly conditions.

In the next section, we will present our recent designs of 2-dimensional tensegrity lattices, and apply the previously mentioned lemmas on our new designs.

4.2.2 New 2D designs

We present new designs of 2-dimensional tensegrity unit cells, where bars are isolated and cables are connected. Fig. 4.1 shows our proposed designs.

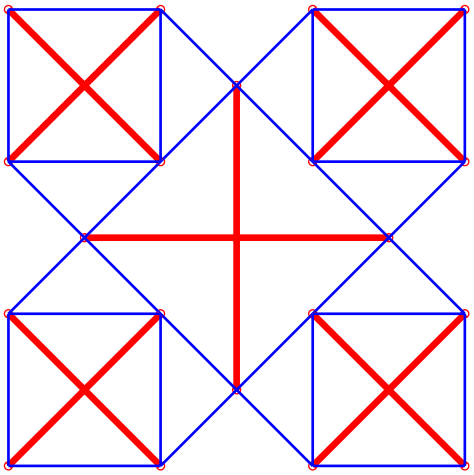

(a)

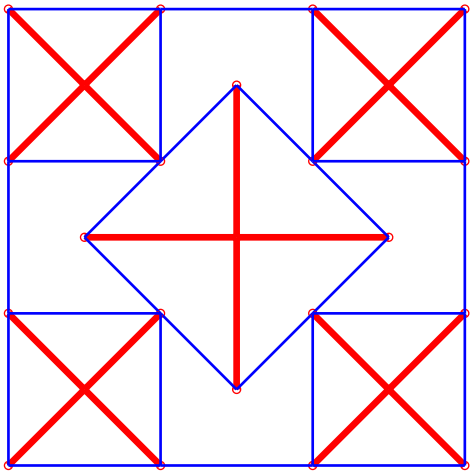

(b)

Figure 4.1: 2-dimensional tensegrity unit cells, where bars and cables are shown in red and blue, respectively.

In both unit cells, it is obvious that the bars, which are shown in red -cables are shown in blue-, are not connected and create isolated subsets of members. The primary advantage of these designs is that they could be easily transformed to 2-dimensional lattices where bars are connected, making them ideal designs to examine our hypothesis. This is due to

the existence of a large square domain, surrounded by smaller squares in the middle of each unit cell. Note that rotation of the large central square domain by 45 degrees would lead to connection of bars in opposite sided peripheral squares , thus creating a connected set of bars. This is illustrated in the next Fig. 4.2. Note that a connected set of bars will create a continous path of compression, as opposed to a discontinous compression path in the case of isolated bars.

We next apply the lemmas mentioned in the previous section to check for their stability. As described, we first compute the force density matrix, $\mathbf{E}$, followed by computation of $\mathbf{G}$ matrix.

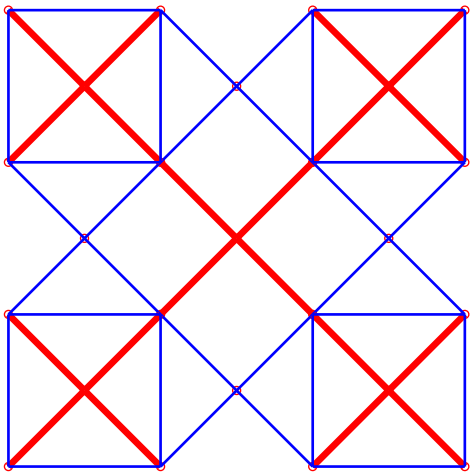

Figure 4.2: 2-dimensional unit cell, with connected set of bars, bars and cables are shown in red and blue, respectively.

These unit cells, obviously, tessellate the 2-dimensional space, and one can easily create beams or plates of any arbitrary geometry, making use of the above unit cell. Lastly, we check to ensure the three conditions associated with the last lemma mentioned in previous subsection apply accordingly. The results demonstrate that all three conditions are met, with $\mathbf{G}$ having a rank deficiency of 3, as well as a positive definite $\mathbf{E}$ with at least rank deficiency of 3. We performed these calculations for various sizes of lattices, and different beam and plate geometries for all the three unit cells proposed. This verifies that our lattices are prestress stable, or superstable.

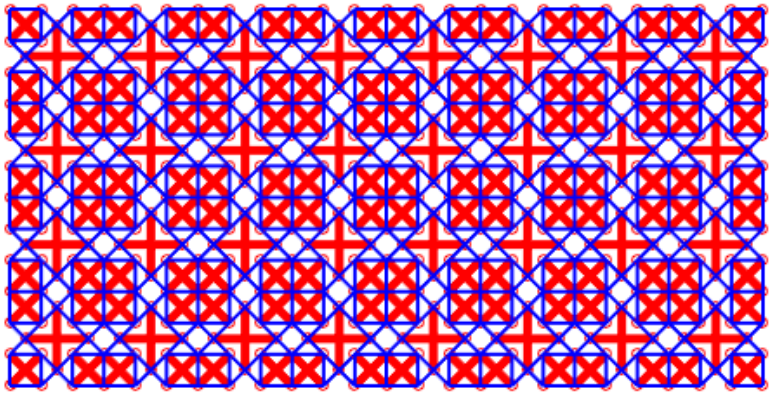

(a)

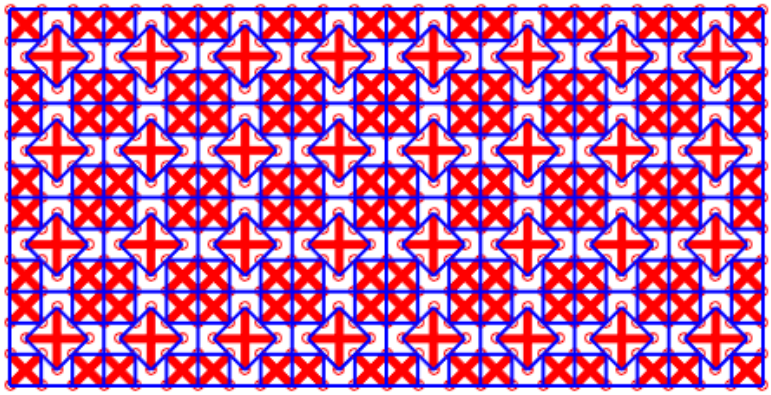

(b)

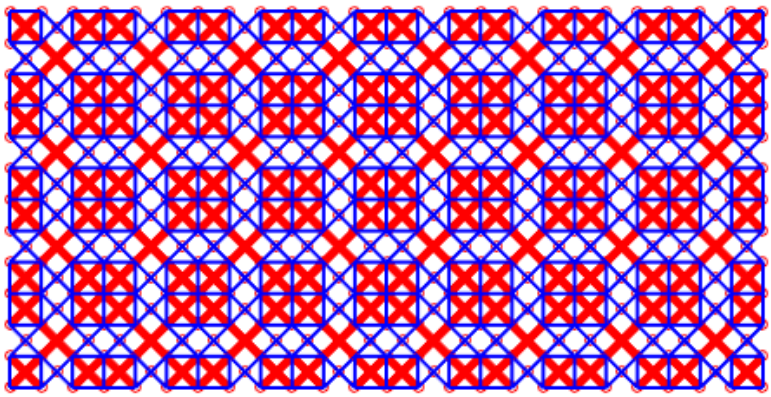

(c)

Figure 4.3: 2-dimensional beams with bars and cables shown in red and blue, respectively.

4.2.3 Effect of connectivity on the mechanical response

In this subsection, we investigate the effect of connectivity on the mechanical response of the proposed 2-dimensional lattices. Let us consider the new unit cells, introduced in the previous subsection, shown in Fig. 4.1 and 4.3a. These two lattices are very similar, apart from a difference in the 'lattice topology', where the bars are connected in the first configuration and isolated in the other. We will abuse the language by referring to this distinction between the lattices as a topological difference, so that either of the lattices can be transformed to the other one only by a topological transformation. We emphasize that our goal is to investigate the effect of this topological difference on the mechanical response and global stability of both lattices.

In each lattice, we model every member using the discrete model that was used in the 3-dimensional tensegrity lattice in Section 3.2.2; all members are connected by pin joints.

We construct a 4×4 domain, from both unit cells, as shown in Fig 4.4. We then apply a pre-stretch λ to all the cables, which are shown in blue in 4.4, using the same definition of pre-stretch as in the previous chapter. Note that we defined λ as a 6-dimensional vector in the previous chapter due to existence of six families of cables, while we have only one family of cables here. In other words, all cables are subjected to an identical pre-stretch λ. As mentioned before, we use the constitutive relation in 3.7, and solve for the pre-stretched equilibrium. To solve for the equilibrium configuration of the pre-stretched lattice, we impose three displacement boundary conditions to prevent rigid body translations and rotation. For the current results, we have chosen $\lambda = 0.999$ and imposed a pin -displacement in both directions is zero- and roller -displacement in the vertical direction is zero- boundary condition in the bottom left and bottom right of each lattice, respectively.

We then study the mechanical response of both lattices subjected to compressive loading. Note that our initial configuration in each step is the pre-stretched configuration. For each lattice shown in 4.4, we impose rollers on all the nodes lying in the left and bottom sides, which prevent displacements in the corresponding normal directions. This set of

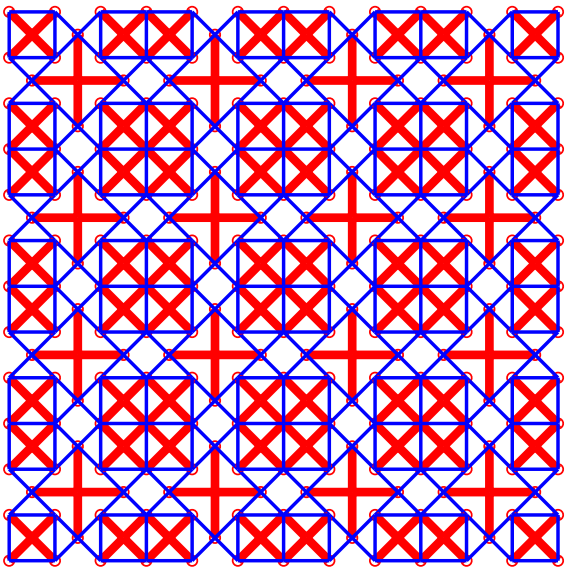

(a)

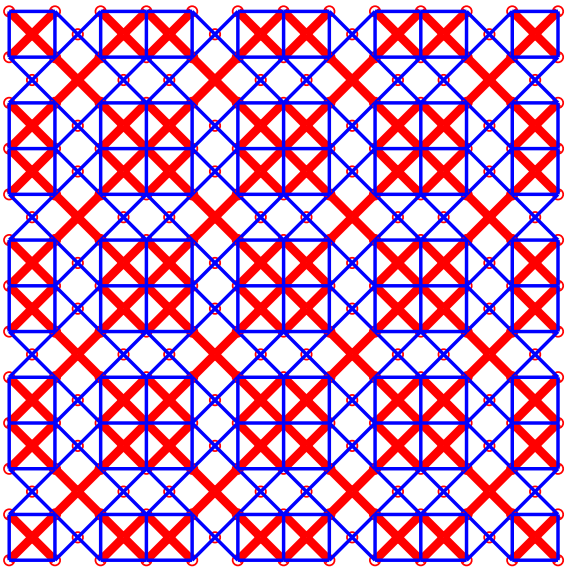

(b)

Figure 4.4: 2-dimensional 4×4 structures, where the bars are isolated in the top one and are connected in the bottom one. Bars and cables are shown in red and blue, respectively.

boundary conditions is imposed on our 4×4 lattices to incorporate the mirror symmetries along horizontal and vertical axis of a larger 8×8 lattice; therefore our results will be identical to that of an 8×8 lattice. Moreover, through a displacement control approach, all the nodes lying in the top surface of each lattice are subjected to a vertical displacements d. To mimic a quasi-static experiment, we impose d in increments of 0.001. Note that the height of each lattice in Fig. 4.4 is 24. At each increment, we solve for the equilibrium configuration. We remark here that due to existence of buckling and material nonlinearities -see the constitutive relation in 3.2.2-, as well as geometric nonlinearities, finding the equilibrium configuration for large deformations is not trivial. This is achieved by employing a combination of Newton-Raphson, conjugate gradient and steepest descent method.

The two sets of figures presented below are snapshots from the equilibrium configuration of each lattice at four different strain levels: 0, 4, 8 and 16 percent strains.

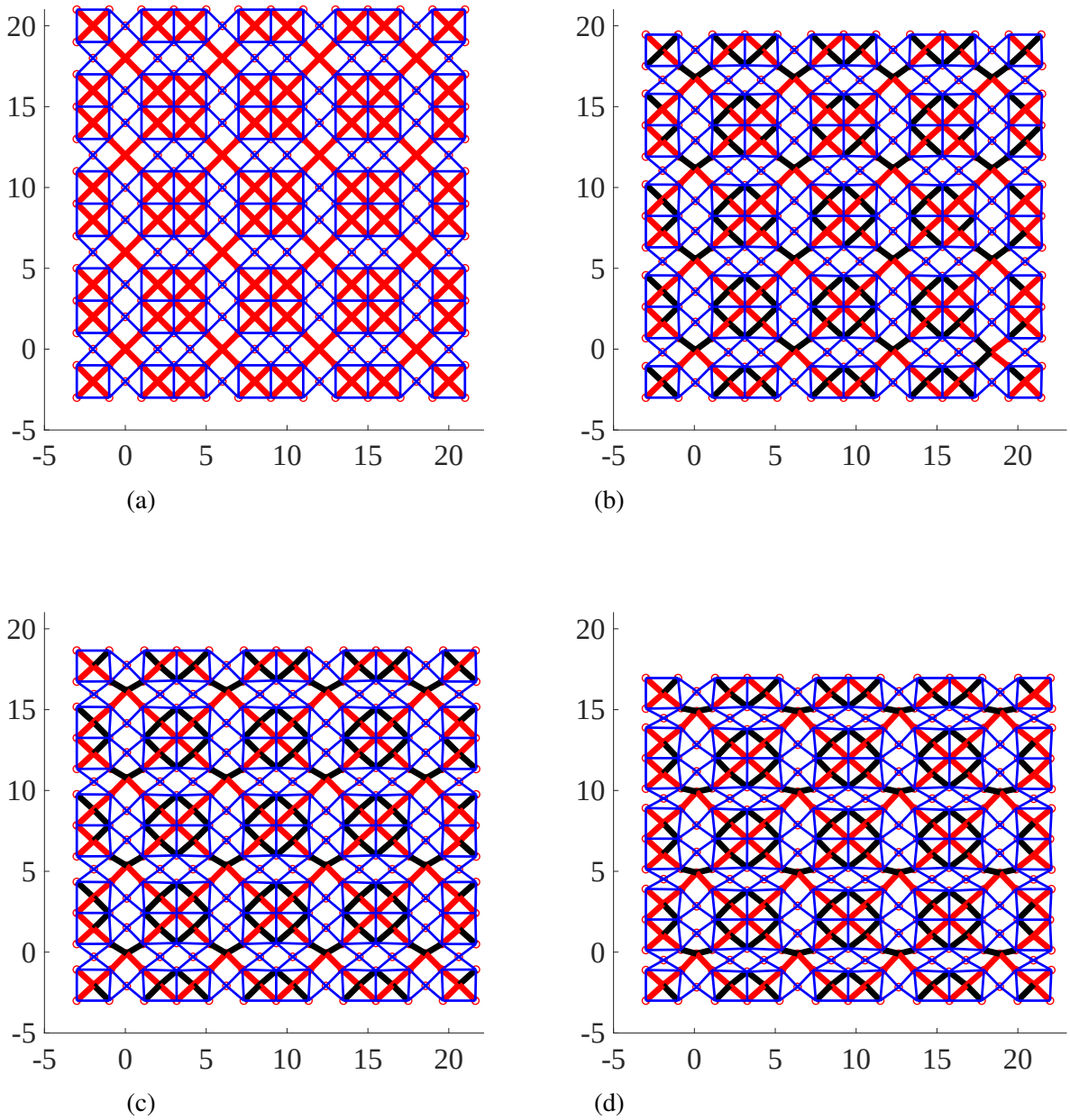

Figure 4.5: Snapshots from the equilibrium configuration of lattice with connected bars, at four different strain levels: (a) 0 % strain, (b) 4 % strain, (c) 8 % strain and (d) 16 % strain. Cables are shown in blue, while the bars in pre and post buckling states are shown in red and blue, respectively.

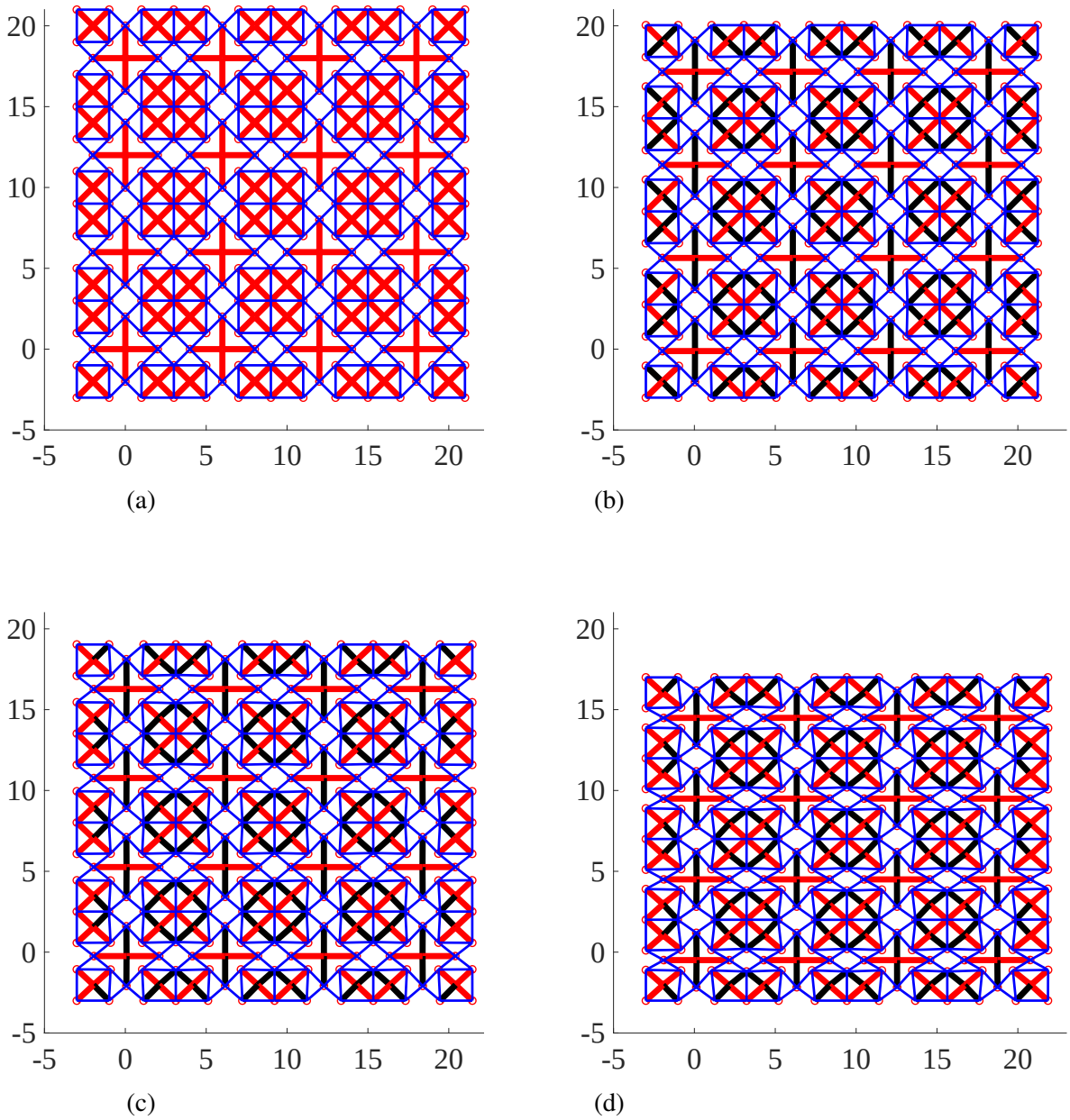

Figure 4.6: Snapshots from the equilibrium configuration of lattice with isolated bars, at four different strain levels: (a) 0 % strain, (b) 4 % strain, (c) 8 % strain and (d) 16 % strain. Cables are shown in blue, while the bars before and after buckling are shown in red and blue, respectively.

To get a better understanding of the mechanical response of the two lattices, particularly in comparison to each other, we look into the strain energy and forces at each step of deformation. We note that force in each step is obtained as the sum of all the vertical forces of all the nodes lying in the top surface.

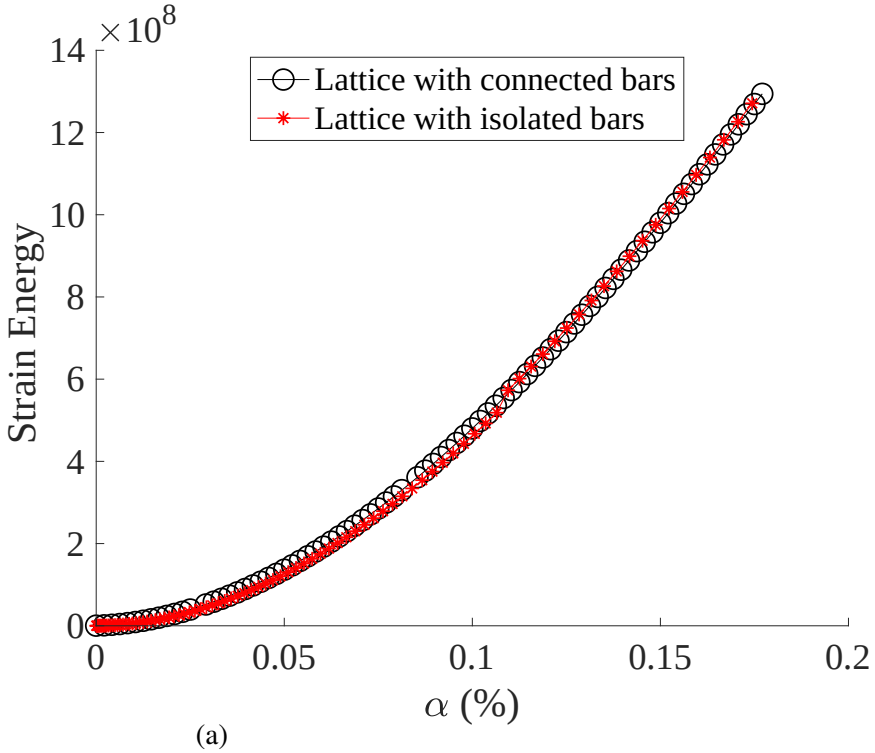

(a)

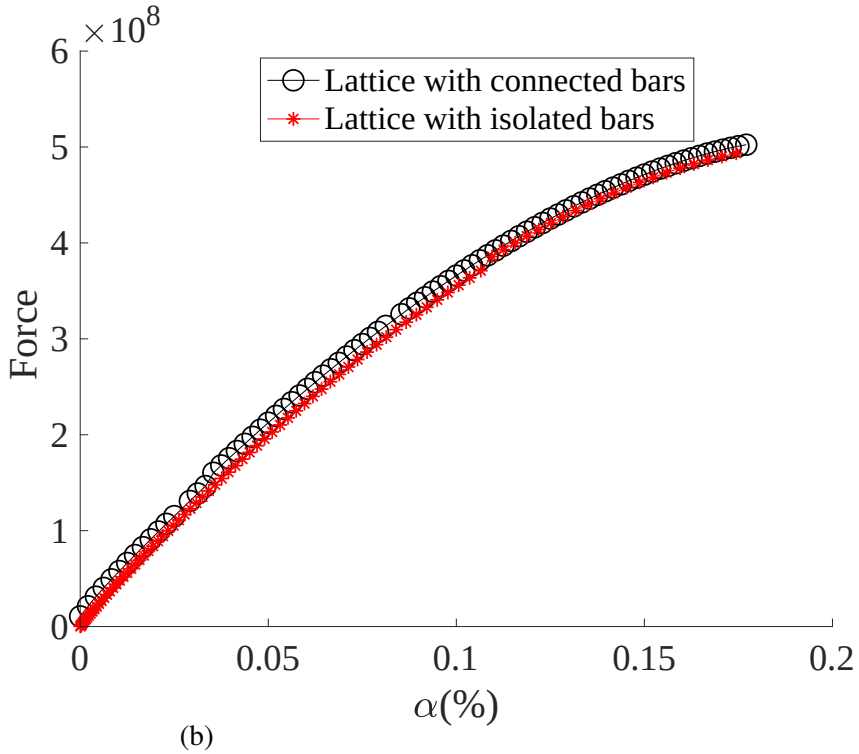

(b)

Figure 4.7: Comparing strain energy and force of the two lattices with connected and isolated bars, during the compression test. The horizontal axis in both figures demonstrate strain, α, while the vertical axis represents (a) strain energy, (b) force.

As it can be seen in Fig. 4.7, for a vast regime of deformations, the quasistatic behav-

ior in both lattices is identical. In other words, based on our results, changing the 'lattice topology' will not affect the force displacement response. We then pose the following questions: How the local instabilities -buckling of individual bars- affect the global instability? Do both lattices exhibit similar responses at the onset of their respective instability? For each case, how fast a local instability propagates in the domain? We devote the remainder of this section to answer these questions.

Effect of local instabilities in the global stiffness

As it was shown in the previous figures, after a certain amount of deformation, local instabilities emerge -a subset of bars buckle- in the domain of each lattice. We aim to characterize the onset of local instabilities in each system. To this end, we perform an eigenvalue analysis on the global stiffness matrix corresponding to each lattice. Note that the eigenvalues are always real, due to the symmetric nature of the global stiffness matrix. We then identify the minimum eigenvalue, denoting it as γ. Figure below illustrates the value of γ at each step of compressive deformation, denoted by d, for both of the lattices. To make the comparison of the γ's in both lattices more simple and tractable, the logarithm of γ is plotted with respect to d.

Evidently, as shown in Fig 4.8, unlike the force-displacement behavior, the lattices exhibit very distinct results. A negative eigenvalue is observed in the lattice with connected bars once it is subjected to a relatively small values of compression. Yet, the lattice with isolated bars never exhibits a negative eigenvalue, even for deformations more than $d = 2$, which mounts to more than 10% strain.

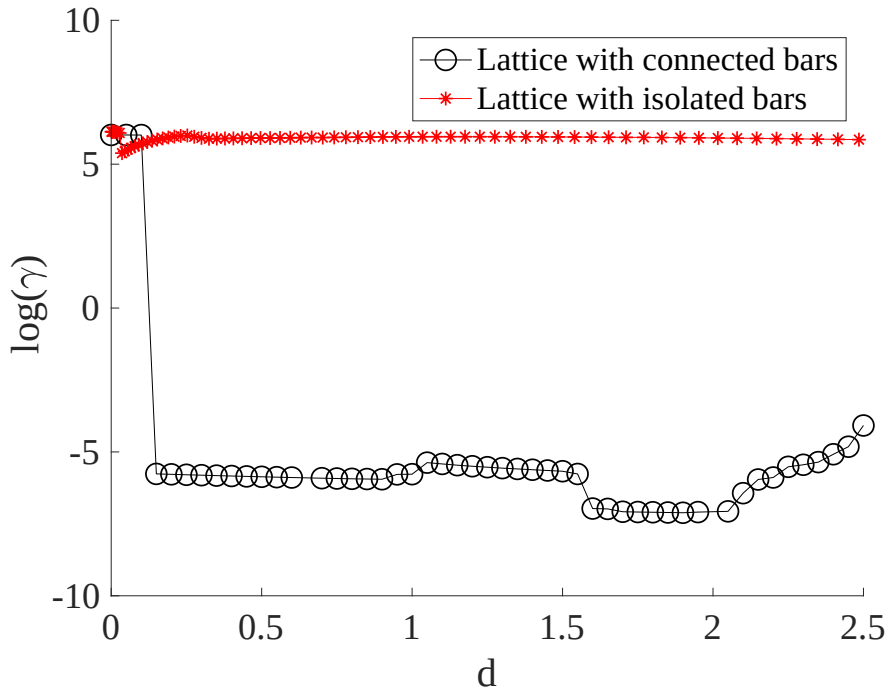

Figure 4.8: The horizontal and vertical axis show values of deformation d and minimum eigenvalue of the corresponding stiffness matrix, respectively.

To shed more light on this, we aim to identify the deformation that corresponds to the first observation of local instabilities in each lattice. To this end, we pursue a bisection approach, and characterize the value of d that leads to the first emergence of a local instability in each lattice, as shown in the figure below.

From this analysis, we observe that in the lattice with connected bars, the first observation of buckling Fig. 4.9b leads to buckling of two bars; and this is coincident with the first exhibition of a negative eigenvalue in the global stiffness. In other words, a local buckling is simultaneously manifested in the global behavior. Yet, in the lattice with isolated bars, despite buckling of 32 bars in the first emergence of a buckling -in a delocalized pattern-, the global stiffness never exhibits a negative eigenvalue. In fact, as seen in Fig 4.7, the number of buckled bars increases to even more than 32 bars in the large values of deformation, but it does not lead to a negative eigenvalue in the global stiffness matrix associated to the lattice with isolated bars.

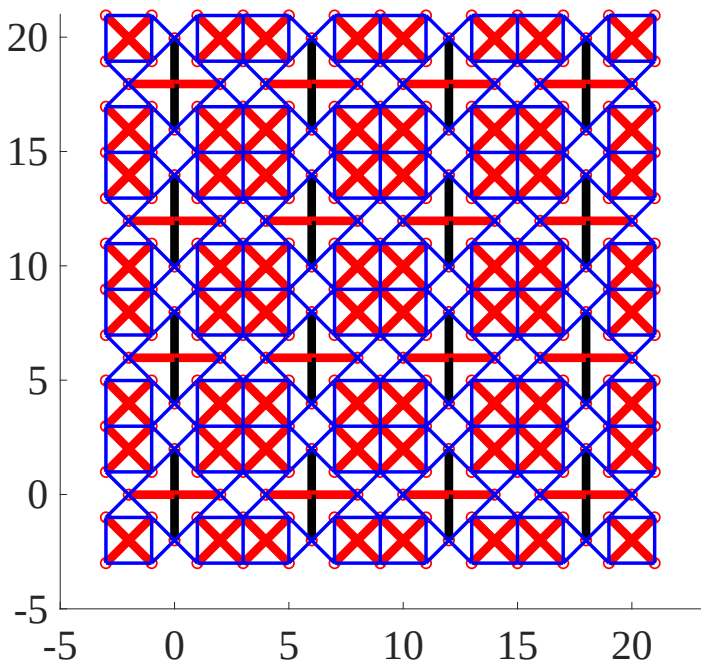

(a)

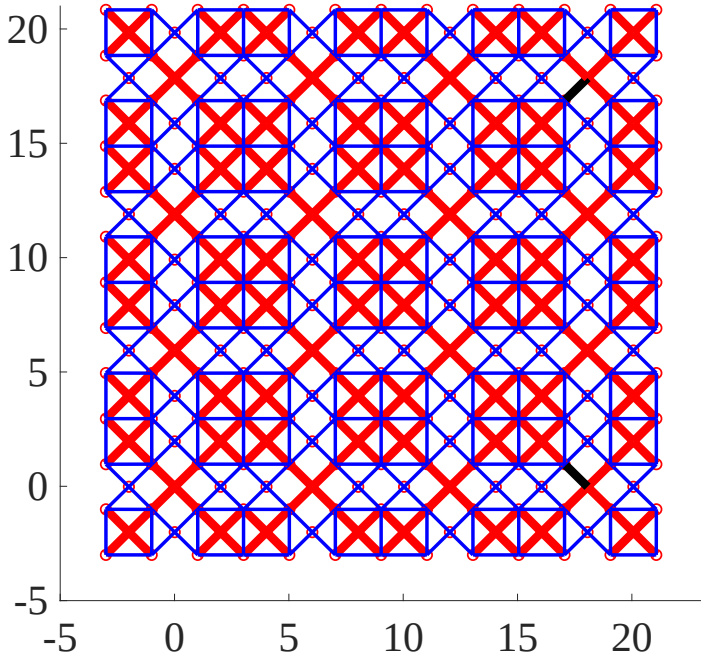

(b)

Figure 4.9: First observation of buckling of bars in: (a) lattice with isolated bars, and (b) lattice with connected bars. Cables are shown in blue, while the bars before and after buckling are shown in red and blue, respectively.

So far, we observed that in the case of the lattice with connected bars, the emergence of a local instability is instantaneously reflected in the global behavior; and a change in the topology of the lattice, so that the bars are disconnected, prevents this reflection in the global behavior. We now aim to investigate the last question posed in the previous subsection, looking into how fast a local instability propagates in the domain of each lattice. To this end, we look into the post-buckling response of each lattice. Starting from the first emergence of a local instability, we increase the compressive deformation very slowly, through increments that are two orders of magnitude smaller than initial steps -as discussed in the previous subsection-. At each step, we measure the number of bars that are buckled. The results of this calculation is presented in the Fig. 4.10.

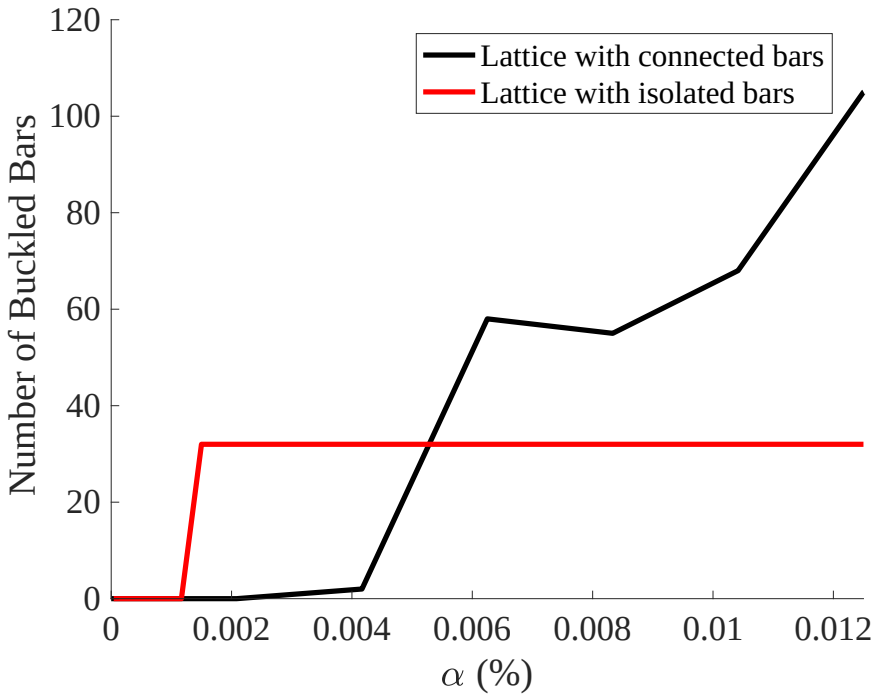

Figure 4.10: The horizontal and vertical axis respectively show the values of strain α and the number of buckled bars in each step of deformation for the corresponding lattice.

We observe that the number of buckled members in the lattice with connected bars mounts very rapidly from two bars -emergence of a local instability- to more than a hundred bars. Since we have 320 bars in total in each lattice, this lattice quickly travels from the

state with 0.006% of buckled bars to a state with 35% of buckled bars. On the other hand, in the lattice with isolated bars, local instabilities are trapped for a relatively large regime of deformations, thus the number of buckled bars remains constant at 32 buckled bars.

4.2.4 Summary and conclusion

In summary, we introduced two new designs for two-dimensional tensegrity systems, with very similar geometries but distinct lattice connectivity. After reviewing the theory for prestress stability, we examined and verified that our designs are prestress stable. We then preformed a compression test on both lattices, comparing the mechanical responses between them. By comparing the energies and forces in each lattice at every step of deformation, we demonstrated that both lattices exhibit an almost identical mechanical response. Yet, we showed that the eigenvalues, and consequently the eigenvectors, are very distinct; the lattice with isolated bars never exhibits a negative eigenvalue, while the lattice with connected bars results in a negative eigenvalue after a relatively small amount of deformation. We investigated this behavior by looking at the onset of buckling in each lattice. We illustrated that, in the lattice with connected bars, the first observation of buckling of bars is coincident with the first exhibition of a negative eigenvalue of the corresponding global stiffness tensor. In the lattice with isolated bars, in spite of a delocalized pattern of buckled bars, a negative eigenvalue is never observed. This strongly suggests that by only perturbing the topology of the lattice, where the lattice is transformed from a state with connected bars to a configuration with isolated bars, one can isolate the local instabilities and prevent their manifestation in the global scale. We also showed that the number of buckled bars rapidly mounts to more than 30% in the lattice with connected bars, while remaining constant, for a remarkable regime of deformations, in the other lattice. Our results lay a preliminary foundation for a more deep research on the effect of lattice topology on the mechanical response of lattices.

CHAPTER 5
CONCLUSIONS, CURRENT WORK AND FUTURE DIRECTIONS

5.1 Summary and conclusion

This thesis was devoted to certain key aspects of mechanics of nonlinear lattices, particularly focusing on instabilities and emergence of localized solutions, as well as material symmetry phase transitions. We explored these phenomena in single crystal metals and tensegrity lattices, as primary examples of natural and artificial lattice-based solids. Even though we have focused on certain types of lattices, in both materials and metamaterials, we emphasize that the incorporated tools are general and could be applied to other periodic lattices.

We have first looked into the instabilities in single crystal metals, modeled using EAM potentials, subjected to a combined dilation and shear deformation. This specific type of deformation is imposed to examine the Schmid assumption at the onset of plasticity in Iron (Fe), Nickel (Ni), Silver(Ag) and Copper (Cu). In addition, we have investigated the type of instabilities for a large regime of deformations, using both phonon stability and elastic analysis. For the latter scenario, we have incorporated a homogenization approach.

We have also studied pre-stretch induced material symmetry phase transitions in tensegrity-based metamaterials. We have devised a 6-dimensional space of pre-stretches, created by identifying six subsets of cables as families with identical pre-stretch. We have employed a homogenization scheme to obtain the first elasticity tensor. For a given pre-stretch scenario, to obtain the material symmetry, we have examined the eigenspaces of the effective elasticity tensor, corresponding to the equilibrium configuration of the pre-stretched lattice. We have then constructed a constrained optimization framework to study the material symmetries of an infinite lattice, where periodic boundary conditions are imposed as constraints.

Finally, we have studied emergence of localized deformation in 2-dimensional tensegrities. After creating novel designs of 2-dimensional lattices, we have investigated the effect of having isolated compression members on the corresponding mechanical properties. To this end, we have compared the quasi-static behavior of two lattices, with very similar geometries, differing only in the connectivity of bars -as compression members-.

5.1.1 Contributions

Here is a summary of contributions to the field, as a result of the current thesis:

- Using both elastic and phonon stability analysis, we have characterized the onset of instability in four single crystal metals, Fe, Ni, Ag and Cu , subjected to a combined dilation and shear deformation.

- We have shown that short wavelength instabilities are abundant in single crystals, undermining a wide spread assumption that instabilities in single crystal metals are of long wavelength. Thus, we have disqualified elastic stability analysis as the method of choice for studying instabilities in materials.

- We have shown the existence of shear-normal coupling at the onset of instability in single crystal metals, providing a more rigorous proof for existence of non-Schmid behavior at the onset of plasticity in single crystal metals.

- Regarding tensegrity-based metamaterials, we have characterized material symmetry phase transitions, induced by varying pre-stretches in the cables, from *cubic* to *tetragonal*, *cubic* to *orthotropic* and *orthotropic* to *tetragonal* and vice-versas.

- We have provided an example, demonstrating that imposing periodic boundary conditions for modeling a very large lattice, but finite, can lead to inaccurate results.

- We have shown the existence of a significant discrepancy between material symmetries of a finite and infinite tensegrity lattice.

- We have presented novel designs of 2-dimensional tensegrities. We have also provided preliminary evidence that, if compression members are isolated from each other, reflection of a localized instability on the global behavior becomes an unlikely event.

5.2 Current work and future directions

There are several interesting research avenues, in multiple fronts, that could be pursued in the future. Some of the key issues that could shed more light on the topics related to this thesis are:

- Investigating the mathematical conditions, such as variational inequalities, that would allow for predicting the emergence of short or long wavelength instabilities [1].

- Characterizing the effect of temperature on the onset of instabilities in single crystal metals.

- Investigating the effect of material symmetry phase transitions on dynamic properties of the corresponding metamaterial.

- Investigating the effect of imposing periodic boundary conditions on high frequency results of lattices that are subjected to non-affine pre-stretches.

- Investigating and understanding the effect of lattice connectivity on the global behavior of the corresponding lattice.

- Investigating and understanding the criteria for emergence of localized deformation.

Appendices

APPENDIX A

NOTIONS OF CONVEXITY IN 3D ELASTICITY

Rank-one convexity

W is *rank-one convex* if the map $t \to W(F + ta \otimes N)$ is convext for each $F \in M^{3\times3}$ and $a \in \mathbb{R}^3$, $N \in \mathbb{R}^3$. This is equivalent to $W(\lambda F + (1-\lambda)G) \leq \lambda W(F) + (1-\lambda)W(G)$ if $F, G \in M^{3\times3}$ with $F - G = a \otimes N$ and $\lambda \in (0, 1)$.

If $W \in C^1(M^{3\times3}_+)$ then W is rank-one convex if and only if $t \to DW(F+ta\otimes N).a\otimes N$ is non decreasing. The linear map

$$y(x) = (F + ta \otimes N)x = Fx + ta(x.N) \tag{A.1}$$

represents a shear relative to Fx parallel to a plane Π with normal N in the reference configuration, in the direction a. The corresponding stress vector across the plane Π is

$$t_R = DW(F + ta \otimes N)N, \tag{A.2}$$

and so rank-one convexity says that the component $t_R.a$ in the direction if the shear is monotone in the magnitude of the shear. If $W \in C^2(M^{3\times3}_+$ then W is rank-one convex if and only if

$$\frac{d^2}{dt^2}W(F + ta \otimes N)|_{t=0} \geq 0, \;\; F \in M^{3\times3}_+, a, N \in \mathbb{R}^3. \tag{A.3}$$

This is equivalent to:

$$D^2W(F)(a \otimes N, a \otimes N) = \frac{\partial^2 W(F)}{\partial F_i k \partial F_j l} a_i N_k a_j N_l \geq 0, \tag{A.4}$$

which is known as Legendre-Hadamard condition. A stronger version, which is called

strong ellipticity, is as the following:

$$D^2W(F)(a \otimes N, a \otimes N) = \frac{\partial^2 W(F)}{\partial F_i k \partial F_j l} a_i N_k a_j N_l \geq \mu |a|^2 |N|^2, \tag{A.5}$$

for all $F, a,$ and N and some constant $\mu > 0$.

One consequence of the above condition is that the wave speed in the equations of elastodynamics linearized around a uniform state $y = Fx$ is real. This is seen by first linearization

$$\rho \ddot{u}_i = \frac{\partial^2 W(F)}{\partial F_i k \partial F_j l} u_{j,kl}, \tag{A.6}$$

and plane wave

$$u = af(x.N - ct), \tag{A.7}$$

is a solution if

$$C(F)a = c^2 \rho a, \;\; C_{ij} = \frac{\partial^2 W(F)}{\partial F_i k \partial F_j l} N_k N_l. \tag{A.8}$$

Strong ellipticity implies $C(F) > 0$, so $c^2 > 0$ leading to a real c.

Quasiconvexity

Quasiconvexity, first introduced by [142] in 1952, is defined as below: Let $W : M^{m \times n} \rightarrow [0, \infty]$ be Borel measurable. Let $\Omega \subset \mathbb{R}^m$ be an open bounded set whose boundary $\partial\Omega$ has zero Lebesgue measure. W is said to be *quasiconvex* at $F \in M^{m \times n}$ if the inequality

$$\int_\Omega W(F + D\phi(x))dx \geq \int_\Omega W(F)dx \;\; \forall \phi \in W_0^{1,\infty}(\Omega; \mathbb{R}^m), \tag{A.9}$$

holds and is quasiconvex if it is quasiconvex at every $F \in M_+^{m \times n}$.

If we set $m = n = 3$, as hinted before, we see that W is quasiconvex if for any

$F \in M^{3\times 3}_{+}$ the pure displacement problem to minimize

$$I(y) = \int_{\Omega} W(Dy(x))dx \tag{A.10}$$

subject to the linear boundary condition

$$y(x) = Fx, \;\; x \in \partial\Omega, \tag{A.11}$$

has $y(x) = Fx$ as a minimizer.

Theorem. If W is continuous and quasiconvex then W is rank-one convex.

Proof: We want to prove that

$$\begin{aligned} &W(F) \leq \lambda W(F - (1-\lambda)a \otimes N) + (1-\lambda)W(F + \lambda a \otimes N) \\ &\forall F \in M^{m\times n}, a \in \mathbb{R}^m, N \in \mathbb{R}^m, \lambda \in (0,1). \end{aligned} \tag{A.12}$$

Without loss of generality, we assume that $N = e_1$. Let us denote $D = (-(1-\lambda), \lambda) \times (-\rho, \rho)^{n-1}$ and let $D_j^{\pm}$ be the pyramid that is the convex hull of the origin and the face of D with normal $\pm e_j$. Let $\phi \in W_0^{1,\infty}(D; \mathbb{R}^m)$ be affine in each $D_j^{\pm}$ with $\phi(0) = \lambda(1-\lambda)a$. The values of $D\phi$ are shown in the following figure. By quasiconvexity

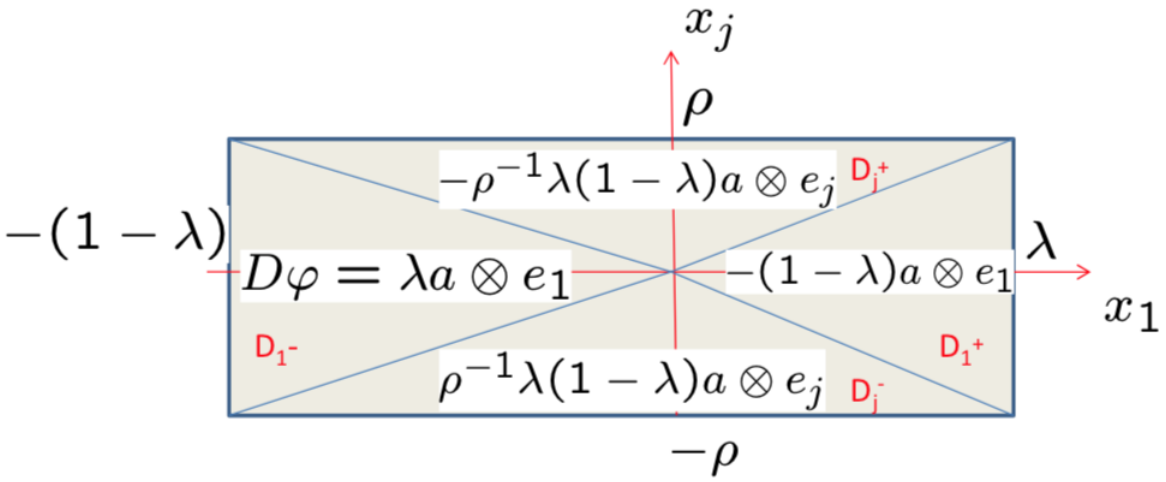

Figure A.1: Borrowed from notes of John Ball on mathematical foundations of elasticity.

$$(2\rho)^{n-1}W(F) \leq \frac{(2\rho)^{n-1}\lambda}{n}W(F-(1-\lambda)a\otimes e_1) + \frac{(2\rho)^{n-1}(1-\lambda)}{n}W(F+\lambda\otimes e_1)$$
$$\sum_{j=2}^{n}\frac{(2\rho)^{n-1}}{2n}[W(F+\rho^{-1}\lambda(1-\lambda)a\otimes e_j)+W(F-\rho^{-1}\lambda(1-\lambda)a\otimes e_j)]. \tag{A.13}$$

Dividing by $(2\rho)^{n-1}$, taking the limit as $\rho \to 0_+$ and by the continuity of W, we obtain

$$W(F) \leq \lambda W(F-(1-\lambda)a\otimes e_1) + (1-\lambda)W(F+\lambda a\otimes e_1), \tag{A.14}$$

which concludes the proof.

We remark here that continuity is crucial, otherwise if we have nonzero a, N such that:

$$W(0) = W(a\otimes N) = 0,\ \ W(F) = \infty \text{otherwise.} \tag{A.15}$$

Then W is clearly not rank-one convex, but it is quasiconvex, since given $F \neq 0$, $a \otimes N$ there is no $\phi \in W_0^{1,\infty}$ with $F + D\phi \in 0, a \otimes N$.

A corollary of the above theorem is that if $m = 1$ or $n = 1$ then a continuous $W : M^{m\times n} \to [0,\infty]$ is quasiconvex if and only if it is convex. There are several theorems showing that quasiconvexity of W will result on the total elastic energy to be sequentially weakly lower semicontinuous, which we refer the interested reader to the notes of professor John Ball.

Polyconvexity

The last measure of convexity that is of interest to us is polyconvexity. W is *polyconvex* if there exists a convex function $g : \mathbb{R}^d(m,n) \to (-\infty,\infty]$ such that $W(F) = g(\mathbf{J}(F))$ for all $F \in M^{m\times n}$. If $m = n = 3$, then we have $W(F) = g(F, \text{cof}F, \det F)$ with g convex. **Theorem**. If W is polyconvex with g lower semicontinuous, then W is quasiconvex.

Proof: If we write

$$\fint_\Omega f dx = \frac{1}{\text{meas}\Omega}\int_\Omega f dx, \tag{A.16}$$

then by using Jensen's inequaility, we can write the following:

$$\begin{aligned}\fint_\Omega W(F+D\phi(x))dx &= \fint_\Omega g(\mathbf{J}(F+D\phi(x)))dx \\ &\quad g\Big(\fint_\Omega \mathbf{J}(F+D\phi)dx\Big) \\ &\quad g(\mathbf{J}(F)) = W(F).\end{aligned} \tag{A.17}$$

Thus we have shown that if

W convex $\rightarrow$ W polyconvex $\rightarrow$ W quasiconvex $\rightarrow$ W rank-one convex.

The reverse are all false, if $m > 1, n > 1$, except it is not known whether W rank-one convex $\rightarrow$ W quasiconvex when $n \geq m = 2$. With this new definition one can show the existence of the minimizers for mixed boundary value problems if we assume W is polyconvex and satisfies some additional conditions, similar to the 1-dimensional case. We will only state the theorem here.

Theorem. Suppose W satisfies the following conditions:

- $W(x,y) \rightarrow \infty$ as $p \rightarrow 0_+$.
- $W(F) \geq c_0(|F|^2 + |\text{cof}F|^{3/2}) - c_1$ for all $F \in M^{3\times 3}$, where $c_0 > 0$.
- W is polyconvex.

Assume that there exists some y in $\mathcal{A} = y \in W^{1,1}(\Omega;\mathbb{R}^3) : y|_{\partial\Omega_1} = \bar{y}$ with $I(y) < \infty$, where $\mathcal{H}^2(\partial\Omega_1) > 0$ and $\bar{y} : \partial\Omega_1 \rightarrow \mathbb{R}^3$ is measurable. Then there exists a global minimizer y^* of I in $\mathcal{A}$.

APPENDIX B

EQUIVALENCE OF ELASTIC STABILITY AND PHONON STABILITY ANALYSIS IN THE LONG WAVELENGTH LIMIT

In this section, we show that in the long wavelength limit, $\kappa \to 0$, phonon and elastic stability analysis are equivalent. We believe demonstrating the steps for a 1-dimensional chain sheds light on the details of the formulation, as well as is easily extendable to a general case, which leads to the general proof. Let us then assume a 1-dimensional infinite chain, as shown in Fig. B.1, where each atom interacts up to its second nearest neighbor. As the fundamental assumption of our homogenization scheme, we apply an affine deformation field through a constant F, so the deformed configuration of atoms would be $x = FX$.

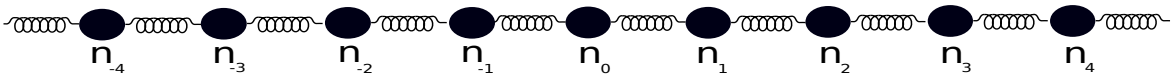

Figure B.1: 1-dimensional monoatomic chain. The distance between each pair of atoms is denoted by a.

The dynamical matrix, corresponding to phonon stability analysis, is as the following:

$$S(\kappa) = \sum_{p=-4}^{p=4} \frac{\partial^2 E_T}{\partial x_0 \partial x_p} \exp\left(-i\kappa x_p\right), \tag{B.1}$$

where E_T is the total energy of the lattice. We remark here that even though the unit cell contains atoms n_{-2} to n_2, we have second nearest neighbor interactions, so the sum in (B.1)

ranges from $p = -4$ to $p = 4$. If we expand (B.1), we will get:

$$\begin{aligned}
S(\kappa) =& \frac{\partial^2 E_0}{\partial x_2 \partial x_{-2}} e^{-i\kappa x_{-4}} + (\frac{\partial^2 E_0}{\partial x_1 \partial x_{-2}} + \frac{\partial^2 E_0}{\partial x_2 \partial x_{-1}}) e^{-i\kappa x_{-3}} \\
&+ (\frac{\partial^2 E_0}{\partial x_0 \partial x_2} + \frac{\partial^2 E_0}{\partial x_1 \partial x_{-1}} + \frac{\partial^2 E_0}{\partial x_0 \partial x_{-2}}) e^{-i\kappa x_{-2}} \\
&+ (\frac{\partial^2 E_0}{\partial x_1 \partial x_2} + \frac{\partial^2 E_0}{\partial x_0 \partial x_1} + \frac{\partial^2 E_0}{\partial x_0 \partial x_{-1}} + \frac{\partial^2 E_0}{\partial x_{-1} \partial x_{-2}}) e^{-i\kappa x_{-1}} \\
&+ (\frac{\partial^2 E_0}{\partial x_{-2}^2} + \frac{\partial^2 E_0}{\partial x_{-1}^2} + \frac{\partial^2 E_0}{\partial x_0^2} + \frac{\partial^2 E_0}{\partial x_1^2} + \frac{\partial^2 E_0}{\partial x_2^2}) e^{-i\kappa x_0} \\
&+ (\frac{\partial^2 E_0}{\partial x_1 \partial x_2} + \frac{\partial^2 E_0}{\partial x_0 \partial x_1} + \frac{\partial^2 E_0}{\partial x_0 \partial x_{-1}} + \frac{\partial^2 E_0}{\partial x_{-1} \partial x_{-2}}) e^{-i\kappa x_1} \\
&+ (\frac{\partial^2 E_0}{\partial x_0 \partial x_2} + \frac{\partial^2 E_0}{\partial x_1 \partial x_{-1}} + \frac{\partial^2 E_0}{\partial x_0 \partial x_{-2}}) e^{-i\kappa x_2} \\
&+ (\frac{\partial^2 E_0}{\partial x_1 \partial x_{-2}} + \frac{\partial^2 E_0}{\partial x_2 \partial x_{-1}}) e^{-i\kappa x_3} + \frac{\partial^2 E_0}{\partial x_2 \partial x_{-2}} e^{-i\kappa x_4}
\end{aligned} \tag{B.2}$$

we want to evaluate $S(\kappa)$ near $\kappa = 0$ -long wavelength-; thus we linearize around $\kappa = 0$. The zeroth and first order terms vanish due to equilibrium and inversion symmetry -sum of each row of dynamical matrix vanishes-, and we are left with $\frac{\partial^2 S}{\partial \kappa^2}$. Without loss of generality, we assume that $F = 1$ and $X = 0$.

$$
\begin{aligned}
S(\kappa) =& \frac{\partial^2 E_0}{\partial x_2 \partial x_{-2}} 4X_{-2}^2 e^{-i\kappa x_{-4}} \\
&+ (\frac{\partial^2 E_0}{\partial x_1 \partial x_{-2}} + \frac{\partial^2 E_0}{\partial x_2 \partial x_{-1}})(X_{-2}^2 + X_{-1}^2 + 2X_{-2}X_{-1}) e^{-i\kappa x_{-3}} \\
&+ (\frac{\partial^2 E_0}{\partial x_0 \partial x_2} + \frac{\partial^2 E_0}{\partial x_1 \partial x_{-1}} + \frac{\partial^2 E_0}{\partial x_0 \partial x_{-2}}) X_{-2}^2 e^{-i\kappa x_{-2}} \\
&+ (\frac{\partial^2 E_0}{\partial x_1 \partial x_2} + \frac{\partial^2 E_0}{\partial x_0 \partial x_1} + \frac{\partial^2 E_0}{\partial x_0 \partial x_{-1}} + \frac{\partial^2 E_0}{\partial x_{-1} \partial x_{-2}}) X_{-1}^2 e^{-i\kappa x_{-1}} \\
&+ (\frac{\partial^2 E_0}{\partial x_1 \partial x_2} + \frac{\partial^2 E_0}{\partial x_0 \partial x_1} + \frac{\partial^2 E_0}{\partial x_0 \partial x_{-1}} + \frac{\partial^2 E_0}{\partial x_{-1} \partial x_{-2}}) X_1^2 e^{-i\kappa x_1} \\
&+ (\frac{\partial^2 E_0}{\partial x_0 \partial x_2} + \frac{\partial^2 E_0}{\partial x_1 \partial x_{-1}} + \frac{\partial^2 E_0}{\partial x_0 \partial x_{-2}}) X_2^2 e^{-i\kappa x_2} \\
&+ (\frac{\partial^2 E_0}{\partial x_1 \partial x_{-2}} + \frac{\partial^2 E_0}{\partial x_2 \partial x_{-1}})(X_2^2 + X_1^2 + 2X_2X_1) e^{-i\kappa x_3} \\
&+ \frac{\partial^2 E_0}{\partial x_2 \partial x_{-2}} 4X_2^2 e^{-i\kappa x_4},
\end{aligned}
\tag{B.3}
$$

where we have used the periodicity to write $X_{-4} = X_{-2} + X-2$ and $X_{-3} = X_{-2} + X-1$.

In the context of elastic stability, we are looking at

$$
\frac{\partial^2 E_0}{\partial F \partial F} = \sum_{q=-2}^{2} \sum_{p=-2}^{2} \frac{\partial^2 E_0}{\partial x_p \partial x_q} X_p X_q. \tag{B.4}
$$

If we expand the above, we get the following:

$$
\begin{aligned}
\frac{\partial^2 E_0}{\partial F \partial F} =& \frac{\partial^2 E_0}{\partial x_{-2}^2} X_{-2}^2 + \frac{\partial^2 E_0}{\partial x_{-1}^2} X_{-1}^2 + \frac{\partial^2 E_0}{\partial x_1^2} X_1^2 + \frac{\partial^2 E_0}{\partial x_2^2} X_2^2 \\
&+ 2\frac{\partial^2 E_0}{\partial x_{-2} \partial x_{-1}} X_{-2}X_{-1} + 2\frac{\partial^2 E_0}{\partial x_{-2} \partial x_1} X_{-2}X_1 + 2\frac{\partial^2 E_0}{\partial x_{-2} \partial x_2} X_{-2}X_2 \\
&+ 2\frac{\partial^2 E_0}{\partial x_{-1} \partial x_1} X_{-1}X_1 + 2\frac{\partial^2 E_0}{\partial x_{-1} \partial x_2} X_{-1}X_2 + 2\frac{\partial^2 E_0}{\partial x_1 \partial x_2} X_1X_2.
\end{aligned}
\tag{B.5}
$$

The last step to see that (B.5) and (B.3) are equivalent, is to incorporate translational

symmetry (B.5); which is the following:

$$\sum_{q=-2}^{2} \frac{\partial^2 E_0}{\partial x_p \partial x_q} = 0, \ \forall \ p \tag{B.6}$$

We remark here that a very similar approach holds in the case of 3-dimensional lattice.

APPENDIX C

DERIVATIVES OF EAM POTENTIAL

In this section, we present the Embedded-Atom-Method (EAM) potential form and its second derivative incorporated in the phonon stability analysis. Let us denote the atom sitting in position 'i' as $\mathbf{r_i} = r_i^1\mathbf{e_1} + r_i^2\mathbf{e_2} + r_i^3\mathbf{e_3}$. We also denote the distance between atoms 'i' and 'j' as $r_{ij} = |\mathbf{r_j} - \mathbf{r_i}|$. We have the total energy as:

$$E = \frac{1}{2}\sum_{ij} V(r_{ij}) - \sum_i f(\rho_i) = \frac{1}{2}\sum_{i=1}^{N}\sum_{j=1}^{N} V(r_{ij}) - \sum_{i=1}^{N}\sqrt{\sum_{j=1}^{N} A^2\phi(r_{ij})}, \tag{C.1}$$

where we have the pair potential term and the embedding term, as follows:

$$V(r_{ij}) = \begin{cases} V(r_{ij}) \ r_{ij} \leq c \\ \\ 0 \ r_{ij} > c \end{cases}, \qquad \phi(r_{ij}) = \begin{cases} \phi(r_{ij}) \ r_{ij} \leq d \\ \\ 0 \ r_{ij} > d \end{cases} \tag{C.2}$$

Taking the first derivative of energy w.r.t r_i^p where $p = 1, 2, 3$ will results in the force acting on particle i in the p direcation, as f_i^p:

$$\frac{\partial E}{\partial r_i^p} = \frac{1}{2}\sum_{j\in B(r_i,c)} \frac{\partial V(r_{ij})}{\partial r_i^p} - \sum_{k\in B(r_i,d)} \frac{\partial f_k}{\partial r_i^p} \tag{C.3}$$

$$\tag{C.4}$$

$B(r_i, c)$ and $B(r_i, d)$ represent a ball centered at atom r_i wth radius c, d being the cutoff of the pair potential and embedding potential. The second derivatives will be as the following:

$$\frac{\partial^2 E}{\partial r_j^q \partial r_i^p} = \frac{1}{2}\frac{\partial^2 V(r_{ij})}{\partial r_j^q \partial r_i^p} - \sum_{k \in B(r_i,d) \cap B(r_j,d)} \frac{\partial}{\partial r_j^q}\left(\frac{\partial f_k}{\partial r_i^p}\right) \tag{C.5}$$

$$\frac{\partial^2 E}{\partial r_i^q \partial r_i^p} = \frac{1}{2}\sum_{j \in B(r_i,c)} \frac{\partial^2 V(r_{ij})}{\partial r_i^q \partial r_i^p} - \sum_{k \in B(r_i,d)} \frac{\partial}{\partial r_i^q}\left(\frac{\partial f_k}{\partial r_i^p}\right) \tag{C.6}$$

$$\tag{C.7}$$

The second derivatives for the equations above are computed as below:

$$\frac{\partial^2 V(r_{ij})}{\partial r_j^q \partial r_i^p} = -\frac{1}{r_{ij}}\frac{dV(r_{ij})}{dr_{ij}}\delta_{pq} + \frac{r_{ij}^q r_{ij}^p}{r_{ij}^3}\frac{dV(r_{ij})}{dr_{ij}} - \frac{r_{ij}^q r_{ij}^p}{r_{ij}^2}\frac{d^2V(r_{ij})}{dr_{ij}^2} \tag{C.8}$$

$$\frac{\partial^2 V(r_{ij})}{\partial r_i^q \partial r_i^p} = \frac{1}{r_{ij}}\frac{dV(r_{ij})}{dr_{ij}}\delta_{pq} - \frac{r_{ij}^q r_{ij}^p}{r_{ij}^3}\frac{dV(r_{ij})}{dr_{ij}} + \frac{r_{ij}^q r_{ij}^p}{r_{ij}^2}\frac{d^2V(r_{ij})}{dr_{ij}^2} \tag{C.9}$$

$$\begin{aligned}\frac{\partial^2 f_i}{\partial r_i^q \partial r_i^p} =& \frac{A^2}{2\sqrt{\rho}_i}\sum_{m \in B(r_i,d)} \frac{1}{r_{im}}\frac{d\phi_{im}}{dr_{im}}\delta_{pq} - \frac{r_{im}^q r_{im}^p}{r_{im}^3}\frac{d\phi(r_{im})}{dr_{im}} + \frac{r_{im}^q r_{im}^p}{r_{im}^2}\frac{d^2\phi(r_{im})}{dr_{im}^2} \\ &- \frac{A^4}{4\rho_i^{3/2}}\sum_{m \in B(r_i,d)}\sum_{n \in B(r_i,d)} \frac{r_{im}^q r_{in}^p}{r_{im} r_{in}}\frac{d\phi_{in}}{dr_{in}}\frac{d\phi_{im}}{dr_{im}}\end{aligned} \tag{C.10}$$

$$\begin{aligned}\frac{\partial^2 f_i}{\partial r_j^q \partial r_i^p} =& \frac{A^2}{2\sqrt{\rho}_i}\Big(-\frac{1}{r_{ij}}\frac{d\phi_{ij}}{dr_{ij}}\delta_{pq} + \frac{r_{ij}^q r_{ij}^p}{r_{ij}^3}\frac{d\phi(r_{ij})}{dr_{ij}} - \frac{r_{ij}^q r_{ij}^p}{r_{ij}^2}\frac{d^2\phi(r_{ij})}{dr_{ij}^2}\Big) \\ &+ \frac{A^4}{4\rho_i^{3/2}}\frac{r_{ij}^p}{r_{ij}}\frac{d\phi_{ij}}{dr_{ij}}\sum_{m \in B(r_i,d)} \frac{r_{im}^q}{r_{im}}\frac{d\phi_{im}}{dr_{im}}\end{aligned} \tag{C.11}$$

$$\begin{aligned}\frac{\partial^2 f_k}{\partial r_i^q \partial r_i^p} =& \frac{A^2}{2\sqrt{\rho}_k}\Big(\frac{1}{r_{ki}}\frac{d\phi_{ki}}{dr_{ki}}\delta_{pq} - \frac{r_{ki}^q r_{ki}^p}{r_{ki}^3}\frac{d\phi(r_{ik})}{dr_{ik}} + \frac{r_{ki}^q r_{ki}^p}{r_{ki}^2}\frac{d^2\phi(r_{ki})}{dr_{ki}^2}\Big) \\ &- \frac{A^4}{4\rho_k^{3/2}}\frac{r_{ki}^q r_{ki}^p}{r_{ki}^2}\left(\frac{d\phi_{ki}}{dr_{ki}}\right)^2\end{aligned} \tag{C.12}$$

$$\frac{\partial^2 f_k}{\partial r_j^q \partial r_i^p} = -\frac{A^4}{4\rho_k^{3/2}}\frac{r_{kj}^q r_{ki}^p}{r_{ki} r_{kj}}\frac{d\phi_{ki}}{dr_{ki}}\frac{d\phi_{kj}}{dr_{kj}} \tag{C.13}$$

Using the previous relations, the dynamical matrix is constructd.

APPENDIX D

DERIVATIVES OF A SPRING POTENTIAL IN 3D

Here we present analytic expressions for derivatives of the energy of a single element, used for solving the nonlinear equations resulting from the constrained optimization problem. The strain energy associated to a spring connecting nodes 'i' and 'j' in 3D is

$$E = \frac{1}{2}k\left(|\mathbf{x}^i - \mathbf{x}^j| - L\right)^2, \tag{D.1}$$

where E, k, L are real numbers representing energy, spring stiffness and the length of unstretched spring, respectively; $\mathbf{x}_i$ and $\mathbf{x}_j$ are vectors in $\mathbb{R}^3$ associated to the current positions of nodes 'i' and 'j'. Next, we compute the first, second and third derivative as follows:

$$\frac{\partial E}{\partial x_p^i} = k\left(|\mathbf{x}^i - \mathbf{x}^j| - L\right)\frac{x_p^i - x_p^j}{|\mathbf{x}^i - \mathbf{x}^j|}, \tag{D.2a}$$

$$\frac{\partial^2 E}{\partial x_p^i \partial x_q^i} = k\left(|\mathbf{x}^i - \mathbf{x}^j| - L\right)\left(\frac{\delta_{pq}}{|\mathbf{x}^i - \mathbf{x}^j|}\right) + kL\frac{(x_p^i - x_p^j)(x_q^i - x_q^j)}{|\mathbf{x}^i - \mathbf{x}^j|^3}, \tag{D.2b}$$

$$\frac{\partial^3 E}{\partial x_p^i \partial x_q^i \partial x_r^i} = \frac{kL}{|\mathbf{x}^i - \mathbf{x}^j|^5}\Big(|\mathbf{x}^i - \mathbf{x}^j|^2(\delta_{qr}(x_p^i - x_p^j) + \delta_{pr}(x_q^i - x_q^j) + \delta_{pq}(x_r^i - x_r^j)) \tag{D.2c}$$

$$- 3(x_p^i - x_p^j)(x_q^i - x_q^j)(x_r^i - x_r^j)\Big). \tag{D.2d}$$

Similarly, derivatives with respect to $\mathbf{x}_j$ and cross derivatives are calculated, which might only differ by a sign from the above equations.

REFERENCES

[1] Alain Bensoussan, Jacques-Louis Lions, and George Papanicolaou. *Asymptotic analysis for periodic structures*. Vol. 374. American Mathematical Soc., 2011.

[2] Dennis M Kochmann and Katia Bertoldi. "Exploiting Microstructural Instabilities in Solids and Structures: From Metamaterials to Structural Transitions". In: *Applied Mechanics Reviews* 69.5 (2017), p. 050801.

[3] Ju Li et al. "Atomistic mechanisms governing elastic limit and incipient plasticity in crystals". In: *Nature* 418.6895 (2002), pp. 307–310.

[4] Ting Zhu et al. "Predictive modeling of nanoindentation-induced homogeneous dislocation nucleation in copper". In: *Journal of the Mechanics and Physics of Solids* 52.3 (2004), pp. 691–724.

[5] Xiaohui Liu et al. "Lattice dynamical finite-element method". In: *Acta Materialia* 58.2 (2010), pp. 510–523.

[6] Krystyn J Van Vliet et al. "Quantifying the early stages of plasticity through nanoscale experiments and simulations". In: *Physical Review B* 67.10 (2003), p. 104105.

[7] Ronald E Miller and David Rodney. "On the nonlocal nature of dislocation nucleation during nanoindentation". In: *Journal of the Mechanics and Physics of Solids* 56.4 (2008), pp. 1203–1223.

[8] TJ Delph et al. "A local instability criterion for solid-state defects". In: *Journal of the Mechanics and Physics of Solids* 57.1 (2009), pp. 67–75.

[9] Akanksha Garg and Craig E Maloney. "Mechanical Instabilities in Perfect Crystals: From Dislocation Nucleation to Bucklinglike Modes". In: *Journal of Applied Mechanics* 83.12 (2016), p. 121006.

[10] Akanksha Garg, Amit Acharya, and Craig E Maloney. "A study of conditions for dislocation nucleation in coarser-than-atomistic scale models". In: *Journal of the Mechanics and Physics of Solids* 75 (2015), pp. 76–92.

[11] Robert G Hutchinson and Norman A Fleck. "The structural performance of the periodic truss". In: *Journal of the Mechanics and Physics of Solids* 54.4 (2006), pp. 756–782.

[12] Johannes Tesse Bastiaan Overvelde, Sicong Shan, and Katia Bertoldi. "Compaction through buckling in 2D periodic, soft and porous structures: effect of pore shape". In: *Advanced Materials* 24.17 (2012), pp. 2337–2342.

[13] Jongmin Shim et al. "Buckling-induced encapsulation of structured elastic shells under pressure". In: *Proceedings of the National Academy of Sciences* 109.16 (2012), pp. 5978–5983.

[14] Raj Kumar Pal, Massimo Ruzzene, and Julian J Rimoli. "A continuum model for nonlinear lattices under large deformations". In: *International Journal of Solids and Structures* 96 (2016), pp. 300–319.

[15] Lucas R Meza, Satyajit Das, and Julia R Greer. "Strong, lightweight, and recoverable three-dimensional ceramic nanolattices". In: *Science* 345.6202 (2014), pp. 1322–1326.

[16] Lucas R Meza et al. "Resilient 3D hierarchical architected metamaterials". In: *Proceedings of the National Academy of Sciences* 112.37 (2015), pp. 11502–11507.

[17] Fatih Göncü, Stefan Luding, and Katia Bertoldi. "Exploiting pattern transformation to tune phononic band gaps in a two-dimensional granular crystal". In: *The Journal of the Acoustical Society of America* 131.6 (2012), EL475–EL480.

[18] Pai Wang et al. "Harnessing buckling to design tunable locally resonant acoustic metamaterials". In: *Physical review letters* 113.1 (2014), p. 014301.

[19] Stephan Rudykh and Mary C Boyce. "Transforming wave propagation in layered media via instability-induced interfacial wrinkling". In: *Physical review letters* 112.3 (2014), p. 034301.

[20] Nader Engheta and Richard W Ziolkowski. *Metamaterials: physics and engineering explorations*. John Wiley & Sons, 2006.

[21] Bastiaan Florijn, Corentin Coulais, and Martin van Hecke. "Programmable mechanical metamaterials". In: *Physical review letters* 113.17 (2014), p. 175503.

[22] Xiaoyu Zheng et al. "Ultralight, ultrastiff mechanical metamaterials". In: *Science* 344.6190 (2014), pp. 1373–1377.

[23] Jong Bum Lee et al. "A mechanical metamaterial made from a DNA hydrogel". In: *Nature Nanotechnology* 7.12 (2012), p. 816.

[24] Zhengyou Liu et al. "Locally resonant sonic materials". In: *Science* 289.5485 (2000), pp. 1734–1736.

[25] M Ruzzene and F Scarpa. “Directional and band-gap behavior of periodic auxetic lattices”. In: *physica status solidi (b)* 242.3 (2005), pp. 665–680.

[26] F Casadei and JJ Rimoli. “Anisotropy-induced broadband stress wave steering in periodic lattices”. In: *International Journal of Solids and Structures* 50.9 (2013), pp. 1402–1414.

[27] Davide Bigoni et al. “Elastic metamaterials with inertial locally resonant structures: Application to lensing and localization”. In: *Physical Review B* 87.17 (2013), p. 174303.

[28] Pai Wang, Jongmin Shim, and Katia Bertoldi. “Effects of geometric and material nonlinearities on tunable band gaps and low-frequency directionality of phononic crystals”. In: *Physical Review B* 88.1 (2013), p. 014304.

[29] Fernando Fraternali et al. “Multiscale tunability of solitary wave dynamics in tensegrity metamaterials”. In: *Applied Physics Letters* 105.20 (2014), p. 201903.

[30] Julian J Rimoli and Raj Kumar Pal. “Mechanical response of 3-dimensional tensegrity lattices”. In: *Composites Part B: Engineering* 115 (2017), pp. 30–42.

[31] D De Tommasi et al. “Morphological optimization of tensegrity-type metamaterials”. In: *Composites Part B: Engineering* 115 (2017), pp. 182–187.

[32] Richard Buckminster Fuller. *Tensile-integrity structures*. US Patent 3,063,521. 1962.

[33] Anthony Pugh. *An introduction to tensegrity*. Univ of California Press, 1976.

[34] Robert E Skelton and Mauricio C de Oliveira. *Tensegrity systems*. Vol. 1. Springer, 2009.

[35] AG Tibert and S Pellegrino. “Deployable tensegrity reflectors for small satellites”. In: *Journal of Spacecraft and Rockets* 39.5 (2002), pp. 701–709.

[36] Wojciech Gilewski, Joanna Kłosowska, and Paulina Obara. “Applications of tensegrity structures in civil engineering”. In: *Procedia Engineering* 111 (2015), pp. 242–248.

[37] Mohammad RK Mofrad and Roger D Kamm. *Cytoskeletal mechanics: models and measurements in cell mechanics*. Cambridge University Press, 2006.

[38] Ning Wang et al. “Mechanical behavior in living cells consistent with the tensegrity model”. In: *Proceedings of the National Academy of Sciences* 98.14 (2001), pp. 7765–7770.

[39] Tim Liedl et al. “Self-assembly of three-dimensional prestressed tensegrity structures from DNA”. In: *Nature nanotechnology* 5.7 (2010), pp. 520–524.

[40] Julian J Rimoli. “On the impact tolerance of tensegrity-based planetary landers”. In: *57th AIAA/ASCE/AHS/ASC Structures, Structural Dynamics, and Materials Conference*. 2016, p. 1511.

[41] E Schmid and W Boas. “Kristallplastizitat’, 1935”. In: *Berlin. J. Springer* (1950).

[42] K Ito and V Vitek. “Atomistic study of non-Schmid effects in the plastic yielding of bcc metals”. In: *Philosophical Magazine A* 81.5 (2001), pp. 1387–1407.

[43] JW Christian. “Some surprising features of the plastic deformation of body-centered cubic metals and alloys”. In: *Metallurgical Transactions A* 14.7 (1983), pp. 1237–1256.

[44] Lucile Dezerald et al. “Plastic anisotropy and dislocation trajectory in BCC metals”. In: *Nature communications* 7 (2016).

[45] S Alkan and H Sehitoglu. “Non-Schmid response of Fe 3 Al: The twin-antitwin slip asymmetry and non-glide shear stress effects”. In: *Acta Materialia* 125 (2017), pp. 550–566.

[46] David Cereceda et al. “Unraveling the temperature dependence of the yield strength in single-crystal tungsten using atomistically-informed crystal plasticity calculations”. In: *International Journal of Plasticity* 78 (2016), pp. 242–265.

[47] Anirban Patra, Ting Zhu, and David L McDowell. “Constitutive equations for modeling non-Schmid effects in single crystal bcc-Fe at low and ambient temperatures”. In: *International Journal of Plasticity* 59 (2014), pp. 1–14.

[48] Göran Grimvall et al. “Lattice instabilities in metallic elements”. In: *Reviews of Modern Physics* 84.2 (2012), p. 945.

[49] Xiaohui Liu et al. “Crystal metamorphosis at stress extremes: how soft phonons turn into lattice defects”. In: *NPG Asia Materials* 8.10 (2016), e320.

[50] Robert Connelly and Walter Whiteley. “Second-order rigidity and prestress stability for tensegrity frameworks”. In: *SIAM Journal on Discrete Mathematics* 9.3 (1996), pp. 453–491.

[51] Simon D Guest. “The stiffness of tensegrity structures”. In: *IMA Journal of Applied Mathematics* 76.1 (2010), pp. 57–66.

[52] Andrej B?? na, Ioan Bucataru, and Michael A Slawinski. “Coordinate-free characterization of the symmetry classes of elasticity tensors”. In: *Journal of Elasticity* 87.2 (2007), pp. 109–132.

[53] SC Cowin and MM Mehrabadi. “Anisotropic symmetries of linear elasticity”. In: *Appl. Mech. Rev* 48.5 (1995), pp. 247–285.

[54] SC Cowin and MM Mehrabadi. “The structure of the linear anisotropic elastic symmetries”. In: *Journal of the Mechanics and Physics of Solids* 40.7 (1992), pp. 1459–1471.

[55] Morteza M Mehrabadi and Stephen C Cowin. “Eigentensors of linear anisotropic elastic materials”. In: *The Quarterly Journal of Mechanics and Applied Mathematics* 43.1 (1990), pp. 15–41.

[56] Christian Miehe, Jörg Schröder, and Martin Becker. “Computational homogenization analysis in finite elasticity: material and structural instabilities on the micro- and macro-scales of periodic composites and their interaction”. In: *Computer Methods in Applied Mechanics and Engineering* 191.44 (2002), pp. 4971–5005.

[57] Andrea Vigliotti and Damiano Pasini. “Linear multiscale analysis and finite element validation of stretching and bending dominated lattice materials”. In: *Mechanics of Materials* 46 (2012), pp. 57–68.

[58] Takashi Asada, Yuji Tanaka, and Nobutada Ohno. “Two-scale and full-scale analyses of elastoplastic honeycomb blocks subjected to flat-punch indentation”. In: *International Journal of Solids and Structures* 46.7 (2009), pp. 1755–1763.

[59] Marc Louis Maurice François, L Chen, and Michel Coret. “Elasticity and symmetry of triangular lattice materials”. In: *International Journal of Solids and Structures* (2017).

[60] Pushan Ayyub et al. “Effect of crystal size reduction on lattice symmetry and cooperative properties”. In: *Physical Review B* 51.9 (1995), p. 6135.

[61] VR Palkar et al. “Size-induced structural transitions in the Cu-O and Ce-O systems”. In: *Physical Review B* 53.5 (1996), p. 2167.

[62] Hossein Salahshoor, Raj Kumar Pal, and Julian J Rimoli. “Non-Schmid effects and finite wavelength instabilities in single crystal metals”. In: *Extreme Mechanics Letters* 20 (2018), pp. 9–13.

[63] N Ohno, D Okumura, and H Noguchi. “Microscopic symmetric bifurcation condition of cellular solids based on a homogenization theory of finite deformation”. In: *Journal of the Mechanics and Physics of Solids* 50.5 (2002), pp. 1125–1153.

[64] Giuseppe Geymonat, Stefan Müller, and Nicolas Triantafyllidis. “Homogenization of nonlinearly elastic materials, microscopic bifurcation and macroscopic loss of rank-one convexity”. In: *Archive for rational mechanics and analysis* 122.3 (1993), pp. 231–290.

[65] N Triantafyllidis and MW Schraad. “Onset of failure in aluminum honeycombs under general in-plane loading”. In: *Journal of the Mechanics and Physics of Solids* 46.6 (1998), pp. 1089–1124.

[66] N Triantafyllidis and S Bardenhagen. “The influence of scale size on the stability of periodic solids and the role of associated higher order gradient continuum models”. In: *Journal of the Mechanics and Physics of Solids* 44.11 (1996), pp. 1891–1928.

[67] EB Tadmor et al. “Mixed finite element and atomistic formulation for complex crystals”. In: *Physical Review B* 59.1 (1999), p. 235.

[68] Gero Friesecke and Florian Theil. “Validity and Failure of the Cauchy-Born Hypothesis in a Two-Dimensional Mass-Spring Lattice.” In: *Journal of nonlinear Science* 12.5 (2002).

[69] Giuseppe Buttazzo, Mariano Giaquinta, and Stefan Hildebrandt. *One-dimensional variational problems: an introduction*. Vol. 15. Oxford University Press, 1998.

[70] Clifford Truesdell and Walter Noll. “The non-linear field theories of mechanics”. In: *The non-linear field theories of mechanics*. Springer, 2004, pp. 1–579.

[71] John M Ball. “Convexity conditions and existence theorems in nonlinear elasticity”. In: *Archive for rational mechanics and Analysis* 63.4 (1976), pp. 337–403.

[72] John P Hirth and Jens Lothe. *Theory of dislocations*. John Wiley\& Sons, 1982.

[73] MA Tschopp, DE Spearot, and DL McDowell. “Atomistic simulations of homogeneous dislocation nucleation in single crystal copper”. In: *Modelling and Simulation in Materials Science and Engineering* 15.7 (2007), p. 693.

[74] Qing Qin and John L Bassani. “Non-Schmid yield behavior in single crystals”. In: *Journal of the Mechanics and Physics of Solids* 40.4 (1992), pp. 813–833.

[75] PW Bridgman. “The tensile properties of several special steels and certain other materials under pressure”. In: *Journal of Applied Physics* 17.3 (1946), pp. 201–212.

[76] Tiedo Tinga, WAM Brekelmans, and Marc GD Geers. “Cube slip and non-Schmid effects in single crystal Ni-base superalloys”. In: *modelling and simulation in materials science and engineering* 18.1 (2009), p. 015005.

[77] Lucas M Hale et al. “Insights on activation enthalpy for non-Schmid slip in body-centered cubic metals”. In: *Scripta Materialia* 99 (2015), pp. 89–92.

[78] V Paidar, DP Pope, and V Vitek. “A theory of the anomalous yield behavior in L12 ordered alloys”. In: *Acta Metallurgica* 32.3 (1984), pp. 435–448.

[79] S Alkan, Y Wu, and H Sehitoglu. “Giant non-Schmid effect in NiTi”. In: *Extreme Mechanics Letters* 15 (2017), pp. 38–43.

[80] Stefan C Soare. “Plasticity and non-Schmid effects”. In: *Proc. R. Soc. A*. Vol. 470. 2161. The Royal Society. 2014, p. 20130440.

[81] CD Barrett, Haitham El Kadiri, and MA Tschopp. “Breakdown of the Schmid law in homogeneous and heterogeneous nucleation events of slip and twinning in magnesium”. In: *Journal of the Mechanics and Physics of Solids* 60.12 (2012), pp. 2084–2099.

[82] Yu Mishin et al. “Structural stability and lattice defects in copper: Ab initio, tight-binding, and embedded-atom calculations”. In: *Physical Review B* 63.22 (2001). `http://www.ctcms.nist.gov/potentials`, p. 224106.

[83] H Chamati et al. “Embedded-atom potential for Fe and its application to self-diffusion on Fe (100)”. In: *Surface Science* 600.9 (2006). `http://www.ctcms.nist.gov/potentials`, pp. 1793–1803.

[84] PL Williams, Y Mishin, and JC Hamilton. “An embedded-atom potential for the Cu–Ag system”. In: *Modelling and Simulation in Materials Science and Engineering* 14.5 (2006). `http://www.ctcms.nist.gov/potentials`, p. 817.

[85] Y Mishin et al. “Interatomic potentials for monoatomic metals from experimental data and ab initio calculations”. In: *Physical Review B* 59.5 (1999). `http://www.ctcms.nist.gov/potentials`, p. 3393.

[86] Andrew T Jennings et al. “Modeling dislocation nucleation strengths in pristine metallic nanowires under experimental conditions”. In: *Acta Materialia* 61.6 (2013), pp. 2244–2259.

[87] Wahyu Setyawan and Stefano Curtarolo. “High-throughput electronic band structure calculations: Challenges and tools”. In: *Computational materials science* 49.2 (2010), pp. 299–312.

[88] Ryan S Elliott, Nicolas Triantafyllidis, and John A Shaw. “Stability of crystalline solidsI: Continuum and atomic lattice considerations”. In: *Journal of the Mechanics and Physics of Solids* 54.1 (2006), pp. 161–192.

[89] Nicolas Mounet and Nicola Marzari. “First-principles determination of the structural, vibrational and thermodynamic properties of diamond, graphite, and derivatives”. In: *Physical Review B* 71.20 (2005), p. 205214.

[90] MA Tschopp and DL McDowell. “Tension-compression asymmetry in homogeneous dislocation nucleation in single crystal copper”. In: *Applied physics letters* 90.12 (2007), p. 121916.

[91] Duane C Wallace and Janice L Patrick. “Stability of crystal lattices”. In: *Physical Review* 137.1A (1965), A152.

[92] Jean-Claude Michel et al. “Microscopic and macroscopic instabilities in finitely strained porous elastomers”. In: *Journal of the Mechanics and Physics of Solids* 55.5 (2007), pp. 900–938.

[93] Morton E Gurtin. *An introduction to continuum mechanics*. Vol. 158. Academic press, 1982.

[94] Shigenobu Ogata, Ju Li, and Sidney Yip. “Ideal pure shear strength of aluminum and copper”. In: *Science* 298.5594 (2002), pp. 807–811.

[95] D Roundy et al. “Ideal shear strengths of fcc aluminum and copper”. In: *Physical Review Letters* 82.13 (1999), p. 2713.

[96] Shigenobu Ogata et al. “Ideal shear strain of metals and ceramics”. In: *Physical Review B* 70.10 (2004), p. 104104.

[97] Laurent M Dupuy et al. “Finite-temperature quasicontinuum: molecular dynamics without all the atoms”. In: *Physical Review Letters* 95.6 (2005), p. 060202.

[98] Matt Fago et al. “Density-functional-theory-based local quasicontinuum method: Prediction of dislocation nucleation”. In: *Physical Review B* 70.10 (2004), p. 100102.

[99] Harry Geoffrey Hopkins and Michael J Sewell. *Mechanics of solids: The Rodney Hill 60th anniversary volume*. Elsevier, 2016.

[100] Hossein Salahshoor, Raj Kumar Pal, and Julian J Rimoli. “Material symmetry phase transitions in three-dimensional tensegrity metamaterials”. In: *Journal of the Mechanics and Physics of Solids* 119 (2018), pp. 382–399.

[101] K Koohestani and SD Guest. “A new approach to the analytical and numerical form-finding of tensegrity structures”. In: *International Journal of Solids and Structures* 50.19 (2013), pp. 2995–3007.

[102] K Koohestani. “Form-finding of tensegrity structures via genetic algorithm”. In: *International Journal of Solids and Structures* 49.5 (2012), pp. 739–747.

[103] Cornel Sultan and Robert Skelton. “Deployment of tensegrity structures”. In: *International Journal of Solids and Structures* 40.18 (2003), pp. 4637–4657.

[104] Milenko Masic, Robert E Skelton, and Philip E Gill. “Optimization of tensegrity structures”. In: *International Journal of Solids and Structures* 43.16 (2006), pp. 4687–4703.

[105] Rene Motro. *Tensegrity: structural systems for the future*. Elsevier, 2003.

[106] Nasseradeen Ashwear, Ganesh Tamadapu, and Anders Eriksson. “Optimization of modular tensegrity structures for high stiffness and frequency separation requirements”. In: *International Journal of Solids and Structures* 80 (2016), pp. 297–309.

[107] Haresh Lalvani. “Origins of tensegrity: views of Emmerich, Fuller and Snelson”. In: *International Journal of Space Structures* 11.1-2 (1996), pp. 27–27.

[108] F Fraternali, L Senatore, and C Daraio. “Solitary waves on tensegrity lattices”. In: *Journal of the Mechanics and Physics of Solids* 60.6 (2012), pp. 1137–1144.

[109] Ada Amendola et al. “Tuning frequency band gaps of tensegrity metamaterials with local and global prestress”. In: *arXiv preprint arXiv:1803.03472* (2018).

[110] Fernando Fraternali, Gerardo Carpentieri, and Ada Amendola. “On the mechanical modeling of the extreme softening/stiffening response of axially loaded tensegrity prisms”. In: *Journal of the Mechanics and Physics of Solids* 74 (2015), pp. 136–157.

[111] SD Guest and JW Hutchinson. “On the determinacy of repetitive structures”. In: *Journal of the Mechanics and Physics of Solids* 51.3 (2003), pp. 383–391.

[112] Aleksandar Donev and Salvatore Torquato. “Energy-efficient actuation in infinite lattice structures”. In: *Journal of the Mechanics and Physics of Solids* 51.8 (2003), pp. 1459–1475.

[113] VS Deshpande, MF Ashby, and NA Fleck. “Foam topology: bending versus stretching dominated architectures”. In: *Acta materialia* 49.6 (2001), pp. 1035–1040.

[114] AG Tibert and Sergio Pellegrino. “Review of form-finding methods for tensegrity structures”. In: *International Journal of Space Structures* 26.3 (2011), pp. 241–255.

[115] Julian J Rimoli. “A reduced-order model for the dynamic and post-buckling behavior of tensegrity structures”. In: *Mechanics of Materials* 116 (2018), pp. 146–157.

[116] Sandra Forte and Maurizio Vianello. “Symmetry classes for elasticity tensors”. In: *Journal of Elasticity* 43.2 (1996), pp. 81–108.

[117] Peter Chadwick, Maurizio Vianello, and Stephen C Cowin. “A new proof that the number of linear elastic symmetries is eight”. In: *Journal of the Mechanics and Physics of Solids* 49.11 (2001), pp. 2471–2492.

[118] J Rychlewski. “On Hooke’s law”. In: *Journal of Applied Mathematics and Mechanics* 48.3 (1984), pp. 303–314.

[119] Ellad B Tadmor, Ronald E Miller, and Ryan S Elliott. *Continuum mechanics and thermodynamics: from fundamental concepts to governing equations*. Cambridge University Press, 2012.

[120] Mildred S Dresselhaus, Gene Dresselhaus, and Ado Jorio. *Group theory: application to the physics of condensed matter*. Springer Science & Business Media, 2007.

[121] Christopher Bradley and Arthur Cracknell. *The mathematical theory of symmetry in solids: representation theory for point groups and space groups*. Oxford University Press, 2010.

[122] MH Yoo. “Slip, twinning, and fracture in hexagonal close-packed metals”. In: *Metallurgical Transactions A* 12.3 (1981), pp. 409–418.

[123] Nebojsa Murisic et al. “From discrete to continuum models of three-dimensional deformations in epithelial sheets”. In: *Biophysical journal* 109.1 (2015), pp. 154–163.

[124] John G Ramsay. “Development of chevron folds”. In: *Geological Society of America Bulletin* 85.11 (1974), pp. 1741–1754.

[125] Kaushik Bhattacharya. *Microstructure of martensite: why it forms and how it gives rise to the shape-memory effect*. Vol. 2. Oxford University Press, 2003.

[126] Katia Bertoldi and MC Boyce. “Mechanically triggered transformations of phononic band gaps in periodic elastomeric structures”. In: *Physical Review B* 77.5 (2008), p. 052105.

[127] Raj Kumar Pal, Julian Rimoli, and Massimo Ruzzene. “Effect of large deformation pre-loads on the wave properties of hexagonal lattices”. In: *Smart Materials and Structures* 25.5 (2016), p. 054010.

[128] Raj Kumar Pal et al. “A study of deformation localization in nonlinear elastic square lattices under compression”. In: *Phil. Trans. R. Soc. A* 376.2127 (2018), p. 20170140.

[129] Christelle Combescure, Pierre Henry, and Ryan S Elliott. “Post-bifurcation and stability of a finitely strained hexagonal honeycomb subjected to equi-biaxial in-plane loading”. In: *International Journal of Solids and Structures* 88 (2016), pp. 296–318.

[130] John Walter Rudnicki and JR Rice. “Conditions for the localization of deformation in pressure-sensitive dilatant materials”. In: *Journal of the Mechanics and Physics of Solids* 23.6 (1975), pp. 371–394.

[131] Lorna J Gibson and Michael F Ashby. *Cellular solids: structure and properties*. Cambridge university press, 1999.

[132] Scott D Papka and Stelios Kyriakides. “In-plane compressive response and crushing of honeycomb”. In: *Journal of the Mechanics and Physics of Solids* 42.10 (1994), pp. 1499–1532.

[133] S Da Papka and Sa Kyriakides. “Experiments and full-scale numerical simulations of in-plane crushing of a honeycomb”. In: *Acta materialia* 46.8 (1998), pp. 2765–2776.

[134] SD Papka and S Kyriakides. “Biaxial crushing of honeycombs:Part 1: Experiments”. In: *International Journal of Solids and Structures* 36.29 (1999), pp. 4367–4396.

[135] MP Santisi d’Avila, Nicolas Triantafyllidis, and Guangyang Wen. “Localization of deformation and loss of macroscopic ellipticity in microstructured solids”. In: *Journal of the Mechanics and Physics of Solids* 97 (2016), pp. 275–298.

[136] David K Campbell, Sergej Flach, Yuri S Kivshar, et al. “Localizing energy through nonlinearity and discreteness”. In: *Physics Today* 57.1 (2004), pp. 43–49.

[137] AJ Sievers and S Takeno. “Intrinsic localized modes in anharmonic crystals”. In: *Physical Review Letters* 61.8 (1988), p. 970.

[138] Carlos M Portela, Julia R Greer, and Dennis M Kochmann. “Impact of node geometry on the effective stiffness of non-slender three-dimensional truss lattice architectures”. In: *Extreme Mechanics Letters* 22 (2018), pp. 138–148.

[139] Lucas R Meza et al. “Reexamining the mechanical property space of three-dimensional lattice architectures”. In: *Acta Materialia* 140 (2017), pp. 424–432.

[140] JY Zhang and M Ohsaki. “Stability conditions for tensegrity structures”. In: *International journal of solids and structures* 44.11-12 (2007), pp. 3875–3886.

[141] Robert Connelly and Allen Back. “Mathematics and Tensegrity: Group and representation theory make it possible to form a complete catalogue of” strut-cable” constructions with prescribed symmetries”. In: *American Scientist* 86.2 (1998), pp. 142–151.

[142] Charles B Morrey et al. “Quasi-convexity and the lower semicontinuity of multiple integrals.” In: *Pacific journal of mathematics* 2.1 (1952), pp. 25–53.